

氮化鎵薄膜的結構缺陷及表面態特性研究

**The investigation of structural defects and surface states on GaN films**

研究生：鍾浩銘

Student : Hao-Ming Chung

指導教授：陳衛國 博士

Advisor : Dr. Wei-Kuo Chen

國立交通大學  
電子物理研究所

博士論文

A Dissertation

Submitted to Institute of Electrophysics

College of Science

National Chiao Tung University

in Partial Fulfillment of the Requirements

for the Degree of

Doctor of Philosophy

in

Electrophysics

June 2004

Hsinchu, Taiwan, Republic of China

中華民國九十三年六月

# 氮化鎵薄膜的結構缺陷及表面態特性研究

研究生：鍾浩銘

指導教授：陳衛國博士

國立交通大學 電子物理研究所

## 摘要

本論文運用包括霍爾、電壓電流特性、光電容、電容電壓特性、深層能階暫態能譜及 X 光吸收光譜等電學及光學量測方法，探討由有機金屬汽相磊晶成長氮化鎵薄膜及其蕭基二極體元件，(1)在有銻、砷或鎂元素摻入以及熱退火之下的結構缺陷；(2)其中光電容衰減效應的發現及研究；以及(3)其表面態與在不同表面處理之下的表面鈍化效應。

新發現如下：(1)我們發現一個在導帶下方 0.769 電子伏特，與砷相關的新能階，極可能是砷佔據氮的位置所產生。我們發現一個呈現對數光電容衰減的暫態行為，是與錯位缺陷密切相關，我們並且發展出新的方法取得此行為之對數時間常數以及捕捉截面積。(2)我們發現熱退火對鎂摻雜薄膜產生的影響是非等向性的，並且對垂直薄膜表面方向的晶體微結構影響顯著，我們也發現晶相混合比例以及德拜溫度隨退火時間的增加而變化。(3)我們也成功發展出 p 型半導體的表面態計算方法，並將之運用在分析不同表面處理下的 p 型氮化鎵蕭基二極體。

整體而論，在等價位銻元素摻雜方面，我們發現摻雜等價位銻元素可以抑制深層能階的生成，並改善了 n 型氮化鎵蕭基二極體的電學特性，顯示等價位銻元素摻雜是改善氮化鎵薄膜品質的可行方法。光電容量測亦可證實這個結果。關於熱退火效應，我們發現砷離子佈植氮化鎵薄膜的電學特性，可以經由熱退火恢復到未佈植樣品的狀態；我們還發現所有鎂摻雜氮化鎵薄膜的都顯示，在熱退火過程中，其混合晶相會變得包含更多更穩定的六方晶相結構，並且原子的排列更有秩序。最後在 p 型氮化鎵蕭基二極體的表面處理方面，透過硫化處理，我們成功的將 p 型氮化鎵蕭基二極體的理想因子降到 1.14，據我們所知，此結果已稱得上世界級的水準。

# The investigation of structural defects and surface states on GaN films

Student: Hao-Ming Chung

Advisor: Dr. Wei-Kuo Chen

Institute of Electrophysics, National Chiao-Tung University

Hsin-Chu, Taiwan, R.O.C.

## Abstract

Electrical and optical measurements, including Hall, current-voltage, phot capacitance, capacitance-voltage, deep level transient spectroscopy and *x*-ray absorption measurements, *etc.*, has been employed to investigate the following effects, respectively. First, the various effects of structural defects and surface states on GaN films through the incorporation of In, As and Mg atoms into GaN with or without post-annealing have been intensively studied. Secondly, the novel observation and the detailed discussion of the long-term phot capacitance decay behavior will be reported. And at last, the influence of various surface treatments on surface states and the passivation of GaN surface will be taken up.

Some salient features in our findings are listed as follows. (1) A trap-center related to arsenic is found located at 0.769 eV below the conduction band, which behaves most likely antisite in nature. (2) A decay phenomenon with logarithmic feature is found in the phot capacitance measurements and is relevant to the effect of traps associated with dislocations. By the way a technique is developed to retrieve the logarithmic time constants and capture cross sections as well. Moreover, (3) the effects of thermal annealing on Mg-doped GaN films are found to be anisotropic with respect to the crystal axes and have the greatest crystal microstructural change along the perpendicular of the epilayer surface. The effects also involved shifting of the structural mixing ratio between polytypes and increasing of Debye temperature of the films. In addition, we develop a method to characterize the surface states on *p*-GaN surface, and we use this method to analyze the *p*-GaN Schottky diodes with various surface treatments.

As a whole, some important remarks on the practical viewpoints for operation and design of the possible modern electronic devices are worthy noted. On the isoelectronic In doping, we found In isodoping can effectively suppress the formation of deep levels and improve the electrical properties of *n*-GaN Schottky diodes, indicating that the isoelectronic In doping technique is a viable way to improve the *n*-GaN film quality. This has been confirmed by the results of phot capacitance measurements. As for the thermal annealing effects, we found the electrical properties of As-implanted GaN films can be recovered to that of the un-implanted ones, and all the findings on the Mg-doped GaN films indicated crystal structure relaxation towards a more stable hexagonal wurtzite configuration and atomic rearrangement to a more orderly condition after annealing. Finally on the surface treatment effects of *p*-GaN Schottky diodes, we realized the *p*-GaN Schottky diode with the ideality factor down to the value of 1.14 through the sulfide pretreatment, maybe nearly ideal optimization on the operation of *p*-GaN Schottky diodes currently.

## 致 謝 (Acknowledgements)

在攻讀博士學位的過程中，首先要由衷的感謝指導教授陳衛國老師，不論是在研究工作、論文寫作以及待人處事上，給予我長期的耐心指導並提供我良好的研究設備與環境，啟發我做研究的方法與觀念，讓我能順利完成博士學位。

其次，感謝陳文雄教授以及李明知教授在研究過程中對我的鼓勵與指導。感謝口試委員會召集人郭義雄教授的幫助與指導，使我的物理知識能在準備口試期間有更進一步啟發與架構上的統整。感謝晶采微元科技總經理姜崇義博士，在百忙之中參加我的口試，並感謝他在中科院期間，對於量測儀器以及樣品所提供的支援。感謝周武清教授以及晶元光電專案經理，學長歐震博士在口試上的指教。感謝黃迪靖老師使我在跨入新的研究領域的方法上有所嘗試與啟發，並感謝黃老師在口試上的指導。感謝施敏教授在百忙之中回覆我關於表面態的問題。感謝在我擔任交通大學游泳校隊隊員期間，張秀梅老師在游泳方面的指導，使我得以有強健的身心承受博士的訓練。

此外，感謝學長陳乃權博士在電學量測理論、實驗儀器架設、分析技巧及研究方法上的啟蒙，感謝學長王錦雄博士在電學研究上的共同討論，感謝學長潘永中博士的樣品支援以及實驗與處事上的指教，感謝同學許永昌博士在電腦數值分析方法上的啟發，感謝同學林銘杰博士的合作與關心，感謝同學鍾旺成在電學量測系統的建構與電學元件的製作的密切合作，

感謝實驗室伙伴李文雄、黃懷瑩、張富欽、柯文政、沈坤慶以及李寧在研究過程中的共同研討，感謝蕭家慶、黃俊元、盧建志、陳俊亮、劉建忠、林國隆等學弟妹在實驗上的幫忙，尤其是洪肇逸、曹衛立、李文祺、蔡政忠以及李寧，謝謝你們的配合與辛勞付出不但使本論文更加豐富，也是使我領導能力與智識不斷提升的重要驅動力。

最後，要感謝我的家人，感謝母親、妹妹、弟弟及女友這幾年來的辛苦、支持與關心，願以畢業的喜悅以及此論文獻與我最愛的你們。

# CONTENTS

LIST OF FIGURES	xvi
LIST OF TABLES	xvii
1 INTRODUCTION	1
2 THEORETICAL BACKGROUNDS	5
2.1 Generation-Recombination Statistics of Deep Levels . . . . .	5
2.2 X-ray Absorption Fine Structures . . . . .	7
2.2.1 Near X-ray Absorption Fine Structure . . . . .	9
2.2.2 Extend X-ray absorption Fine Structure . . . . .	11
2.3 Theory of Surface States in Metal-Semiconductor Systems . . . . .	18
3 EXPERIMENTAL DETAILS	27
3.1 Hall Measurement Systems . . . . .	27
3.2 Electrical Characterization Systems . . . . .	28
3.3 XAFS Systems . . . . .	28
4 ISOELECTRONIC IN-DOPING EFFECTS IN GAN	37
4.1 Introduction . . . . .	37
4.2 Experiments . . . . .	38
4.3 Results and Discussion . . . . .	39

4.4	Summary . . . . .	46
5	ISOELECTRONIC AS-IMPLANTED EFFECTS IN GAN	48
5.1	Introduction . . . . .	48
5.2	Experiments . . . . .	49
5.3	Results and Discussion . . . . .	49
5.4	Summary . . . . .	58
6	MICROSTRUCTURAL STUDY OF THERMAL ANNEALING EFFECTS ON MG DOPED GAN FILMS	60
6.1	Introduction . . . . .	60
6.2	Experiments . . . . .	61
6.3	Results and Discussion . . . . .	63
6.4	Summary . . . . .	74
7	LONG-TERM PHOTOCAPACITANCE DECAY BEHAVIOR IN UNDOPED GAN FILMS	75
7.1	Introduction . . . . .	75
7.2	Experiments . . . . .	76
7.3	Design of Photocapacitance Measurements . . . . .	77
7.4	Results and Discussion . . . . .	77
7.5	Summary . . . . .	88
8	ISOELECTRONIC IN-DOPING EFFECTS ON THE LONG-TERM PHO-	



TOCAPACITANCE DECAY BEHAVIOR IN GAN	90
8.1 Introduction . . . . .	90
8.2 Experiments . . . . .	91
8.3 Results and Discussion . . . . .	92
8.4 Summary . . . . .	99
9 SURFACE TREATMENT EFFECTS ON <i>P</i> -GAN SCHOTTKY DIODES	100
9.1 Introduction . . . . .	100
9.2 Experiments . . . . .	101
9.3 Results and Discussion . . . . .	102
9.4 Summary . . . . .	109
10 CONCLUSION	111
10.1 On the Isoelectronic In-doping Effects in GaN . . . . .	111
10.2 On the Isoelectronic As-implanted Effects in GaN . . . . .	111
10.3 On the Microstructural Study of Thermal Annealing Effects on Mg doped GaN Films . . . . .	112
10.4 On the Long-Term Photocapacitance Decay Behavior in Undoped GaN Films . . . . .	112
10.5 On the Isoelectronic In-doping Effects on the Long-Term Photoca- pacitance Decay Behavior in GaN . . . . .	113
10.6 On the Surface Treatment Effects on GaN Schottky Diodes . . . . .	113

# LIST OF FIGURES

2.1	The schematic diagram of the generation-recombination mechanisms on deep levels. . . . .	8
2.2	Schematic representation of the fluorescence yield mode and the resulting $x$ -ray absorption spectrum $\mu_x$ vs $E$ . . . . .	13
2.3	The Model of interference effect of EXAFS. . . . .	15
2.4	Energy band diagram of a metal- $p$ -type semiconductor contact with an interfacial layer. . . . .	20
3.1	The schematic diagrams of the Hall measurement system. . . . .	29
3.2	The schematic layout of the electrical characterization systems. . . . .	30
3.3	The optical layout of the 6m-HSGM beamlines. S is the radiation source. HFM and VFM are spherical mirrors. S1, S2 are the entrance and exit slits. G is a spherical grating. RFM is an toroidal mirror. D is sample position. . . . .	31
3.4	The relationship between intensities of different gratings and the photon energy. The curve labeling 700 $l/mm$ is pertinent to our experiment. . . . .	33
3.5	Wiggler X-ray beamline layout. Where FE:Front-end, FT:Filter tank, CM:Collimating mirror, Mono: Monochromater, RFM:Refocusing mirror, HHRM:High-order harmonic rejection mirror. . . . .	34



3.6	Some major components of the Wiggler-C (BL17C) beam line. . .	35
3.7	The typical X-ray absorption spectrum detecting system of BL17C.	36
4.1	Room temperature current density-voltage characteristics of Ni-GaN Schottky diodes. . . . .	41
4.2	The DLTS spectra of undoped and In-doped GaN samples at rate window of $1.65 \text{ s}^{-1}$ . . . . .	43
4.3	Arrhenius plot of the inverse emission rate times temperature squared vs reciprocal temperature for undoped GaN film. . . . .	44
5.1	Distribution of implanted As atoms in GaN films with various dosage levels simulated by TRIM programs. . . . .	50
5.2	Carrier mobility and concentration of GaN films with various As-implanted dosage vs the annealing time. . . . .	52
5.3	DLTS spectra of the as-grown, As14-60, and As15-60 samples. . .	53
5.4	Arrhenius plot of DLTS signals for as-grown, As14-60, and As15-60 samples. Similar deep levels published in previous literatures are also included in this figure. . . . .	55
5.5	The schematic diagram on the energy level of As substitute on Ga site, and its related transitions measured by DLTS and PL measurements. . . . .	59
6.1	SIMS results of Mg doped GaN with various $\text{Cp}_2\text{Mg}$ flow rates. . .	62

6.2	Ga $K$ -edge XANES spectra of amorphous, heavily Mg-doped, and undoped GaN films in (a) $c$ axis ( $E \parallel c$ ) and (b) $ab$ plane ( $E \perp c$ axis) polarization mode. . . . .	64
6.3	Fourier transform (FT) amplitudes of Ga $K$ -edge EXAFS for heavily Mg-doped GaN annealing after 0, 30, and 60 min in (a) $c$ axis ( $E \parallel c$ ) and (b) $ab$ plane ( $E \perp c$ axis) polarization mode. . . . .	66
6.4	Comparisons of $k^3\chi(k)$ oscillations for the $E \parallel c$ axis polarization of (a) our $u$ -GaN and the FEFF8-generated undoped hexagonal GaN, (b) 1 hour annealed $x$ -GaN and the simulated case of $1\text{Mg}_i+1\text{Mg}_{Ga}$ , (c) 1 hour annealed $x$ -GaN and the simulated of mixed-phase $1\text{Mg}_i+1\text{Mg}_{Ga}$ , (d) the case of (c) using reduced $T_D = 500\text{K}$ , showing the best fit of our data. . . . .	70
6.5	Hexagonal phase fractions for as-grown, 30 min, and 60 min annealed GaN:Mg films. . . . .	71
6.6	Debye Temperatures for as-grown, 30 min, and 60 min annealed GaN:Mg films. . . . .	72
7.1	Schematic procedures of photocapacitance measurements. . . . .	78
7.2	The transient capacitance response of the undoped GaN during the applications of square voltage recorded at different waiting time, $t$ , at room temperature. . . . .	79

7.3	The steady state value of transient capacitance, $C_S(t)$ versus waiting time $t$ at room temperature for undoped GaN. . . . .	81
7.4	The status of excess carriers in GaN (a) during the photopumping (b) at the time soon after the photopumping, and (c) at prolonged time after the switch-off of the light. The open rectangles enclosing negative charged ions symbolizes the groups of linear arranged dislocation traps. . . . .	83
7.5	The ratio of $n_T(t)$ and $N_D$ versus waiting time $t$ at room temperature.	87
8.1	The transient capacitance response of the undoped and In-doped GaN during the applications of square voltage recorded at different waiting time, $t$ , at room temperature. . . . .	94
8.2	The steady state value of transient capacitance, $C_S(t)$ versus waiting time $t$ at room temperature for undoped and In-doped GaN. .	95
8.3	The ratio of $n_T(t)$ and $N_D$ versus waiting time $t$ at room temperature for undoped and In-doped GaN films in linear scale. . . . .	96
8.4	The ratio of $n_T(t)$ and $N_D$ versus waiting time $t$ at room temperature for undoped and In-doped GaN films in log scale. . . . .	97
9.1	Room temperature current density-voltage characteristics of Ni-GaN Schottky diodes with various surface treatments in both linear and log scales. . . . .	104

9.2 Room temperature capacitance-voltage characteristics of Ni-GaN  
Schottky diodes with various surface treatments. . . . . 106



# LIST OF TABLES

4.1	Results of forward bias I-V measurement for undoped and isoelectronic In-doping GaN films. . . . .	40
4.2	Results of deep level transient spectroscopy measurement for undoped and isoelectronic In-doping GaN films. . . . .	42
5.1	Parameters of Hall and current-voltage properties for as-grown, As14, As14-60, As15, and As15-60 samples. . . . .	54
5.2	The parameters of DLTS signals for as-grown, As14-60, and As15-60 samples. . . . .	56
6.1	EXAFS-analysis results of $x$ -GaN through 60 min thermal annealing (TA). . . . .	67



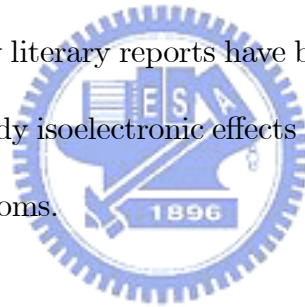
# CHAPTER 1

## INTRODUCTION

With the properties of wide-direct bandgaps, high thermal conductivity and superior thermal stability, gallium nitride (GaN) and related-nitride materials have recently drawn much attention from the view point of use in a variety of applications on electronic, optoelectronic and high-power devices, including high-temperature transistors, blue and green light-emitting diodes and violet laser diodes, *etc.* These devices lead us to the world with all-solid-state systems, full-color-flat panel systems, compact and high-density optical storage systems, high-speed printing system, and small medical apparatus, *etc.* These developments in one way require high-quality wide-bandgap semiconductor films with controllable electrical conductivity and luminescence properties. In the other way, in order to improve their performance, they also demand proper engineering on semiconductor films and surfaces to reduce structural defects and surface states.

It has been reported that deep-level defects are one of the principle factors impeding the performance of GaN-based transistors. Such defects can generally cause nonradiative recombinations in the active layer and result in an increase of threshold current in nitride semiconductor laser diode. In addition, as compared to GaAs and InP, GaN usually possesses relatively poor film quality in terms of

dislocations. With such a high density of threading edge dislocations ( $10^8 \text{ cm}^{-2}$ ), it was difficult to believe that high-performance optoelectronic devices can be realized without difficulty by the use of this type of material. Varieties of growth techniques have been employed to improve the crystalline and device quality, among them incorporation of isoelectronic atoms has been proved to be a viable method in reducing the unintentional impurity dislocation as well as deep level concentrations. For instance, in the GaP indirect material system, the quantum efficiency can be increased by two-order of magnitude because of the formation of isoelectronic nitrogen center. In the GaAs material system, isoelectronic indium doping has also shown an order of magnitude in reduction of dislocation density. However, up to date very few literary reports have been addressed on this issue on GaN, we thus attempt to study isoelectronic effects in GaN with the incorporation of isoelectronic In and As atoms.



In the emerging of GaN-related optoelectronic devices, additional improvements are needed to enhance the performance and reliability for commercial applications. A major issue is to increase *p*-type conductivity. To meet the criterion of device quality, thermal processing for the activation of *p*-type dopant (commonly prepared with magnesium) becomes a critical step. Though some work has been devoted to the effects of thermal annealing on electrical and optical properties, the study of effects on microscopic crystal properties are limited. In this thesis, we examined these properties on 30 min and 1 hour 700°C thermal

annealed samples using x-ray absorption fine structure (XAFS) measurements. Analysis of the obtained data showed thermal annealing resulted in more ordered atomic arrangement and richer concentration of the stable polytype in films.

One of the major trends in modern electronic materials and device research is to reduce individual device down to nanoscale dimensions. At such a small scale, the total number of surface and interface atoms then becomes a significant part of the device. The passivity and stability of surface atoms are expected to control to a large degree the performance and reliability of a particular device. Even now for air-oxidized III-V surfaces, the high number of surface states and high surface recombination velocity have contributed to many failures in optoelectronic devices such as catastrophic optical mirror damage in semiconductor lasers. Surface passivations has, for example, been found to be an absolutely essential process in the manufacturing of micro-disk lasers. Therefore, ways of removing native oxides and passivating the surface against oxidation have been actively researched in recent years both for device manufacturing and for epitaxial growth on patterned surfaces. Sulfur and chlorine passivation have been the most widely used passivation method in III-V materials. For example, it is found that S forms bridge bonds with group-III elements and therefore, naturally saturates all dangling bond states. It is also found that Cl atoms can terminate the GaAs surface with Ga-Cl bonds and eliminates surface states caused by surface oxides. However, up to date very few literary reports have been addressed on this issue on the Schottky contact of



*p*-type GaN. Thus in this dissertation, we will discuss the role of surface states on the *p*-GaN devices through examining the Ni Schottky contacts on Mg-doped GaN films with various surface treatments. Our results indicate that the electronic properties of  $(\text{NH}_4)_2\text{S}_x$ -treated *p*-GaN Schottky diodes can be effectively improved as compared to the untreated and HCl-treated samples because of the reduction of surface states in the metal-semiconductor interface.

The organization of this dissertation is as follows. This dissertation is divided into seven chapters. Chapter 1 is the introduction. Chapter 2 and 3 are the theoretical backgrounds and experimental details necessary to this thesis. Chapter 4 and 5 deal with the effects of isoelectronic atoms, In and As, on the *n*-type GaN films. Chapter 6 discuss the effects of thermal annealing effects on GaN films doped by Mg atoms, which are the most common *p*-type dopant for GaN films. In chapter 7 and 8, we discuss the long-term photocapacitance decay behavior in undoped and In-doped GaN films. They are related to the deep traps related to the dislocations. In chapter 9, we focus on the effects of surface treatment on *p*-GaN Schottky diodes, and the changes of surface states are also discussed. In the long run, summary and conclusions will be given in chapter 10.

## CHAPTER 2

### THEORETICAL BACKGROUNDS

In this chapter, we will introduce some of the most important theoretical backgrounds necessary to this thesis. First of all, we will discuss the generation and recombination statistics of deep levels. It describes the interactions of the deep levels and carriers in the conduction and valance bands, and it plays an important role in the development of characterization of deep levels in the semiconductors. In addition, we shows the theory of  $x$ -ray absorption fine structures, including the near  $x$ -ray absorption fine structure (NEXAFS) and the extend  $x$ -ray absorption fine structure (EXAFS), which can also identify the effects introduced by structural defects in the materials. Finally, we developed the theory of surface states in  $p$ -type metal-semiconductor systems, which enables us to observe the influences of surface states in the metal-semiconductor systems and provides us the way to improve the quality of  $p$ -type GaN Schottky diodes.

#### 2.1 Generation-Recombination Statistics of Deep Levels

A generation-recombination (G-R) center can exist in one of two states. When occupied by an electron, it is in the  $n_T$  state and when occupied by a hole, it is in the  $p_T$  state (both shown in Fig.2.1). The density of G-R centers occupied by

electrons  $n_T$  and holes  $p_T$  must equal to the total density  $N_T$  or

$$N_T = n_T + p_T. \quad (2.1)$$

The electron density in the conduction band is diminished by electron capture [process (a) in Fig.2.1] and increased by electron emission [process (b) in Fig.2.1].

The time rate of change of the electron density in the conduction band  $n$  due to the G-R mechanism is given by

$$\frac{dn}{dt} = (b) - (a) = e_n n_T - c_n n p_T. \quad (2.2)$$

The emission rate  $e_n$  represents the electrons emitted per second from the electron-occupied G-R centers. The capture rate  $c_n n$  represents the density of electrons captured per second from the conduction band. The capture coefficient  $c_n$  is defined by

$$c_n = \sigma_n v_{th}, \quad (2.3)$$

where  $v_{th}$  is the electron thermal velocity and  $\sigma_n$  is the electron capture cross section of the G-R center. A center with a negative or repulsive charge has a smaller capture cross section than one that is neutral or attractively charged.

Neutral capture cross sections are on the order of the physical size of the atom.

For holes, the parallel expression is

$$\frac{dp}{dt} = (d) - (c) = e_p p_T - c_p p n_T. \quad (2.4)$$

Whenever an electron or hole is captured or emitted, the center occupancy changes, and that rate of changes is, from Eqs. ( 2.2) and (2.3) given by

$$\begin{aligned}\frac{dn_T}{dt} &= \frac{dp}{dt} - \frac{dn}{dt} \\ &= (c_n n + e_p)(N_T - n_T) - (c_p p + e_n)n_T.\end{aligned}\quad (2.5)$$

In a reverse-biased space-charge region both  $n$  and  $p$  are small and can, to first order, be neglected. In the quasi-neutral regions  $n$  and  $p$  are reasonably constant. Solving Eq. (2.5) for condition (2) gives  $n_T(t)$  as

$$n_T(t) = n_T(0) \exp\left(\frac{-t}{\tau}\right) \quad (2.6)$$

$$+ \frac{(e_p + c_n n)N_T}{e_n + c_n n + e_p + c_p p} \left[1 - \exp\left(\frac{-t}{\tau}\right)\right],$$

where  $n_T(0)$  is the density of G-R centers occupied by electrons at  $t = 0$ , and

$$\tau = \frac{1}{e_n + c_n n + e_p + c_p p}. \quad (2.7)$$

The steady-state density as  $t \rightarrow \infty$  is

$$n_T = \frac{(e_p + c_n n)N_T}{e_n + c_n n + e_p + c_p p}. \quad (2.8)$$

Equations (2.6) to (2.8) are the basis for most deep-level impurity measurements.

## 2.2 X-ray Absorption Fine Structures

X-rays are electromagnetic radiations which lie between ultraviolet light and gamma rays in the electromagnetic spectrum.  $x$ -rays are characterized by the

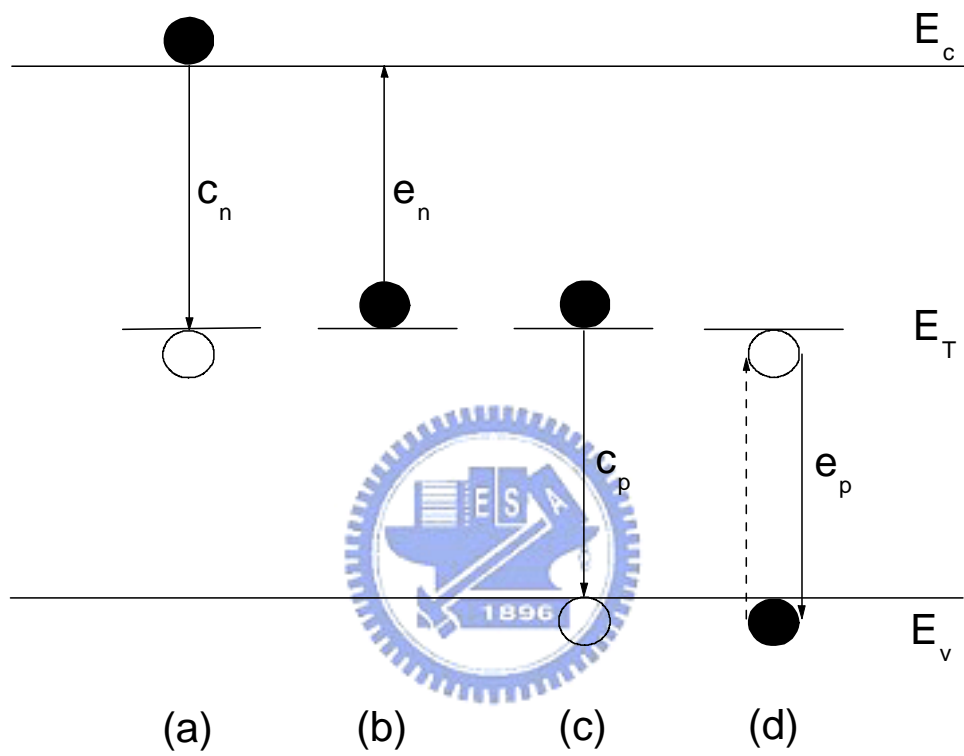


Figure 2.1: The schematic diagram of the generation-recombination mechanisms on deep levels.

relatively short wavelengths of 0.01 Å to 100 Å with hard  $x$ -rays on one end and soft  $x$ -rays on the other. Throughout the history of modern physical science,  $x$ -rays have been used as powerful tools in analytical, physical, chemical, biological, and structure characterization of matter.

### 2.2.1 Near X-ray Absorption Fine Structure

In the NEXAFS spectra of semi-conductor solids there are contributions due to transitions from the initial state to a final bound state in the conduction band which give rise to resonances superimposed to a steplike absorption resulting from transitions to the continuum. The  $x$ -ray absorption is given from the equation [1]:

$$\sigma_x = \frac{4\pi^2 \hbar^2 e^2}{m^2} \frac{1}{\hbar c \hbar \omega} |\langle f | \mathbf{e} \cdot \mathbf{p} | i \rangle|^2 \rho_f(E), \quad (2.9)$$

where  $m$  is the electron mass,  $e$  the electron charge,  $c$  is the velocity of light,  $\hbar\omega$  is the incident photon energy,  $\mathbf{e}$  is a unit vector along the direction of the electron field vector  $E$ ,  $\mathbf{p}$  is the sum of the linear moment of the electron;  $|\langle f | \mathbf{e} \cdot \mathbf{p} | i \rangle|^2$  is the dipole matrix element and  $\rho_f$  is the density of state in the continuum. Eq. (2.9) shows the intensity of this absorption depends on the dipole matrix element and the density of states (DOS) in the continuum. In the case of transitions to bound states the  $x$ -ray absorption cross section is given from the equation [1]:

$$\sigma_x(E) = \frac{2\pi^2 \hbar}{mc} f \rho_b(E), \quad (2.10)$$

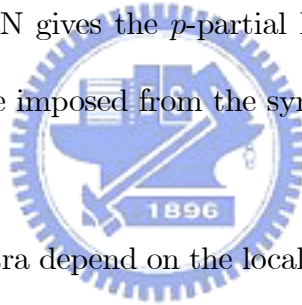
where  $\rho_b$  is the density of bound states and  $f$  is the oscillator strength, a dimensionless “number” which is proportional to the area under a NEXAFS resonance,

given by

$$f = \frac{2}{m\hbar\omega} |\langle f | \mathbf{e} \cdot \mathbf{p} | i \rangle|^2. \quad (2.11)$$

The density and the width of a transition are given by  $\sigma_x$  and  $1/\rho_b$ , respectively. The dipole matrix for crystalline solids generally depends on the angle of incidence of the linearly polarized synchrotron light and therefore the areas under the resonances (oscillator strengths) depend on the angle of incidence.

One important selection rule is the  $\Delta l = \pm 1$ , *i.e.*, the angular momentum of the electron in the initial and the final state should differ by  $\pm 1$ . In the case of 1s initial state (*K*-edge) the final state should have *p* component and for that reason a N *K*-edge spectrum of GaN gives the *p*-partial DOS in the conduction band. Additional selection rules are imposed from the symmetry of the solid, *i.e.*, from group theory considerations.



Since the NEXAFS spectra depend on the local symmetry around the central absorbing atom, angular dependence should be expected in certain symmetries. GaN exists in two polytypes: cubic ( $T_d$ ) and hexagonal ( $C_{6v}$ ). In the case of isotropic materials, such as the cubic GaN, the NEXAFS spectra dose not depend on the angle of incidence. The allowed transitions are  $1a_1 \rightarrow t_2^*$ , which are expected to have an intensity that is invariant with  $\theta$ [2].

On the other hand, when the material belongs to the  $C_{6v}$  symmetry group, the initial state is of  $1a_1$  symmetry and the allowed transitions are  $1a_1 \rightarrow a_1^*$  and  $1a_1 \rightarrow e_1^*$  [2]. The first will be observed strongest when the electron field vector is

parallel to  $z$  [in the case of hexagonal GaN grown on (0001)  $\text{Al}_2\text{O}_3$  parallel to the  $c$  axis], *i.e.*, for grazing incidence. The second will be observed strongest when the electron field vector is parallel to the  $(x,y)$  plane, *i.e.*, for normal incidence.

The  $e_1^*$  final state results from mixing of  $p_x$  and  $p_y$  orbitals and can be considered as a plane orbital and the  $a_1^*$  state results from mixing of  $s$  and  $p_z$  orbitals and can be considered as a vector orbital along the  $z$  axis. Consequently, when  $E \parallel c$ , *i.e.*, the electric field parallels to the hexagonal GaN  $c$ -axis, the  $p_z$  or out-of-plane orbitals are preferentially excited at  $K$ -edge. Similarly, when  $E \perp c$ , *i.e.* the electric field normal to the hexagonal GaN  $c$ -axis, the  $p_x$  and  $p_y$  or in-plane orbitals are preferentially excited. Such effects have been reported earlier by Lawniczak-Jablonska *et al.* for N  $K$ -edge absorption in the binary III-nitrides AlN, GaN, and InN [3]. It is apparent from the above discussion that the NEXAFS spectra are independent of the angle of incidence for the cubic GaN but depend on the incidence angle for the hexagonal GaN.

### 2.2.2 Extend X-ray absorption Fine Structure

Extended  $x$ -ray absorption fine structure (EXAFS) refers to the oscillatory variation of the  $x$ -ray absorption as a function of photon energy beyond  $\sim 40$  eV of an absorption edge. Although the extended fine structure has been known for a long time (Kronig, 1931, 1932) [4, 5], its structural content was not fully recognized until the work of Stern, Lytle, and Sayers [6, 7] (1974, 1975). In addition, the



availability of synchrotron radiation has resulted in the establishment of EXAFS as a practical structure tool particularly through the work of Eisenberger [8] (1975) and Kincaid [9, 10, 11]. This technique is especially valuable for structure analysis of chemical or biological systems where conventional diffraction methods are not applicable.

EXAFS spectroscopy refers to the measurement of the  $x$ -ray absorption coefficient  $\mu$  as a function of photon energy  $E$  above the threshold of an absorption edge. Fig. 2.2 shows schematically one edge of an absorber. In a fluorescence mode experiment,  $\mu$  and  $\mu x$  ( $x$  is the sample thickness) is calculated by

$$\mu_x = \ln(I_f/I_0), \quad (2.12)$$

where  $I_f$  and  $I_0$  are intensities of the fluorescence and incident beams, respectively.

EXAFS spectrum generally refers to the region 40-1000 eV above the absorption edge. From an EXAFS spectrum the type of neighbors, the coordination number, the distance between the central and the neighboring atoms, and the Debye-Waller factors (DW) can be deduced by data analysis. Near or below the edge, there generally appear absorption peaks due to excitation of core electrons to some bound states (1s to  $nd$ ,  $(n+1)s$ , or  $(n+1)p$  orbital for  $K$  edge, and  $2s$  for  $L_I$  edge,  $2p$  for  $L_{II}$ ,  $L_{III}$  edges to the same set of vacant orbital, *etc*)[12]. This pre-edge region contains valuable bonding information such as the energy of virtual orbital, the electronic configuration, and the site symmetry. The edge position also contains information about the charge on the absorber. In between the

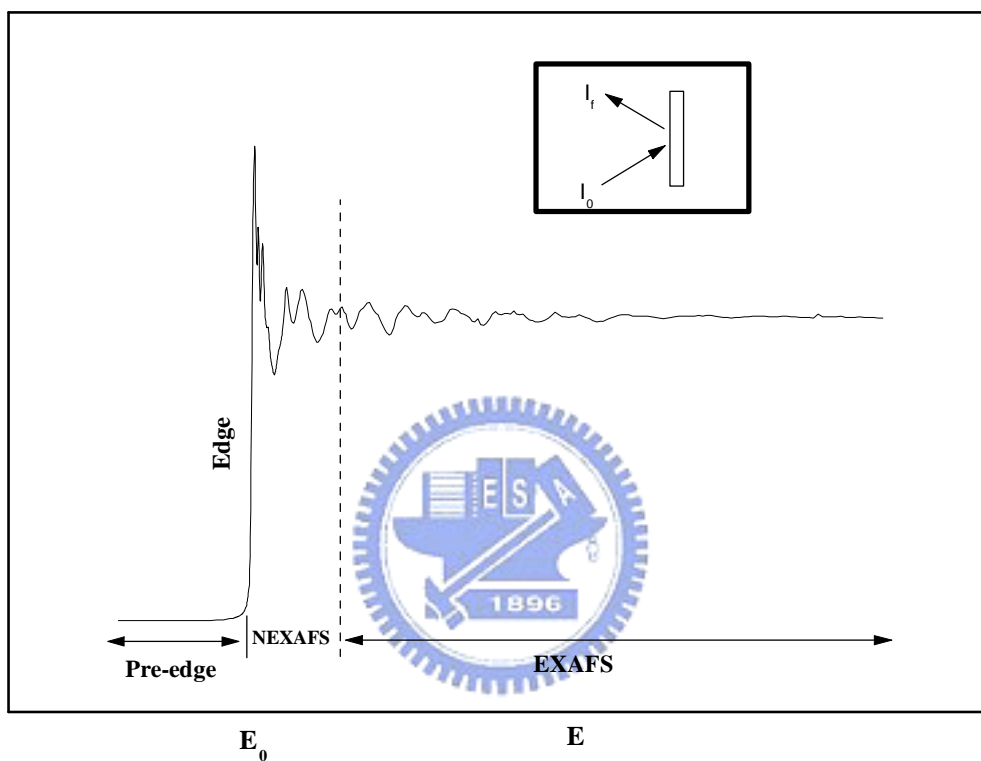


Figure 2.2: Schematic representation of the fluorescence yield mode and the resulting  $x$ -ray absorption spectrum  $\mu_x$  vs  $E$ .

pre-edge and the EXAFS regions is the near  $x$ -ray absorption fine structure (NEXAFS) which we have discussed in the previous section arises from effects such as many-body interactions, multiple scattering, distortion of the excited state wavefunction by the Coulomb field, band structures, *etc.*

EXAFS is a final state interference effect involving scattering of the outgoing photoelectron from the neighboring atoms. From a qualitative viewpoint, the probability that an  $x$ -ray photon will be absorbed by a core electron depends on both the initial and the final states of the electron. The initial state is the localized core level corresponding to the absorption edge. The final state is that of the ejected photoelectron which can be represented as an outgoing spherical wave originating from the  $x$ -ray absorbing atom. If the absorbing atom has a neighboring atom, the outgoing photoelectron wave (solid line in Fig. 2.3) will be backscattered by the neighboring atom, thereby producing an incoming electron wave (dashed line).

The final state is then the sum of the outgoing and all the incoming waves, one from each neighboring atom. The coefficient  $\mu$  of EXAFS is the interference between the outgoing and the incoming waves that give rise to the sinusoidal-like variation.

The  $x$ -ray absorption coefficient  $\mu$  is a function of photon energy  $E$  above the threshold of an absorption edge, and can be clearly revealed after the subtraction of the atomic absorption, *i.e.* the absorption of the central atom in the absence of

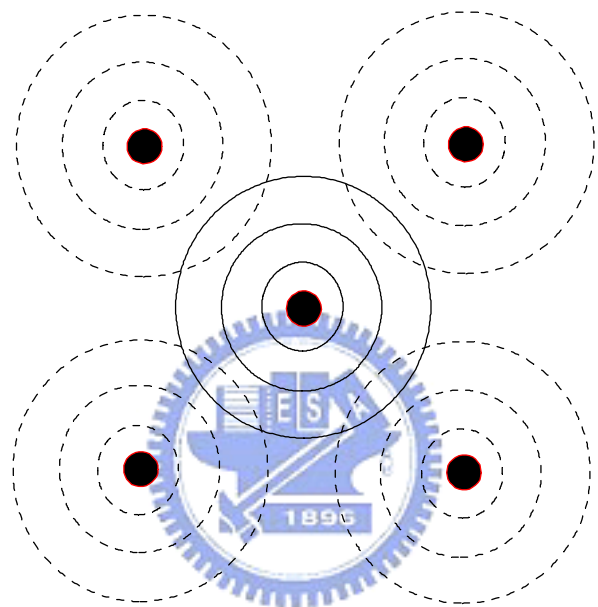


Figure 2.3: The Model of interference effect of EXAFS.

neighboring atoms. For reasonably high energy ( $\geq 60$  eV) and modulate thermal or static disorders, the modulation of absorption rate in EXAFS, normalized to the “background” absorption ( $\mu_0$ ) is given by

$$\chi(E) = \frac{\mu(E) - \mu_0(E)}{\mu(E)}. \quad (2.13)$$

In order to relate  $\chi(E)$  to structural parameters, it is necessary to convert the energy  $E$  into the photoelectron wavevector  $k$  via Eq. (2.14):

$$k = \sqrt{\frac{2m}{\hbar^2}(E - E_0)}. \quad (2.14)$$

Here  $E$  is the incident photon energy and  $E_0$  is the threshold energy of that particular absorption edge. This transformation of  $\chi(E)$  in  $E$  space gives rise to  $\chi(k)$  in  $k$  space where

$$\chi(k) = \sum A_j(k) \sin [2kr_j + \varphi_{ij}(k)], \quad (2.15)$$

and

$$A_j(k) = \frac{1}{kr_j^2} N_j S_i(k) F_j(k) \exp(-2\sigma_j^2 k^2) \exp\left(\frac{-2r_j}{\lambda_j(k)}\right). \quad (2.16)$$

Here  $F_j(k)$  is the backscattering amplitude from each of the  $N_j$  neighboring atoms of the  $j$ th type with a Debye-Waller factor of  $\sigma_j(k)$  to account for thermal vibration (assuming harmonic vibration) and static disorder (assuming Gaussian pair distribution) and at a distance  $r_j$  away.  $\varphi_{ij}(k)$  is the total phase shift, which contains contributions from both the absorb and the backscatter and affects the origins of the sine wave and its frequency. The term  $\exp(-2r_j/\lambda_j(k))$  is due to inelastic losses in the scattering process (due to neighboring atoms and the medium

in between) with  $\lambda_j(k)$  being the electron mean free path.  $S_i(k)$  is an amplitude reduction factor due to many-body effects such as shake-up/shake-off processes at the central atom (denoted by  $i$ ). The term  $1/kr_j^2$  presents that the outgoing or incoming wave is a spherical surface wave. It is clear that each EXAFS wave is determined by the backscattering amplitude ( $N_j F_j(k)$ ), modified by the reduction factors  $S_i(k)$ ,  $\exp(-2\sigma_j^2(k)k^2)$ , and  $\exp(-2r_j/\lambda_j(k))$ , and the  $1/kr_j^2$  distance dependence, and the sinusoidal oscillation which is a function of interatomic distances ( $2kr_j$ ) and the phase shift ( $\varphi_{ij}(k)$ ). So the sinusoidal oscillation of EXAFS is caused by interference  $\sin(2kr)$  term with a frequency  $2r$  in  $k$  space.



EXAFS can be applied in both crystalline and amorphous materials and it can be also applied to detect local lattice distortions. The common detection schemes in the soft  $x$ -ray range are the total electron yield (TEY) and fluorescence yield (FLY) modes. The TEY mode is surface sensitive and meticulous surface preparation and cleaning are required in order to avoid contributions from surface contaminants. The FLY mode is bulk sensitive and is thus better suited when the bulk material properties are sought. The fluorescence yield mode can suffer from self-absorption effects that affect mostly the amplitude of the EXAFS spectrum and thus the calculated coordination numbers and the Debye-Waller factors.

## 2.3 Theory of Surface States in Metal-Semiconductor Systems

Bardeen proposed a theory in 1947 [13] to explain the rectification characteristic of a metal–semiconductor contact. He showed that if the density of localized surface states having energies distributed in the semiconductor energy gap is sufficiently high, a double layer at the free surface of a semiconductor is formed from a net charge of carriers in surface states and a space charge of opposite sign. He concluded that this double layer will tend to make the work function independent of the Fermi level in the interior of the semiconductor, and the rectification characteristics of a metal–semiconductor contact are then practically independent of the metal. It is well known that such surface states and surface barriers do exist.[14] The surface states can occur either from the termination of the periodic structure of the semiconductor crystal at the surface or from the presence of adsorbed foreign atoms on the surface.

The data of Archer and Atalla[15] on metal contacts on cleaved silicon surface seems to indicate that for gold on cleaved silicon, there is good agreement between experiment and the simple theory proposed by Schottky[16] that the barrier height depends only on the work function of the metal and the semiconductor and is independent of the semiconductor doping. However, Mead and Spitzer[17] have studied the barrier height of metal–semiconductor systems for 14 IV and III-V semiconductors using cleaved semiconductor surface. In all cases, they report that the position of the Fermi level at the surface is essentially independent of

the metal work function and is very close to one third of the band gap from the valence-band edge.

The results of the experiments cited above are evidently quite different; the Schottky model seems to hold for Si-metal systems, but the results for the Mead and Spitzer experiments are in direct conflict with the Schottky theory. Nevertheless, Crowell, Sze, and Spitzer[18] have observed that the Fermi level at the metal–semiconductor interface is pinned in the relation to the valence-band edge. Referring to the work of Cowley and Sze[19], thus in this section, we derived the dependence of the barrier height on metal work function, surface states, and the thickness of the interfacial layer for the metal–*p*-type semiconductor systems.

The energy band diagram of a metal–*p*-type semiconductor contact is shown in Fig. 2.4. The various quantities used in the derivation which follows are defined in this figure. The first quantity which is of interest to us is the  $q\phi_0$ ; this energy is measured from the conduction-band edge at the semiconductor surface and specifies the level above which all surface states must be filled for charge neutrality at the semiconductor surface. The second quantity is  $q\phi_{Bp}$ , the barrier height of the metal-semiconductor contact;  $q\phi_{Bp}$  is the energy needed by a hole at the Fermi level in the metal to enter the valence band of the semiconductor, and includes the effect of the image force lowering  $q\Delta\phi$ . The interfacial layer will be assumed to have a thickness of a few angstroms and will be assumed transparent to holes whose energy is greater than the potential barrier.



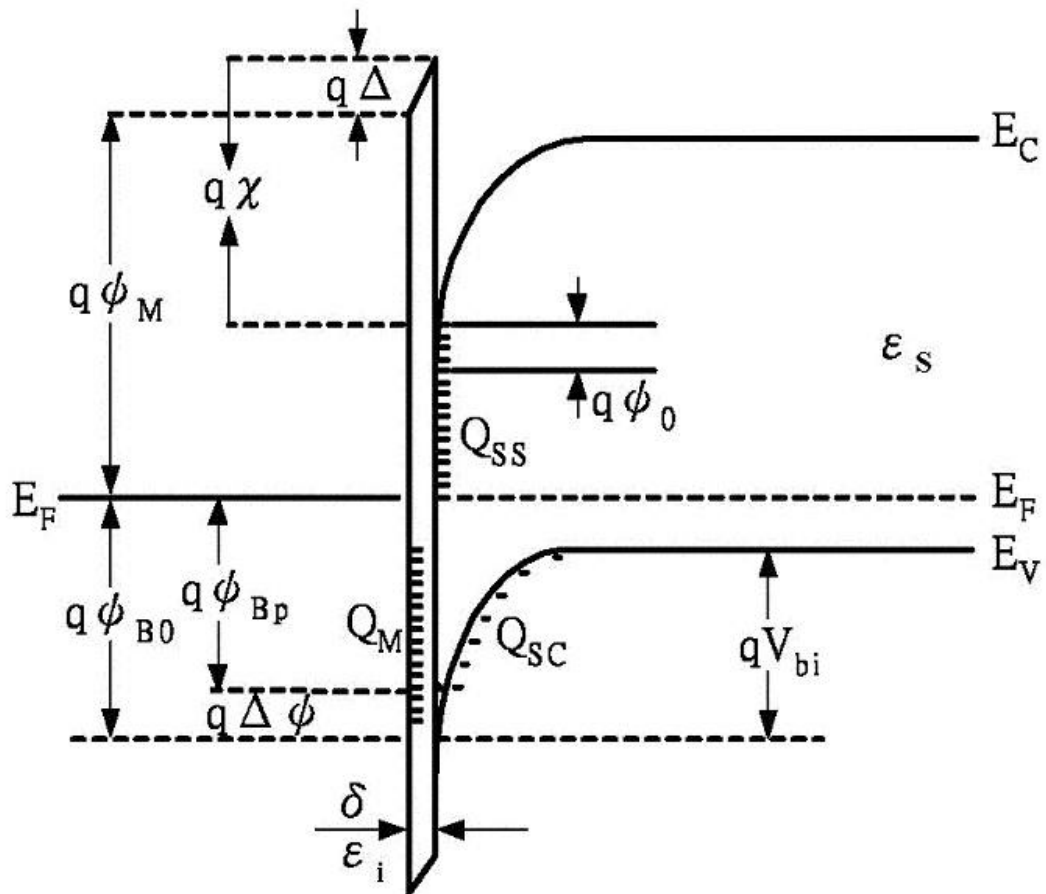


Figure 2.4: Energy band diagram of a metal-*p*-type semiconductor contact with an interfacial layer.

First we consider a  $p$ -type semiconductor with donor surface states whose density is  $D_s$  states/cm<sup>2</sup>/eV, and assume as did Bardeen,[13] that  $D_s$  is a constant over the energy range from  $q\phi_0$  to the Fermi level. For a uniform distribution the surface state charge density on the semiconductor  $Q_{ss}$  is given by

$$Q_{ss} = qD_s \left[ \frac{E_g}{q} - (\phi_0 + \phi_{Bp} + \Delta\phi) \right] \text{ (C/cm}^2\text{)}, \quad (2.17)$$

where  $\Delta\phi$  is the image force barrier lowering[20] and  $q$  is the electron charge. The quantity in parentheses is simply the difference between the Fermi level at the surface and  $q\phi_0$ .  $D_s$  times this quantity yields the number of surface states below which are full.

The space charge which forms in the depletion layer of the semiconductor can be expressed as an equivalent surface charge density, which is the net charge/cm<sup>2</sup> looking into the bulk semiconductor from a point just inside the semiconductor surface. The charge is obtained by solving Poisson's equation for the depletion layer of the semiconductor and can be written as

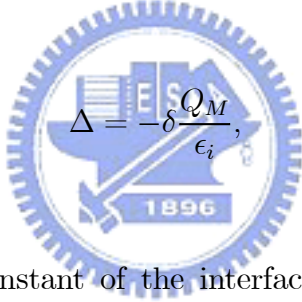
$$Q_{sc} = -\sqrt{2q\epsilon_s N_a (\phi_{Bp} + \Delta\phi - V_p - \frac{kT}{q})} \text{ (C/cm}^2\text{)}, \quad (2.18)$$

where  $N_a$  is the acceptor density of the bulk semiconductor. Equation (2.18) is valid only if there is no inversion layer in the semiconductor. The total equivalent surface charge density on the semiconductor surface is given by the sum of Eqs. (2.17) and (2.18). In the absence of any space charge effects in the interfacial layer, an exactly equal and opposite charge  $Q_M$  develops on the metal surface.

For thin interfacial layers, such effects are negligible, and  $Q_M$  can be written as

$$\begin{aligned}
 Q_M &= -(Q_{ss} + Q_{sc}) \\
 &= -qD_s \left[ \frac{E_g}{q} - (\phi_0 + \phi_{Bp} + \Delta\phi) \right] \\
 &\quad + \sqrt{2q\epsilon_s N_a (\phi_{Bp} + \Delta\phi) - V_p - \frac{kT}{q}}.
 \end{aligned} \tag{2.19}$$

The potential energy  $q\Delta$  across the interfacial layer with no voltage applied to the junction can be obtained by the application of Gauss' law to the surface charge on the metal and semiconductor:



$$\Delta = -\delta \frac{Q_M}{\epsilon_i}, \tag{2.20}$$

where  $\epsilon_i$  is the dielectric constant of the interfacial layer and  $\delta$  its thickness.

Another relation for  $\Delta$  can be obtained by inspection of the energy band diagram of Fig. 2.4:

$$\Delta = \left( \frac{E_g}{q} - \phi_M + \chi \right) - (\phi_{Bp} + \Delta\phi). \tag{2.21}$$

This results from the fact that the Fermi level must be constant throughout the metal–interfacial-layer–semiconductor system at equilibrium.

If  $\Delta$  is eliminated from Eqs. (2.20) and (2.21), and Eq. (2.19) is used to

substitute for  $Q_M$ , we obtain

$$\begin{aligned}
& \left(\frac{E_g}{q} - \phi_M + \chi\right) - (\phi_{Bp} + \Delta\phi) \tag{2.22} \\
&= \frac{q\delta D_s}{\epsilon_i} \left[\frac{E_g}{q} - (\phi_0 + \phi_{Bp} + \Delta\phi)\right] \\
&\quad - 2\sqrt{\frac{2q\epsilon_s N_a \delta^2}{\epsilon_i^2} (\phi_{Bp} + \Delta\phi) - V_p - \frac{kT}{q}}.
\end{aligned}$$

Equation (2.22) can now be solved for  $\phi_{Bp}$ . Introducing the quantities  $b_1$  and  $b_2$ :

$$b_1 = \frac{8q\epsilon_s N_a \delta^2}{\epsilon_i^2}, \tag{2.23a}$$

$$b_2 = \frac{\epsilon_i}{\epsilon_i - q\delta D_s}, \tag{2.23b}$$

we can write the solution to (2.22) as

$$\begin{aligned}
\phi_{Bp} &= \left[ b_2 \left(\frac{E_g}{q} - \phi_M + \chi\right) + (1 - b_2) \left(\frac{E_g}{q} - \phi_0\right) - \Delta\phi \right] \tag{2.24} \\
&\quad + \left\{ \frac{b_2^2 b_1}{2} - b_2 \sqrt{b_2} \left[ b_1 \left(\frac{E_g}{q} - \phi_M + \chi\right) \right. \right. \\
&\quad \left. \left. + \frac{(1 - b_2) b_1}{b_2} \left(\frac{E_g}{q} - \phi_0\right) - \frac{b_1}{b_2} \left(V_p + \frac{kT}{q}\right) + \frac{b_2 b_1^2}{4} \right]^{\frac{1}{2}} \right\}.
\end{aligned}$$

Equation (2.23a) can be used to calculate  $b_1$  if values of  $\delta$  and  $\epsilon_i$  are estimated:

For vacuum-cleaved or well-cleaned semiconductor substrates the interfacial layer will have a thickness of atomic dimensions, i.e., 4 or 5 Å. The dielectric constant of such a thin layer can be well approximated by the free-space value, and since this approximation represents a lower limit for  $\epsilon_i$ , it leads to an overestimation of  $b_1$ . For  $\epsilon_s \cong 10\epsilon_i$  and  $N_a \leq 10^{18} \text{ cm}^{-3}$ ,  $b_1$  is small, of the order of 0.01 eV, and

the  $\{ \}$  term in Eq. (2.24) is estimated to be less than 0.04 eV. Neglect of the  $\{ \}$  term in Eq. (2.24) reduces the equation to

$$\begin{aligned}\phi_{Bp} &= b_2\left(\frac{E_g}{q} - \phi_M + \chi\right) + (1 - b_2)\left(\frac{E_g}{q} - \phi_0\right) - \Delta\phi \\ &\equiv -b_2\phi_M + b_3.\end{aligned}\quad (2.25)$$

If  $b_2$  and  $b_3$  can be determined experimentally and if  $\chi$  is known, then using the measured values we can determine  $\phi_0$  from the relation

$$\phi_0 = \frac{1}{1 - b_2} \left[ \frac{E_g}{q} - (-b_2\chi + b_3 + \Delta\phi + 2b_2\phi_M) \right], \quad (2.26)$$

and from (2.23b) a relation for determining  $D_s$  is

$$D_s = \frac{b_2 - 1}{b_2} \frac{\epsilon_i}{q\delta}. \quad (2.27)$$

Using the previous assumptions for  $\delta$  and  $\epsilon_i$ , Eq. (2.27) becomes

$$D_s \cong 10^{13} \frac{b_2 - 1}{b_2} \text{ (states/cm}^2\text{/eV)}. \quad (2.28)$$

Two special cases of Eq. (2.25) are of interest:

(1) When  $b_2 \rightarrow 0$ , then

$$\phi_{Bp} \cong \left(\frac{E_g}{q} - \phi_0\right) - \Delta\phi. \quad (2.29)$$

In this case the Fermi level at the interface is "pinned" by the surface states at the value  $\phi_0$  below the conduction band. The barrier height is independent of the metal work function, and is determined entirely by the doping and the surface properties of the semiconductor.

(2) When  $b_2 \rightarrow 1$ , then

$$\phi_{Bp} \cong \left( \frac{E_g}{q} - \phi_M + \chi \right) - \Delta\phi. \quad (2.30)$$

This is recognized as the familiar expression (except for the  $\Delta\phi$  term) for the barrier height of a simple Schottky barrier where surface effects are neglected.

In summary, the dependence of the barrier height of metal-semiconductor systems upon the metal work function is derived based on the following assumptions:

(1) the contact between the metal and the semiconductor has an interfacial layer of the order of atomic dimensions; it is further assumed that this layer is transparent to holes with energy greater than the potential barrier but can withstand potential across it. (2) The surface state density (per unit area per electron volt) at the interface is a property only of the semiconductor surface and is independent of the metal. The barrier height  $\phi_{Bp}$  is defined here as the energy needed by a hole at the Fermi level in the metal to enter the valence band of semiconductor.

With the above assumptions, the barrier height for  $p$ -type semiconductor-metal contacts is found to be a linear combination of the metal work function  $\phi_M$  and a neutral level  $\phi_0$  which is defined as the energy above which the surface states must be filled for charge neutrality at the semiconductor surface. The energy  $\phi_0$  is measured from the edge of conduction band in the metal- $p$ -type semiconductor systems, and is very close to two-thirds of the band gap from the conduction-band edge[19]. For constant surface state density the theoretical expression obtained is

$$\phi_{Bp} = b_2 \left( \frac{E_g}{q} - \phi_M + \chi \right) + (1 - b_2) \left( \frac{E_g}{q} - \phi_0 \right) - \Delta\phi,$$

where  $\chi$  and  $E_g$  are electron affinity and the band gap of the semiconductor, respectively,  $\Delta\phi$  is the image force lowering, and  $b_2$  is a weighting factor which depends mainly on the surface state density and the thickness of the interfacial layer.



# CHAPTER 3

## EXPERIMENTAL DETAILS

The characterization systems used in this dissertation include Hall, current-voltage (I-V), capacitance-voltage (C-V), deep level transient spectroscopy (DLTS), photoluminescence (PL), Raman, *x*-ray diffraction, *x*-ray absorption fine structure (XAFS), secondary ion mass spectrometry (SIMS) and photcapacitance measurements. All the GaN films are grown by metalorganic vapor phase epitaxy (MOVPE) system. All the Schottky contacts are formed by electron-gun evaporation through metal masks. The following describes some of the details of experimental systems. Others are described in the section of experiments from chapter 4 to 9.



### 3.1 Hall Measurement Systems

The schematic drawing of the Hall system is shown in Fig. 3.1. The system contains a current source (Keithley, Model 220), a voltage meter (Keithley, Model 196), a current meter (DMM, Model 485), and a scanner (Keithley, Model 705). The magnetic field used in the measurement is about  $10^4$  Gauss. To assure good ohmic metal-contacting characteristics of *n*-type and *p*-type samples, the In and Ni/Au metal contacts in N<sub>2</sub> ambient were annealed with 500 °C thermal annealing



(TA) for 15 minutes and with 700 °C rapid temperature annealing (RTA, ramping rate of 140 °C/sec) for 10 seconds, respectively.

### 3.2 Electrical Characterization Systems

The electrical characterizations contain the current-voltage (I-V), capacitance-voltage (C-V), transient capacitance (C-t) and deep level transient spectroscopy (DLTS) measurements. They consist chiefly of HP4145B and HP4194A with GPIB interface, and temperature controller with the RS232 interface to communicate with the personal computer. The schematic layout of the electrical characterization systems is shown in Fig. 3.2

### 3.3 XAFS Systems



For the structure study of the nitride epilayers, the *x*-ray absorption fine structure (XAFS) measurements including near-edge (NEXAFS) and extend structure (EXAFS) were employed. The doping effect of Mg incorporation was examined by probing both nitrogen and gallium atoms due to lack of suitable *x*-ray energy for the magnesium atom. The nitrogen *K*-edge NEXAFS was recorded at the high-energy spherical grating monochromator (HSGM, BL20A) of NSRRC in Hsin-Chu. The schematic layout of the HSGM beam line is shown in Fig. 3.3. The grating (700 lines/min) of the monochromator of BL20A is made of gold-coated fused silica and is suitable to cover the photon-energy range of from  $\sim 207$

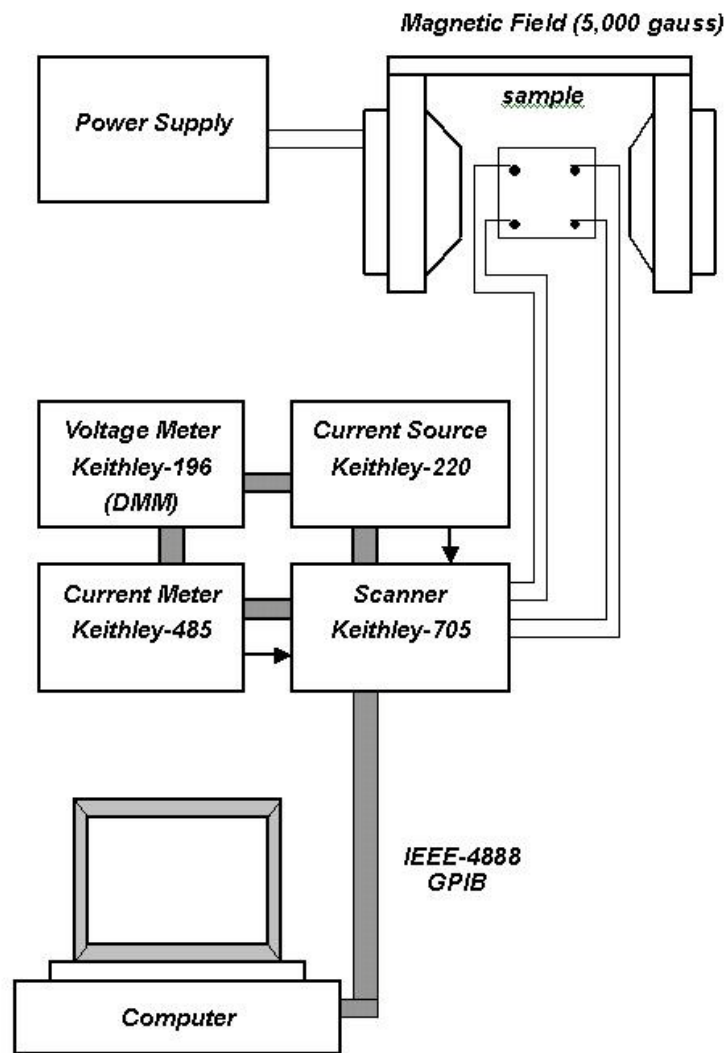


Figure 3.1: The schematic diagrams of the Hall measurement system.

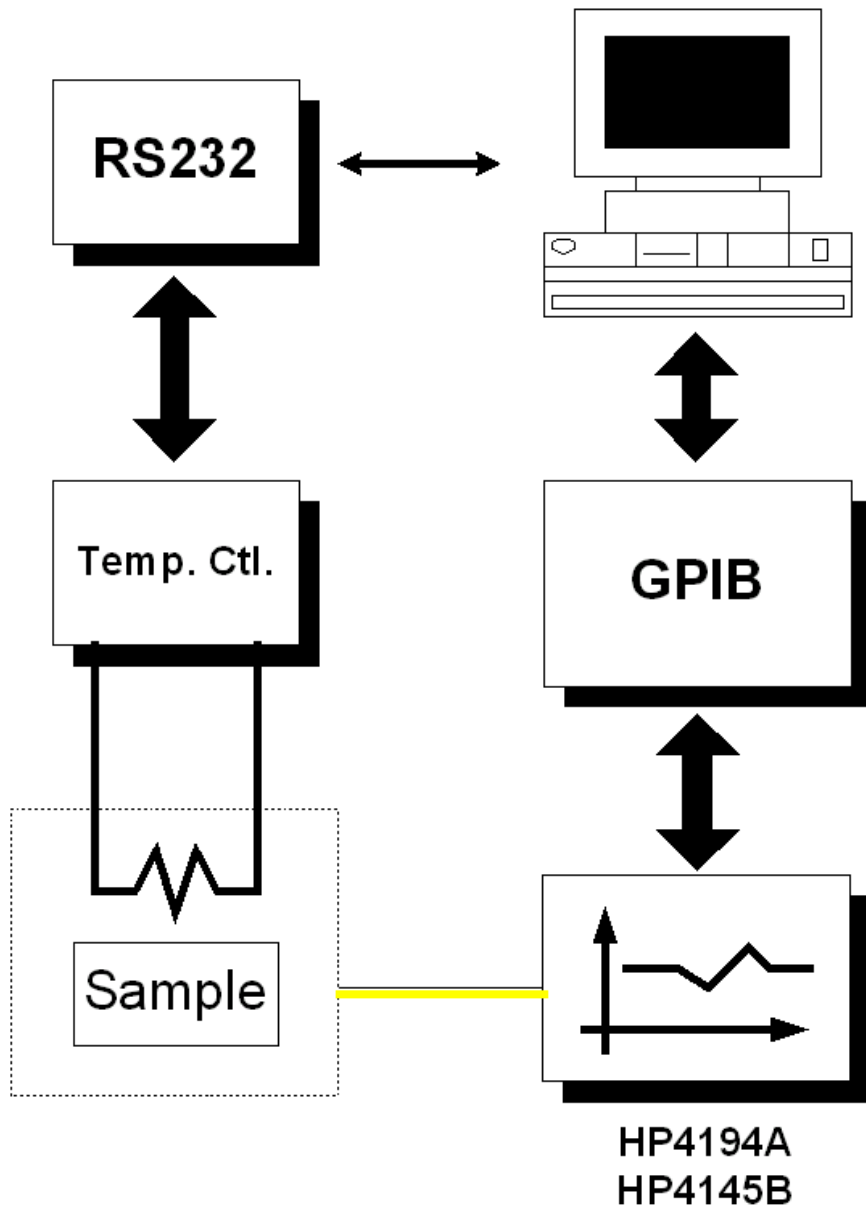


Figure 3.2: The schematic layout of the electrical characterization systems.

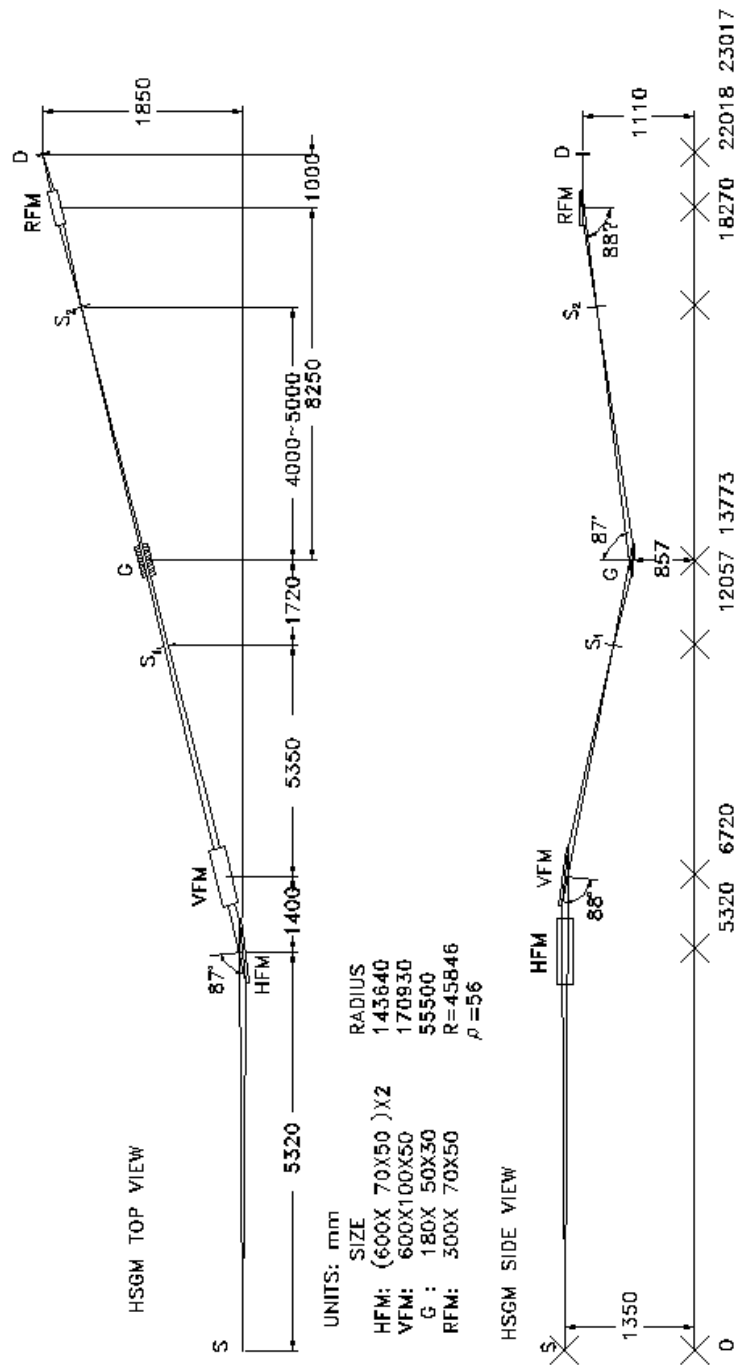


Figure 3.3: The optical layout of the 6m-HSGM beamlines. S is the radiation source. HFM and VFM are spherical mirrors. S1, S2 are the entrance and exit slits. G is a spherical grating. RFM is an toroidal mirror. D is sample position.

to  $\sim 517$  eV (see the second curve from the top in Fig. 3.4). The spectra were measured in fluorescence yield (FLY) mode with a high-purity and high-sensitivity seven-element Ge detector. The  $x$ -ray incident angle  $\theta$  was varied between  $0^\circ$  and  $80^\circ$  with respect to the norm of the substrate. The samples were kept at room temperature, under a chamber pressure of better than  $5 \times 10^{-9}$  torr. The typical resolution of the spectra was better than 0.2 eV. The beam size at the sample is less than  $1.5 \times 1.0$  mm<sup>2</sup>.

The gallium  $K$ -edge EXAFS spectrum was performed at the Wiggler beam line (BL17C) of NSRRC. This layout of this beamline is shown in Fig. 3.5. The schematic beam line arrangement of the Wiggler BL17C beam line with some major components is shown in Fig. 3.6. A Si (111) double-crystal monochromator with a 0.5 mm entrance slit was used for energy scanning, which covered a wide photon energy ranging from 0.8 to 15 KeV with a resolving power of  $>7,000$ . The intensities of the incident beam and the fluorescence were measured by a N<sub>2</sub>-filled ionization chamber and an argon-filled Stern-Heald-Lytle detector. To suppress second order and scattered lights from the monochromator, a thickness of 6-absorption length Zn-filter was placed between the sample and the window of the Stern-Heald-Lytle detector for Ga  $K$ -edge absorption. Such an arrangement effectively reduced the noise level resulting from the scattering of  $x$ -ray by the sample or the surrounding air. The typical  $x$ -ray absorption spectrum experiment equipment is shown in Fig. 3.7.

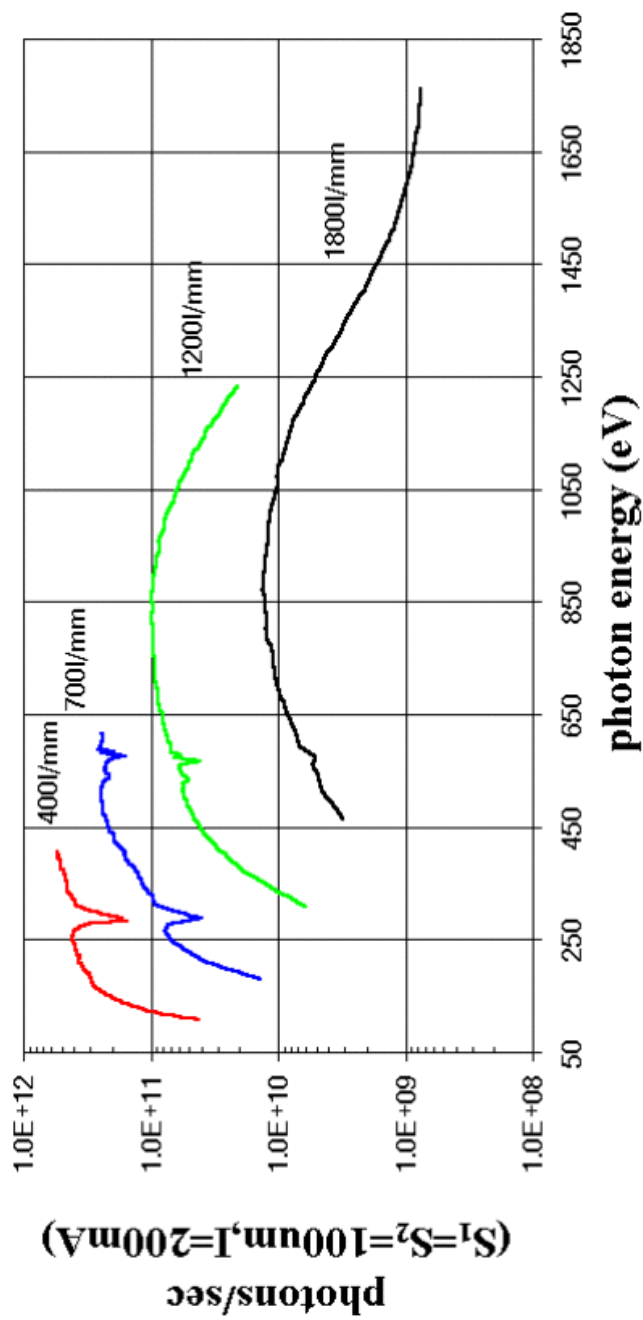


Figure 3.4: The relationship between intensities of different gratings and the photon energy. The curve labeling 700  $l/mm$  is pertinent to our experiment.

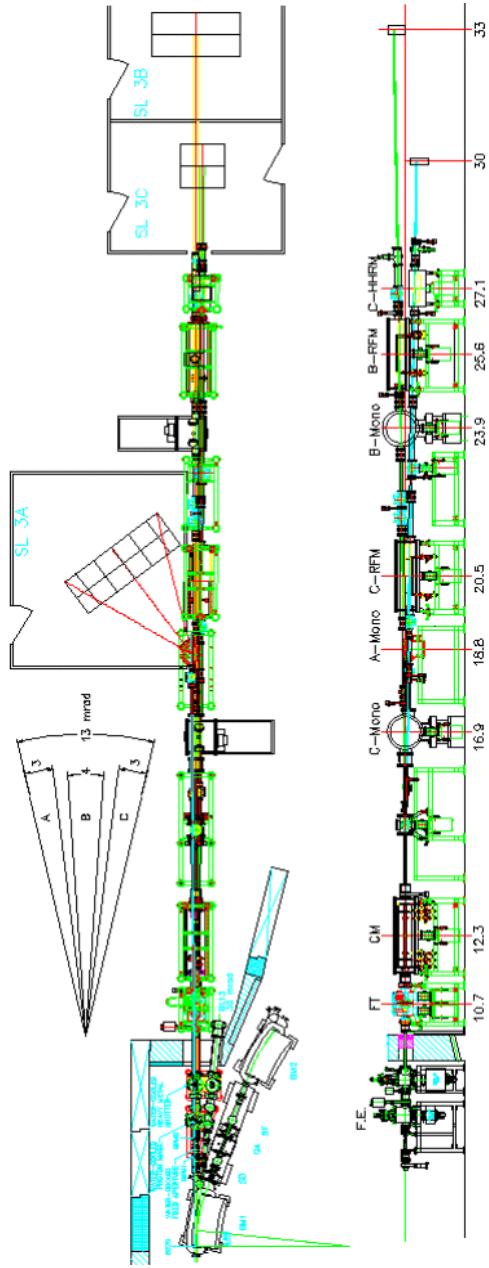


Figure 3.5: Wiggler X-ray beamline layout. Where FE:Front-end, FT:Filter tank, CM:Collimating mirror, Mono: Monochromater, RFM:Re-focusing mirror, HHRM:High-order harmonic rejection mirror.

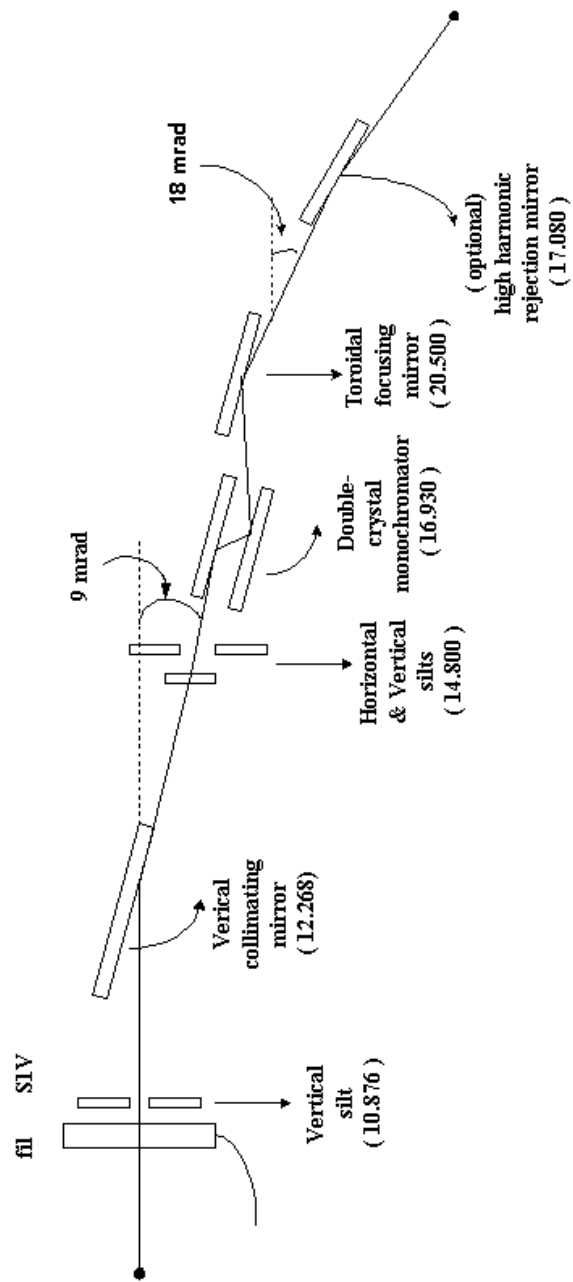


Figure 3.6: Some major components of the Wiggler-C (BL17C) beam line.



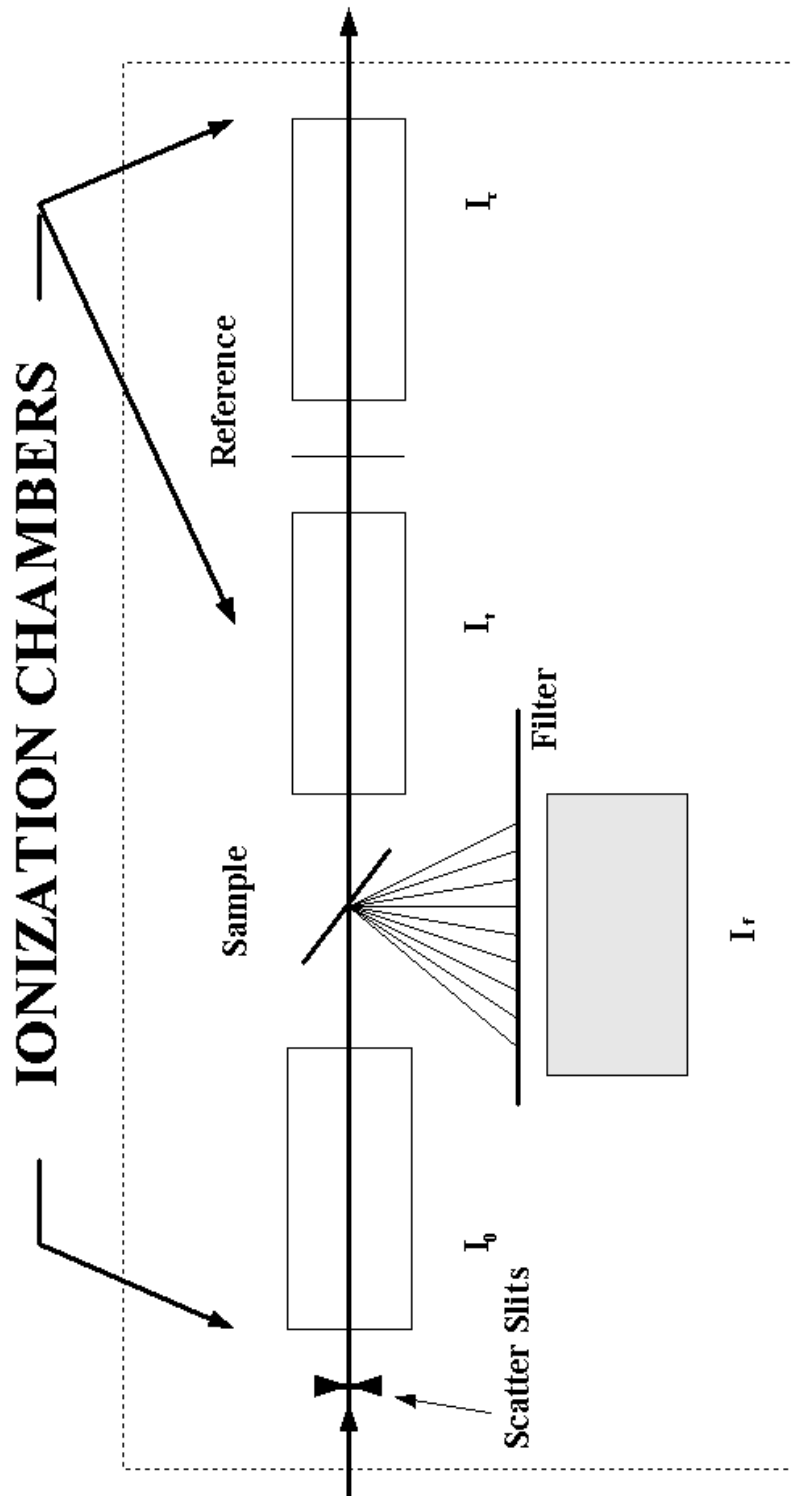


Figure 3.7: The typical X-ray absorption spectrum detecting system of BL17C.

## CHAPTER 4

### ISOELECTRONIC IN-DOPING EFFECTS IN GAN

#### 4.1 Introduction

III-V nitrides have been a subject of intense investigation for applications in optoelectronic devices such as high-temperature transistors[21], blue and green light-emitting diodes and violet laser diodes[22]. During the past decade, material quality of GaN in terms of carrier mobility, dislocations,  $p$ -type doping and metal contacts has been indeed improved greatly, however, to obtain a device quality sample is still an uneasy task. It has been reported that deep-level defects are one of the principle factors impeding the performance of GaN-based transistors[23]. Such defects can generally cause nonradiative recombinations in the active layer and result in an increase of threshold current in nitride semiconductor laser diode. Varieties of growth techniques have been employed to improve the crystalline quality, among them isoelectronic doping has been proved to be a viable method in reducing the unintentional impurity dislocation as well as deep level concentrations. For example, nitrogen in GaP can form isoelectronic center and increase the quantum efficiency by approximately two-order of magnitude in this indirect material system[24]. The commonly used GaAs film doped with iso-

electronic indium doping has also shown an order of magnitude in reduction of dislocation density[25]. However, up to date very few literary reports have been addressed on this issue on GaN, we thus attempt to study isoelectronic effects in GaN with small amount of In doping using current-voltage ( $I$ - $V$ ) measurement and deep level transient spectroscopy (DLTS) so as to determine the changes in their  $I$ - $V$  and deep level characteristics. Our results indicate that the electronic properties of isoelectronically doped GaN can be improved as compared to the undoped sample.

## 4.2 Experiments

The undoped and In-doped GaN films were grown on (0001) sapphire substrates at a temperature of 1100°C by a low-pressure horizontal metalorganic vapor phase epitaxy (MOVPE) reactor. For undoped GaN growth, ammonia ( $\text{NH}_3$ ) and trimethylgallium (TMGa) were used as the N and Ga precursors with flow rates of 3 standard liter per minute and 133  $\mu\text{mol}/\text{min}$ , respectively. The growth condition for iso-doped sample was almost the same as undoped one, except that a flow rate of 25.5  $\mu\text{mol}/\text{min}$  of TMIIn was introduced into the reactor during the sample preparation. Since the indium atom appears very difficult to enter into the solid at high growth temperatures, the resulted In/Ga ratio in the solid is less than 0.2%, as determined by secondary ion mass spectrometry. Photoluminescence (PL) and Raman measurements further confirms isoelectronic doping

properties of our GaN:In film because neither PL emission wavelength shift, nor phonon vibration mode broadening is observed. Hall measurement reveals that the electron carrier concentrations and mobilities are  $4.70 \times 10^{16} \text{ cm}^{-3}$ ,  $77 \text{ cm}^2/\text{V}\cdot\text{s}$  for undoped GaN and  $8.21 \times 10^{16} \text{ cm}^{-3}$  and  $88 \text{ cm}^2/\text{V}\cdot\text{s}$  for doped one. It seems that the Hall properties do not change significantly at this isoelectronic doping level.

Prior to the diode fabrication, the as-grown GaN sample was cleaned in successive rinses of acetone, isopropyl alcohol and D. I. water for 5 min each with ultrasonic agitation and etched by HCl: H<sub>2</sub>O= 1:1 for 10 min. Ni and Al metals were then deposited on the top of GaN films to form Schottky and ohmic contacts by electron-gun evaporation through metal masks.

### 4.3 Results and Discussion



Figure 4.1 shows the room temperature current density-voltage ( $J$ - $V$ ) characteristics of Ni Schottky diodes on both undoped and In-doped GaN epilayers. The forward  $J$ - $V$  characteristics was expressed according to the thermionic emission theory[26]:

$$J = J_s \left[ \exp \left( \frac{V - IR_s}{nkT} \right) - 1 \right], \quad (4.1)$$

where  $J_s$  is the saturation current density,  $R_s$  is the series resistance,  $n$  is the ideality factor for our GaN diodes. These results were presented in Table 4.1. As can be seen in the table, the ideality factor can be improved from 1.20 to 1.06 and

Samples	$n$	$J_s$ (A/cm <sup>-2</sup> )	$R_s$ (k $\Omega$ )
Undoped	1.20	$1.02 \times 10^{-7}$	13.80
In-doped	1.06	$1.27 \times 10^{-9}$	2.40

Table 4.1: Results of forward bias I-V measurement for undoped and isoelectronic In-doping GaN films.

the calculated saturation current, based on the ideal diode law, can be reduced from  $1.02 \times 10^{-7}$  to  $1.27 \times 10^{-9}$  A/cm<sup>2</sup>. Since the ideality factor is closely related to the interface states between the metal-semiconductor and deep levels in the space-charge region, the improvement in diode quality could be ascribed in part to the reduction of these defects when small quantities of In is doped into the epilayer. This point will be addressed in more detailed later using DLTS measurement. Moreover, it is observed that the series resistance of the diode is also lowered by isoelectronically In doping. Note that the series resistance of a Schottky diode is composed of the resistance of quasi-neutral region and resistance of the ohmic contact in the diode. Because the difference of carrier concentration and mobility product in quasi-neutral region is only about two-fold in magnitude, we believed that the decrease of diode series resistance is stemmed largely from the improved ohmic contact characteristics owing to the isoelectronic doping effects.

The DLTS spectra of both undoped and In-doped GaN films are shown in Fig. 4.2. Two distinct trap peaks were clearly observed at the temperatures of 113 and 269 K in undoped GaN film, at the rate window of  $1.65 \text{ s}^{-1}$ . From the

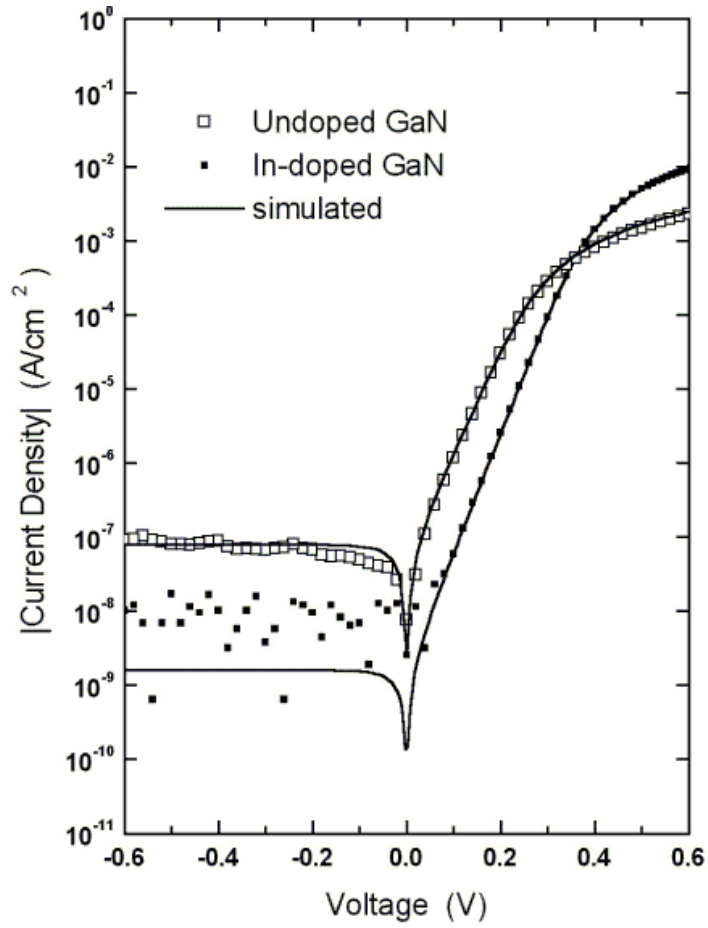


Figure 4.1: Room temperature current density-voltage characteristics of Ni-GaN Schottky diodes.

	$E1$	$\sigma_{E1}$	$N_{E1}$	$E2$	$\sigma_{E2}$	$N_{E2}$
Sample	(eV)	(cm <sup>2</sup> )	(cm <sup>-3</sup> )	(eV)	(cm <sup>2</sup> )	(cm <sup>-3</sup> )
Undoped	0.149	$1.20 \times 10^{-18}$	$8.97 \times 10^{13}$	0.601	$5.80 \times 10^{-15}$	$8.49 \times 10^{14}$
In-doped	—	—	—	0.601	$3.97 \times 10^{-15}$	$1.43 \times 10^{14}$

Table 4.2: Results of deep level transient spectroscopy measurement for undoped and isoelectronic In-doping GaN films.

Arrhenius plot of Figure 4.3, we can find that the trap energy levels are located at  $E_C-0.149$  eV (labelled as E1) and  $E_C-0.601$  eV (labelled as E2) and their capture cross sections and trap concentrations are  $1.20 \times 10^{-18}$  cm<sup>2</sup>,  $8.97 \times 10^{13}$  cm<sup>-3</sup> and  $5.80 \times 10^{-15}$  cm<sup>2</sup>,  $8.49 \times 10^{14}$  cm<sup>-3</sup>, respectively. The detailed characteristics were listed in Table 4.2.

The energy level of  $E_C-0.149$  eV obtained from our experiments are comparable to the deep level  $\sim 0.26$  eV reported by Hacke *et al.* in their MOVPE[27] and hydride vapor phase epitaxy (HVPE) samples[28], 0.18 eV by Gotz *et al.*[29] and by Fang *et al.*[30] in as-grown and electron irradiated GaN films, 0.14 eV by Lee *et al.*[31] and 0.234 eV by Wang *et al.*[32] in reactive molecular beam epitaxy (MBE)-grown GaN sample. All these levels are generally believed to be the same defect level because of their similar patterns on the Arrhenius plots in Fig. 4.3. The other trap level,  $E_C-0.601$  eV, is also measured previously by Hacke *et al.*[28], Haase *et al.*[33], and Wang *et al.*[32], irrespective of different growth methods being used in preparing GaN samples. The fact of the presence of these

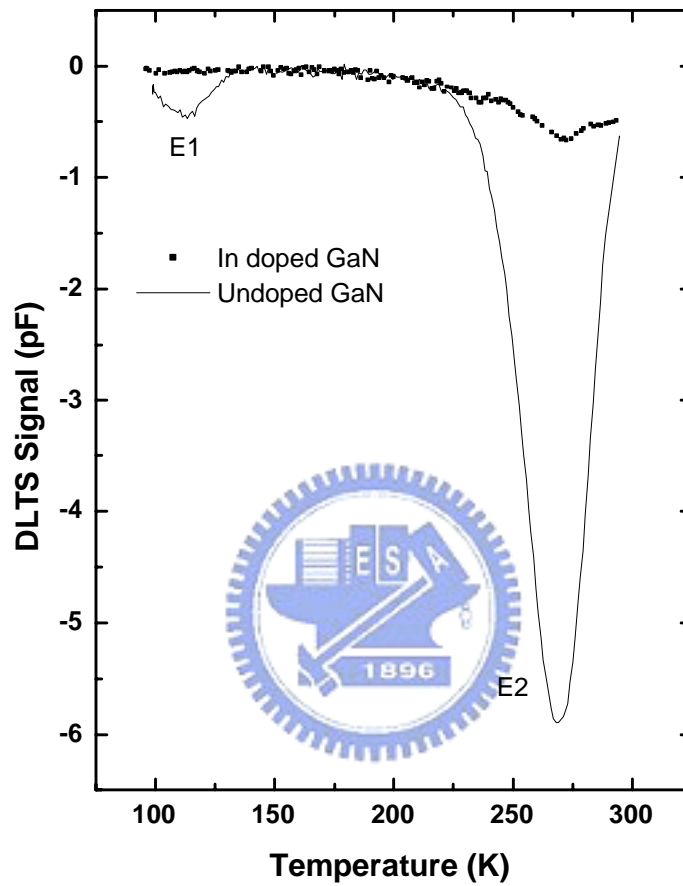


Figure 4.2: The DLTS spectra of undoped and In-doped GaN samples at rate window of  $1.65 \text{ s}^{-1}$ .



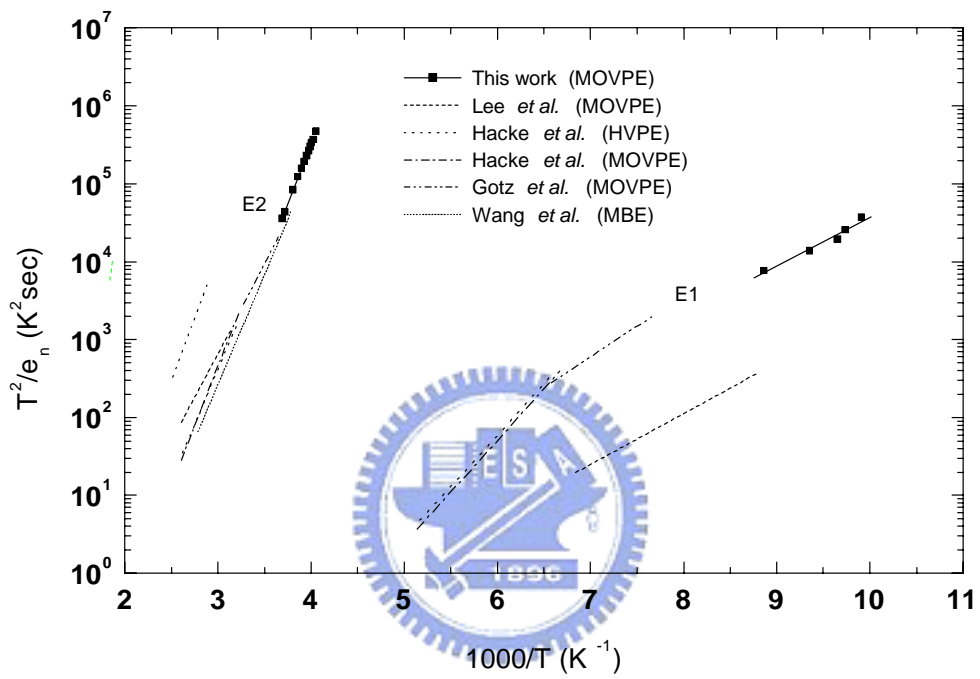


Figure 4.3: Arrhenius plot of the inverse emission rate times temperature squared vs reciprocal temperature for undoped GaN film.

traps seemingly independent of reacting chemical species and growth techniques suggests that their origins may come mainly from the native defects or related complexes, such as antisites, vacancies and interstitials. In regard to these deep levels, Fang *et al.*[30] believes that the trap at shallow level is associated with N vacancy after the comparison between the as-grown and electron irradiated GaN samples. The prominent trap at  $\sim 0.601$  eV in GaN film is likely due to the nitrogen antisite point defect ( $N_{Ga}$ ), as suggested by Hacke *et al.*[27] This argument agrees well with the prediction by Jenkins and Dow[34], who have shown that the deep level associated with N atom on a Ga site is at a location of  $\sim 0.52$  eV below the conduction band, fairly close to the experimental value.

In contrast to the undoped one, we measured almost no signal at  $E_C - 0.149$  eV for In-doped GaN film. The cause for such a appearance is not clear yet. If nitrogen vacancy is responsible for this defect level, it implies that the addition of small quantities of In atoms can help to suppress the formation of nitrogen vacancies during the deposition. This explanation is also consistent with our recent observations in In iso-doped GaN and InGaN studies[35]. In these experiments, we have found that the Ga incorporation efficiency is suddenly decreased when In atoms are introduced into the growth chamber, which will result in a higher effective V/III ratio in the growing interface and hence a decrease of nitrogen vacancy concentration in the solid. Moreover, it is known that In atom in conventional GaAs bulk crystal can greatly reduce the density of large dislocations

by pinning of dislocations at In atoms due to the large radius of In as compared to that of Ga[36]. Such a pinning action can generally withhold the generation of point defects, including the native defects, and improve the film quality. This may also occur in the case of GaN.

Additionally, we have also found that the concentration of  $E_C-0.601$  eV in isoelectronic In doped GaN sample decreases sharply from  $8.49 \times 10^{14} \text{ cm}^{-3}$  to  $1.43 \times 10^{14} \text{ cm}^{-3}$ , nearly an order of magnitude in reduction. It is reasonably to credit it to the dislocation pinning effect, as mentioned above; however, the migration of In surfacant may play an essential role as well. Due to a weaker In-N bond than that for Ga-N, the In atom is expected to have a much faster surface mobility on the growing surface, especially at high growth temperatures. This will enable the In atoms with a greater possibility in occupying normally vacant Ga sites in the growing crystal and thereby lowering the density of Ga vacancy-related defects. For that reason, the trap concentration of  $E_C-0.601$  eV defect level, which we ascribe to nitrogen antisite ( $N_{Ga}$ ), is reduced.

#### 4.4 Summary

In summary, we have performed the I-V and DLTS studies on undoped and isoelectronically In doped GaN samples. Experimental results reveal that when small quantities of In atoms is added into the epilayer, the commonly observed GaN defect levels, located at  $E_C-0.149$  and  $E_C-0.601$  eV, can be effectively sup-

pressed. The trap concentration of  $E_C-0.149$  eV defect is even decreased to a level undetected by our equipment. This study confirms that the isoelectronic doping technique is a simple, but yet effective method in reducing the concentrations of electron traps for GaN. The use of this technique may bring an improvement in GaN device performance, particularly for those films grown with large defect concentration.



## CHAPTER 5

# ISOELECTRONIC AS-IMPLANTED EFFECTS IN GAN

### 5.1 Introduction

III-V nitrides have been a subject of intensive investigations for applications in optoelectronic devices such as high-temperature transistor,[37] visible and ultraviolet light emitting diodes and laser diodes.[38, 39] Due to lack of lattice-matched substrate available for GaN, the epitaxial film is usually comprised with large concentrations of radiative or non-radiative defects, causing degradation of device performances and lifetime. In order to improve the material quality, varieties of techniques have been employed in preparing GaN film. These included the isoelectric doping, which has been proved to be capable of suppressing the formation of nonradiative centers, deep levels, as well as dislocations.[40] Recent theoretical calculations by Matilla *et al.*[41], and Van de Walle *et al.*[42] also showed that the isovalent doping using As atoms can produce energy levels deep into the bandgap of GaN, leading to an emission in the desired visible wavelength region. This prediction was confirmed by numbers of authors using primarily the optical measurements, such as Jadwisieniczak *et al.*[43], Guido *et al.*[44], Li *et al.*[45] and Winser *et al.*[46, 47] They reported that As doping and implanting of GaN could

improve the mobility[45], suppressed the yellow emission[47], and, more importantly, enhance the strong blue emissions at the peak positions of from 2.60 to 2.73 eV.[43, 44, 45, 46] Here, we conducted a series of Hall, current-voltage and deep level transient spectroscopy measurements of the As-implanted GaN films. Our results indicated that one additional deep level is generated at 0.769 eV below the conduction band, which is most likely to be As related.

## 5.2 Experiments

The undoped n-type GaN samples were grown on sapphire substrate using the metalorganic vapor phase epitaxy technique. The corresponding carrier concentration and mobility are about  $2 \times 10^{17} \text{ cm}^{-3}$  and  $318 \text{ cm}^2/\text{V}\cdot\text{s}$ , respectively. These samples were subsequently implanted with  $\text{As}^+$  ions with 50 keV at  $1 \times 10^{14}$  and  $5 \times 10^{15} \text{ cm}^{-2}$  dosage levels. They are labeled as As14 and As15, respectively. The distributions of As atoms in the GaN films were simulated by Trim programs and these results was presented in Fig. 5.1. These simulation results were in agreement with the data obtained with SIMS measurements.

## 5.3 Results and Discussion

The results of the Hall measurement are depicted in Fig. 5.2. We see the carrier concentration of the As-implanted film dropped considerably to a value of  $\sim 1.3 \times 10^{16} \text{ cm}^{-3}$ , nearly independent of As ion dosage. However, we do observe

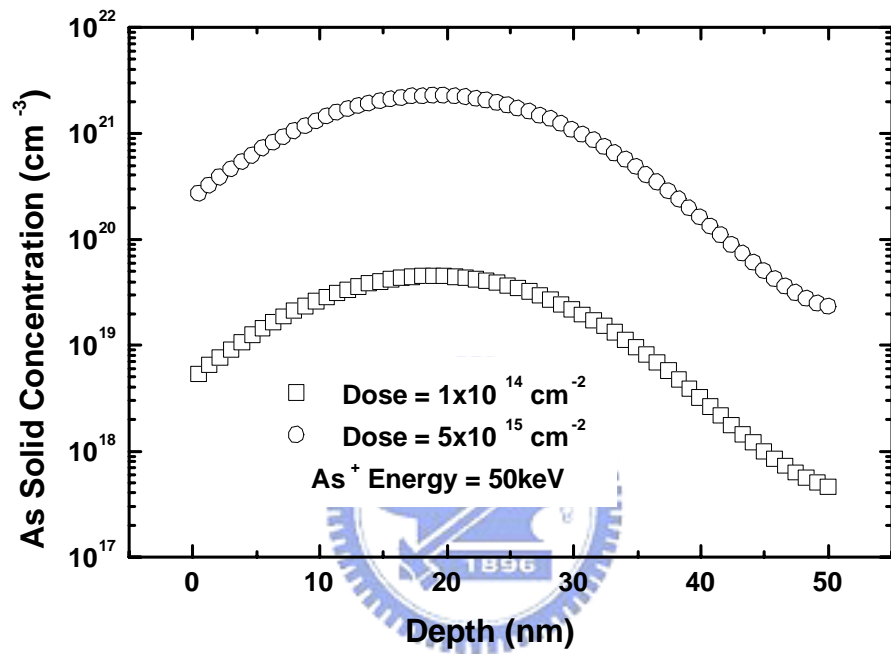


Figure 5.1: Distribution of implanted As atoms in GaN films with various dosage levels simulated by TRIM programs.

a greater difference on the mobility of the two ion dosages. The mobility of As-14 is  $275 \text{ cm}^2/\text{V}\cdot\text{s}$ , reduced only slightly from its original value. As for As-15, probably because of high implantation damages a highly resistive characteristic was observed, which gives almost a zero value in the mobility. Nonetheless, the subsequent thermal annealing process did help improving the film quality as was shown in Fig. 5.2. For implanted samples annealed at  $800^\circ\text{C}$ , we can find that both the carrier concentration and mobility recover back gradually with the increasing annealing time, and reach values nearly identical to that of as-grown one as the annealing time extending to 60 min.

After Hall measurements, Schottky diodes were fabricated on the 60 min-annealed samples (labeled as As14-60 and As15-60) to study the As implanting effects on GaN. Using the procedure published in previous literatures,[40, 48] the resulted current-voltage and Hall characteristics are summarized in Table 5.1. It is interesting to note that the annealed arsenic-implanted GaN film performed even better than the as-grown one. Not only the ideality factor is reduced from 1.387 to 1.227, but also the Schottky barrier height and reverse current density are improved substantially from 0.744 eV and  $4.90 \times 10^{-7} \text{ A}/\text{cm}^2$  to 0.927 eV and  $3.77 \times 10^{-10} \text{ A}/\text{cm}^2$ , respectively.

To investigate whether there are electrically active As-induced defects generated in the bandgap, we performed the deep-level transient spectroscopy (DLTS) measurements. The results of As14-60 and As15-60 are shown in Fig. 5.3. For



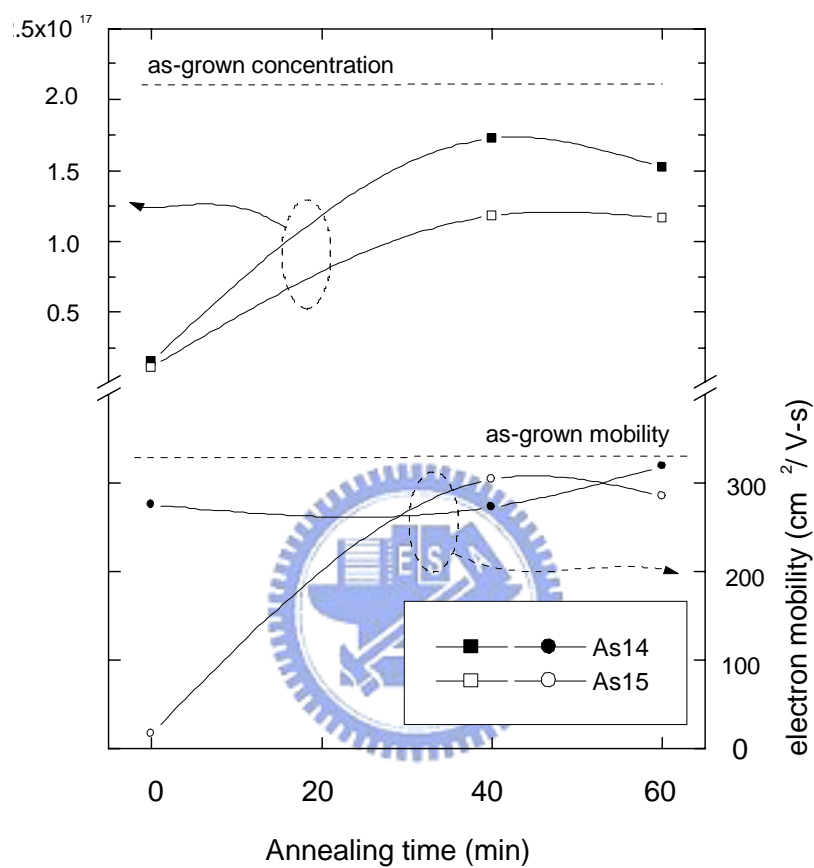


Figure 5.2: Carrier mobility and concentration of GaN films with various As-implanted dosage vs the annealing time.

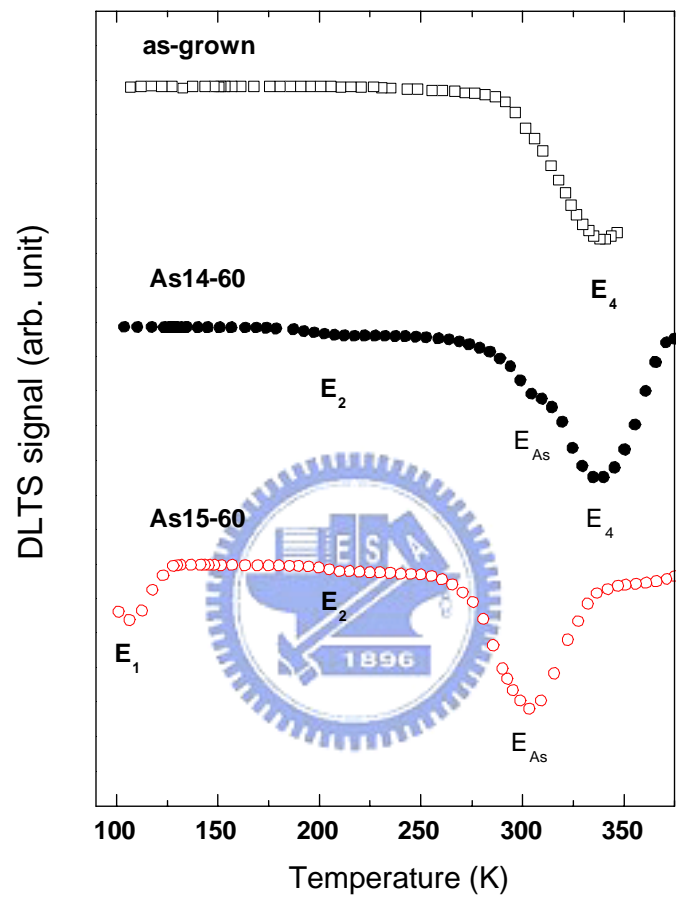


Figure 5.3: DLTS spectra of the as-grown, As14-60, and As15-60 samples.

	Dosage	Mobility	Concentration	Ideality	$J_S$	$\phi_{bn}$
Sample	( $\text{cm}^{-2}$ )	( $\text{cm}^2/\text{V}\cdot\text{s}$ )	( $\text{cm}^{-3}$ )	factor	( $\text{A}/\text{cm}^2$ )	(eV)
As grown		318	$2.14 \times 10^{17}$	1.387	$4.90 \times 10^{-7}$	0.744
As14	$1 \times 10^{14}$	275	$1.55 \times 10^{16}$	...	poor rectify	...
As14-60	$1 \times 10^{14}$	319	$1.74 \times 10^{17}$	1.227	$3.77 \times 10^{-10}$	0.927
As15	$5 \times 10^{15}$	16	$1.10 \times 10^{16}$	...	poor rectify	...
As15-60	$5 \times 10^{15}$	284	$9.76 \times 10^{16}$	1.293	$7.56 \times 10^{-10}$	0.909

Table 5.1: Parameters of Hall and current-voltage properties for as-grown, As14, As14-60, As15, and As15-60 samples.

comparison, that of as-grown sample is also included. The measurements were conducted at a biased of -1 V, pulsed periodically to 0 V for trap filling. Transient capacitance signals were acquired by using a test ac signal of 100 kHz and 100 meV over the temperature range from 370 K to 100 K. It is seen there is only one prominent deep level in the as-grown GaN, peaked at 340 K. Together with the Arrhenius plots in Fig. 5.4, we could determine the activation energy and the trap concentration of this 340 K point defect to be  $E_c-0.879$  eV (labeled as  $E_4$ ) and  $7.09 \times 10^{15} \text{ cm}^{-3}$ , respectively. Two additional deep levels,  $E_c-0.600$  eV (labeled as  $E_2$ ) and  $E_c-0.766$  eV (labeled as  $E_{As}$ ), showed up in the As14-60. On the other hand, for the As15-60,  $E_4$  deep level diminished almost completely, instead a shallower deep level  $E_c-0.157$  eV (labeled as  $E_1$ ) showed up. For convenience, all of the trap parameters for these samples are listed in Table 5.2.

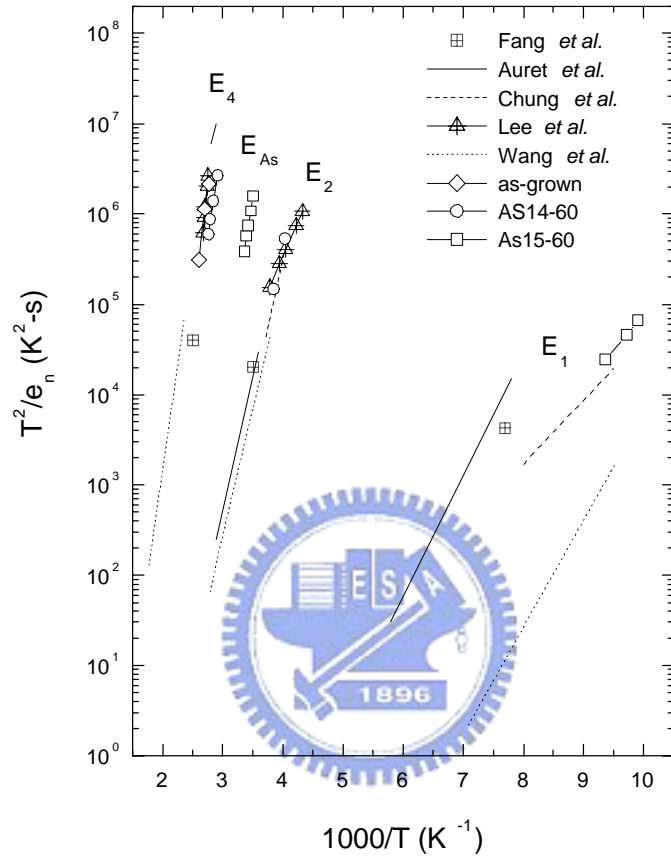


Figure 5.4: Arrhenius plot of DLTS signals for as-grown, As14-60, and As15-60 samples. Similar deep levels published in previous literatures are also included in this figure.

Sample	$\Delta E_1$	$N_1$	$\Delta E_2$	$N_2$
number	(eV)	( $\text{cm}^{-3}$ )	(eV)	( $\text{cm}^{-3}$ )
As-grown	—	—	—	—
As14-60	—	—	0.600	$2.77 \times 10^{14}$
As15-60	0.157	$1.03 \times 10^{15}$	0.600	$3.09 \times 10^{14}$

Sample	$\Delta E_3$	$N_3$	$\Delta E_4$	$N_4$
number	(eV)	( $\text{cm}^{-3}$ )	(eV)	( $\text{cm}^{-3}$ )
As-grown	—	—	0.879	$7.09 \times 10^{15}$
As14-60	0.766	$9.24 \times 10^{14}$	0.920	$5.92 \times 10^{15}$
As15-60	0.769	$7.37 \times 10^{15}$	—	—

Table 5.2: The parameters of DLTS signals for as-grown, As14-60, and As15-60 samples.

Although there are numbers of deep levels appeared in the diodes, the  $E_1$ ,  $E_2$  and  $E_4$  defects were observed in a variety of GaN samples grown by different methods, including metalorganic vapor phase epitaxy,[40, 48, 49, 50] hydride vapor phase epitaxy[51] and molecular beam epitaxy.[52] Accordingly,  $E_1$ ,  $E_2$  and  $E_4$  defects are commonly thought to be native defects and have been assigned to nitrogen vacancy related complex, nitrogen antisite and nitrogen interstitial, respectively. Since ion implantation is known to create native defects,[50] we attribute  $E_1$  and  $E_2$  traps found in our As-implanted films to this effect. On the other hand, the concentration of additional  $E_{As}$  level increase with the increasing arsenic doping suggests the formation of this deep level closely related to the arsenic ions. The tentative explanation for this particular trap is described as follows.



After As implantation, our GaN film is generally believed to hold large quantities of native defects, most likely in the form of nitrogen and gallium vacancies, and arsenic interstitials. Owing to their unstable nature, these arsenic interstitials have a great tendency to incorporate either on Ga to form isovalent arsenic substitutes ( $As_N$ ) or on N sites to form arsenic antisite ( $As_{Ga}$ ) during the subsequent thermal annealing process. Calculation showed both of these levels are type of donor defects with energies positioning at 0.11-0.33 eV above the valence band and 2.6-2.7 eV above the valence band for  $As_N$  and  $As_{Ga}$ ,[41, 42] respectively. The  $As_N$  level therefore is too deep to be account for the observed data

and lead us to believe  $E_{As}$  deep level is the arsenic antisite defect. This is supported by the summation of 0.766 eV and 2.6-2.7 eV equals approximately to 3.4 eV, GaN bandgap[53], and by the much low formation energy of arsenic antisite than that of the isovalent arsenic substitute (-0.37 eV vs. 4.2 eV).[42] More interestingly, our DLTS results agreed to PL data in As-doped GaN films reported to date.[43, 44, 45, 46] In these literatures, a strong, broad blue emission with energy approximately 2.6-2.73 eV[43, 44, 45, 46] was found in As-doped GaN films, irrespective of ion-implanted or epitaxial samples. The schematic diagram of the related transitions is shown in Fig. 5.5.

#### 5.4 Summary

In summary, we have performed the DLTS study on the arsenic implanted GaN films. After 60 minutes annealing at 800°C, we have found a deep level lays  $\sim 0.766$  eV below the conduction band of the As-implanted GaN samples. We tentatively assign this trap to be arsenic antisite since its energy coincides well with the result predicted by theoretical calculation. Our DLTS results also agreed the data from PL measurements fairly well. This finding suggests that arsenic ions in GaN induce deep levels that perform active in both electrical and optical transition processes.

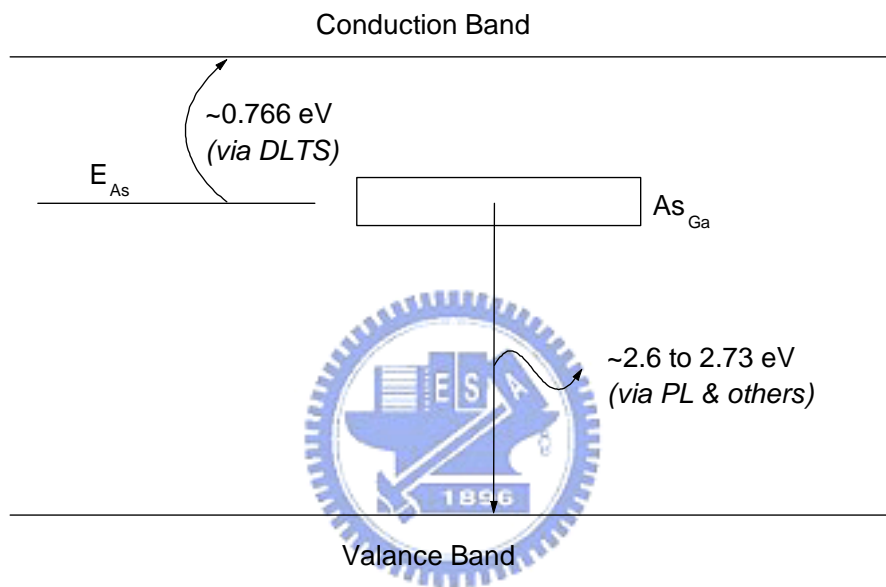


Figure 5.5: The schematic diagram on the energy level of As substitute on Ga site, and its related transitions measured by DLTS and PL measurements.



## CHAPTER 6

# MICROSTRUCTURAL STUDY OF THERMAL ANNEALING EFFECTS ON MG DOPED GAN FILMS

### 6.1 Introduction

GaN and other group III nitrides have invited considerable interest because of their successful applications in high power, high temperature, and light producing (visible and UV) opto-electronic devices.[54, 55, 56] To meet the criterion of device quality, thermal processing for the activation of *p*-type dopant (commonly prepared with magnesium) becomes a critical step. Though some work has been devoted to the effects of thermal annealing on electrical and optical properties,[57, 58, 59] the study of effects on microscopic crystal properties are limited. In this letter, we examined these properties on 30 min and 1 hour 700°C thermal annealed samples using *x*-ray absorption fine structure (XAFS) measurements. Analysis of the obtained data showed thermal annealing resulted in more ordered atomic arrangement and richer concentration of the stable polytype in films.

## 6.2 Experiments

Undoped and Mg-doped GaN samples (with thickness  $\sim 1 \mu\text{m}$ ) used in the experiment were grown on (0001) sapphire substrate at  $1075^\circ\text{C}$  by metalorganic vapor phase epitaxy (MOVPE) in the atmospheric pressure. Trimethylgallium (TMGa) and ammonia ( $\text{NH}_3$ ) and were used as the Ga and N precursors with flow rates of  $10.4 \mu\text{mol}/\text{min}$  and  $0.7 \text{slm}$ , respectively. The carrier gas was purified nitrogen. For doped GaN growth, we introduced a flow of biscyclopentadienyl-magnesium ( $\text{Cp}_2\text{Mg}$ ) from  $0.02$  to  $0.79 \mu\text{mol}/\text{min}$  into the quartz reactor. The Mg solid concentrations of all samples were estimated to be from  $1.7 \times 10^{16}$  to  $2.0 \times 10^{20} \text{cm}^{-3}$ , as determined by secondary ion mass spectrometry measurements.6.1

Ga *K*-edge XAFS measurements were performed in the energy ranging from  $10.2$  to  $11.3 \text{keV}$  at the wiggler beamline BL17C in the Synchrotron Radiation Research Center of Taiwan. A Si(111) double-crystal monochromator with a  $0.5 \text{mm}$  entrance slit was used. The intensity of the incident *x*-ray was monitored by an ionization chamber filled with nitrogen gas, and the fluorescence emitted from the samples was detected by an argon-filled Stern-Heald-Lytle detector. A Zn filter was placed between the samples and the detector window to eliminate the noise from scattering and to improve the spectrum quality.

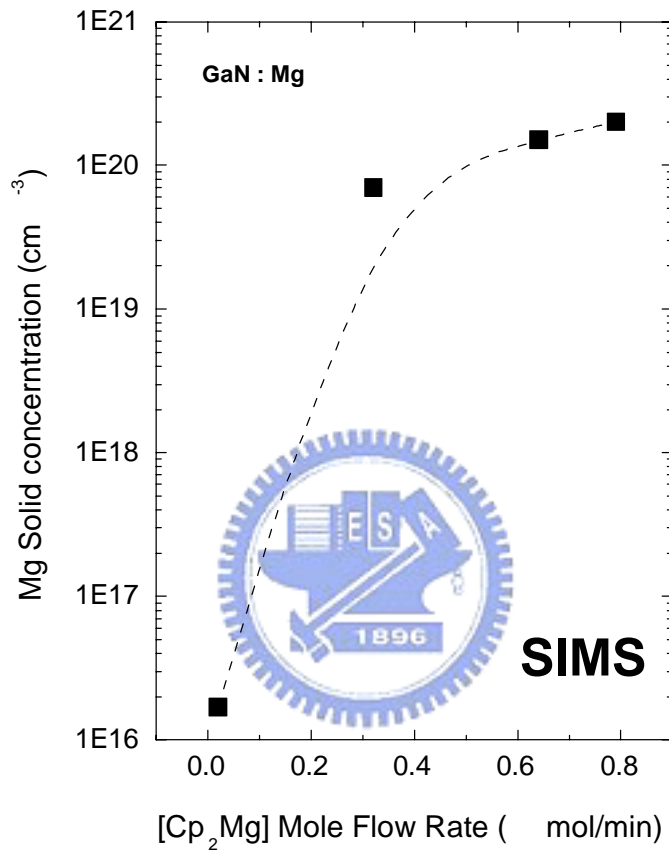


Figure 6.1: SIMS results of Mg doped GaN with various  $Cp_2Mg$  flow rates.

### 6.3 Results and Discussion

Figures 6.2(a) and 6.2(b) show the Ga  $K$ -edge  $x$ -ray absorption near-edge structure (XANES) spectra for GaN samples in the normal (electric-field vector  $E \parallel c$  axis) and the grazing ( $E \perp c$  axis) incidence angles, respectively. These samples examined are amorphous ( $a$ -), heavily Mg doped ( $x$ -) GaN ( $C_{p_2Mg}=0.79 \mu\text{mol}/\text{min}$ ,  $[Mg]=2.0 \times 10^{20} \text{ cm}^{-3}$ ) thermal annealed at  $700^\circ\text{C}$  in  $\text{N}_2$  environment for 0, 30 and 60 min and undoped ( $u$ -) GaN. The annealing temperature was intentionally chosen for the typical activation condition of  $p$ -type GaN using Mg as a  $p$ -type dopant.[60] The first reference sample,  $a$ -GaN, results in both Figs. 6.2(a) and 6.2(b) shows independence of polarization effects due to their amorphous characteristic. On the contrary, the heavily Mg-doped GaN,  $x$ -GaN, and the second reference sample,  $u$ -GaN, exhibit strong polarization effects. Similar polarization variations on group III  $K$ -edge XANES were also observed for InN and AlN.[61] This is attribute to the anisotropic distribution of the  $p$ -partial density of state ( $p$ -DOS) in the conduction band along the hexagonal  $c$ -axis and its perpendiculars.

In Figs. 6.2(a) and 6.2(b), the XANES intensity interference oscillations of  $x$ -GaN are seen to intensify with the increasing annealing duration, suggesting an electron density increasing of the conduction band. This tendency is consistent with photoluminescence results of an earlier report, [59] where the intensity of the blue-band emission increases after proper thermal annealing. However, we see

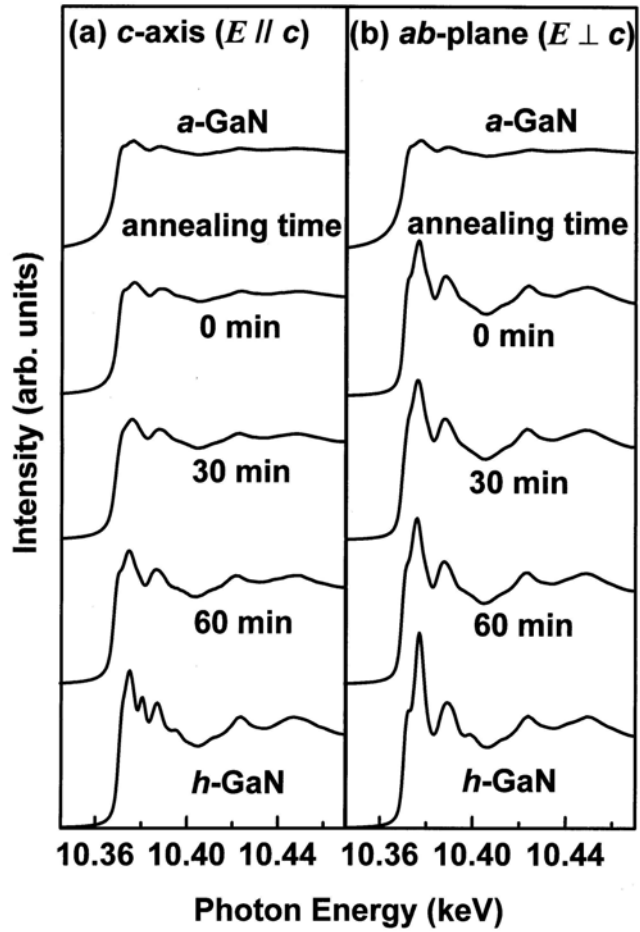


Figure 6.2: Ga *K*-edge XANES spectra of amorphous, heavily Mg-doped, and undoped GaN films in (a) *c* axis ( $E \parallel c$ ) and (b) *ab* plane ( $E \perp c$  axis) polarization mode.

the increase is much more pronounced in the  $E \parallel c$  axis case than in the  $E \perp c$  axis case, revealing the influence of thermal annealing on the  $p$ -DOS along  $c$  axis direction is more enhanced than that in the  $ab$  plane.

It is interesting to note that, in Figs. 6.2(a) and 6.2(b), the  $x$ -GaN's XANES spectra evolve towards  $u$ -GaN's with the increasing of annealing durations. This polarization-dependence evolution through thermal annealing is related to the decreasing of disorderliness and the transformation towards a more anisotropic crystal structure, *i.e.* wurzite structure, which we will explain in the Extend XAFS simulations later.

Extend XAFS (EXAFS) analysis of the samples were carried out using the FEFF8 program package. The resulting Fourier transform (FT) amplitudes of  $k^3\chi(k)$  versus radial distance  $R$  for the case of  $E \parallel c$  axis and  $E \perp c$  axis for the heavily Mg doped GaN ( $x$ -GaN) are shown in Figs. 6.3(a) and 6.3(b), respectively. Again, more significant FT amplitude intensification with annealing time is seen in the  $E \parallel c$  axis case. Using the FEFFIT program, the results extracted from Fig. 6.3(a) are listed in Table 6.1. The first two shells' coordination numbers,  $N_{Ga-N}$  and  $N_{Ga-Ga}$ , were increased from 0.347 to 0.580 and from 1.830 to 3.020, respectively, after the thermal treatment. The corresponding Debye-Waller factor of the two shells,  $\sigma_{Ga-N}$  and  $\sigma_{Ga-Ga}$  were reduced from 4.25 to 2.68 and from 7.43 to 4.66 ( $\text{\AA}^2 \cdot 10^{-3}$ ). Debye-Waller factor, the mean square fluctuation in interatomic distance between the  $x$ -ray absorbing atom and the neighboring atoms, includes

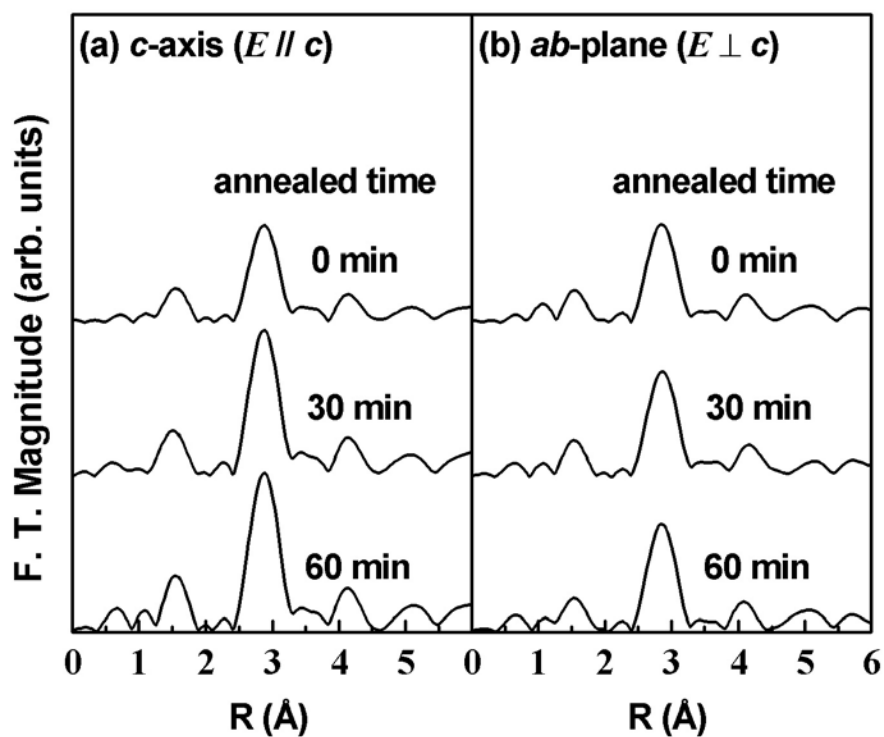


Figure 6.3: Fourier transform (FT) amplitudes of Ga  $K$ -edge EXAFS for heavily Mg-doped GaN annealing after 0, 30, and 60 min in (a)  $c$  axis ( $E \parallel c$ ) and (b)  $ab$  plane ( $E \perp c$  axis) polarization mode.

TA time (min)	$N_{Ga-N}$	$N_{Ga-Ga}$	$\sigma_{Ga-N}$ ( $\text{\AA}^2 \cdot 10^{-3}$ )	$\sigma_{Ga-Ga}$ ( $\text{\AA}^2 \cdot 10^{-3}$ )	$R_{Ga-N}$ ( $\text{\AA}$ )	$R_{Ga-Ga}$ ( $\text{\AA}$ )
0	0.347	1.830	4.253	7.433	1.943	3.188
30	0.465	2.425	3.472	6.054	1.945	3.192
60	0.580	3.020	2.681	4.664	1.946	3.195

Table 6.1: EXAFS-analysis results of *x*-GaN through 60 min thermal annealing (TA).

essentially a temperature-dependent part resulting from thermal vibration and a temperature-independent part arising from the structural disorder[62]. Since the EXAFS measurements were all performed at room temperature, the decreasing of Debye-Waller through 1 hour thermal annealing for GaN:Mg films in the  $E \parallel c$  axis was ascribed to the reduction of structural disorder in the  $E \parallel c$  axis. The first two shells' distances,  $R_{Ga-N}$  and  $R_{Ga-Ga}$ , were respectively increased from 1.943  $\text{\AA}$  to 1.946  $\text{\AA}$  and from 3.188  $\text{\AA}$  to 3.195  $\text{\AA}$  through the two step thermal annealing. Increasing of the first two shell's distances is also related to the decreasing of structure disorderliness[63].

To understand the possible reasons for the evolution of *p*-DOS, the increasing of the observed FT amplitudes, coordination numbers and distances of the first two shells through 1 hour thermal treatment in the  $E \parallel c$  case, we took one step back to the comparison of  $k^3\chi(k)$  from the EXAFS measurements and the simulated curve of our models. In these *k*-power multiplied interference functions of  $\chi(k)$ , it



is easy to see the envelope and frequency of the encompassed sinusoidal wave. We first compared our *u*-GaN  $k^3$ -multiplied data from AUTOBK and the  $k^3\chi(k)$  of the generated hexagonal GaN results in Fig. 6.4(a). AUTOBK is a background removal inclusion of FEFF8. We can simulate a number of cases such as vacancies ( $V_{Ga}$  and/or  $V_N$ ), substitutionals ( $Mg_{Ga}$ ), interstitial occupations ( $Mg_i$ ), as well as their combinations by alternating the output of ATOMS in FEFF8 which provides a coordination list of atoms (relative to the absorber Ga atom at the origin) in a given crystal lattice. Additionally, since the cubic and hexagonal GaN structures crystallographically differ only in an altered stacking sequence of identical close-packed atomic planes, we know that the cubic structure would be induced by Mg incorporation to form mix-phase GaN. Meanwhile, because of the thermal energy supply during thermal annealing, the variation of structural mixing-phase is expected because the difference in formation energy for both stacking sequences is only about 10 meV/atom[64]. Therefore, all cases of 1  $V_{Ga}$ , 1  $V_N$ , 1  $Mg_{Ga}$ , 1  $Mg_i$ , 2  $Mg_{Ga}$ , 2  $Mg_i$ , and 1  $Mg_{Ga}$  + 1  $Mg_{Ga}$  for the hexagonal and cubic GaN using proper weighting were used to simulate the *x*-GaN's data through thermal annealing, and comparable results with smaller phase shifts could only be provided by one substitutional and one interstitial Mg case. However, phase shifting and the theoretical oscillatory amplitude needs further adjustments. To do this, impurity incorporation and vacancy defects larger than those cases were not attempted, since it was impractical because of the Mg concentration and the well-preserved crystalline

form based on our Raman data.[65] On the other hand, one may consider the variation of disorderliness through thermal annealing resulting from the presence of impurity related defects and the variation of mix-phase structure in the film. The disorder in crystal would affect the lattice Debye temperature ( $T_D$ ) resulting in the adjustment of phase shifts and oscillatory amplitudes.[63] Better fittings were finally obtained after we included all these considerations, and they were shown in Figs. 6.4(b) to 6.4(d), where we had used cubic  $Mg_i$  at (1.8435, 1.8435, and 1.8435 Å) and hexagonal  $Mg_i$  at (-0.9208, -2.7545, and 1.2900 Å) with  $Mg_{Ga}$  for both crystals, with proper Debye temperatures and structural phase-mixing ratios. The mixing of hexagonal and cubic phases in GaN:Mg films and the role of Mg atoms were accounted for in the data analysis and curve fitting using FEFF8 software package developed by the University of Washington (Seattle, USA). From our best fitting results we can to examine the variation in phase mixing and Debye temperature change due to different annealing time. Those results are shown in Figs. 6.5 and 6.6.

Fig. 6.5 represents the weighting of hexagonal structures for as-grown, 30 min, and 60 min annealed GaN:Mg films. As can be seen in Fig. 6.5, the hexagonal phase fraction at each annealing time retains its decreasing behavior with the increasing  $Cp_2Mg$  flow rates. This results from the cubic-phase augmentation introduced by the incorporation of Mg atoms.[63] Notably, we see the weighting of hexagonal structures for each  $Cp_2Mg$  flow rate increased with the annealing

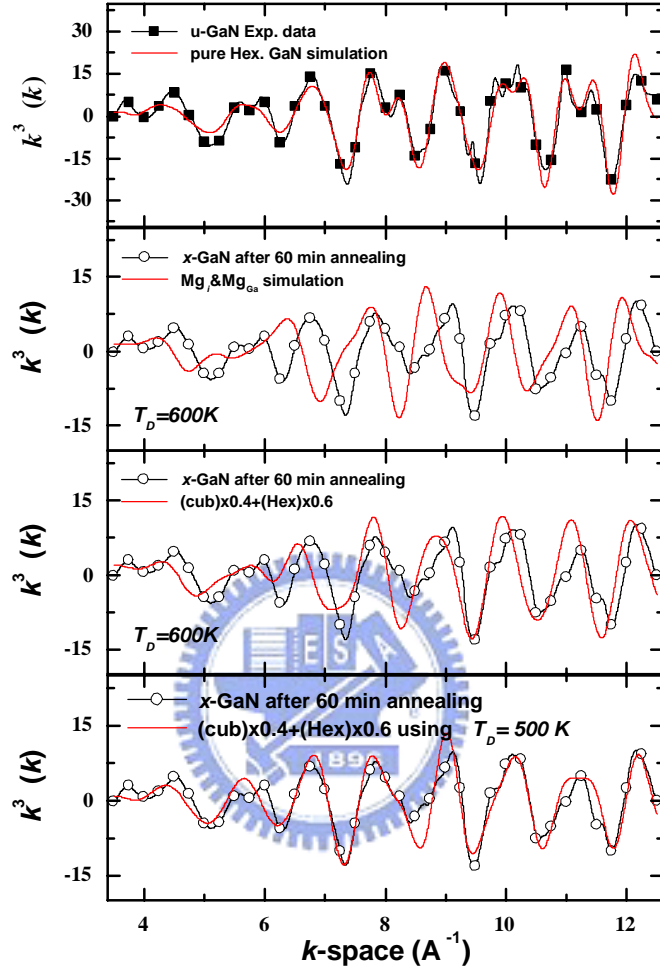


Figure 6.4: Comparisons of  $k^3\chi(k)$  oscillations for the  $E \parallel c$  axis polarization of (a) our  $u$ -GaN and the FEFF8-generated undoped hexagonal GaN, (b) 1 hour annealed  $x$ -GaN and the simulated case of  $1\text{Mg}_i+1\text{Mg}_{Ga}$ , (c) 1 hour annealed  $x$ -GaN and the simulated of mixed-phase  $1\text{Mg}_i+1\text{Mg}_{Ga}$ , (d) the case of (c) using reduced  $T_D = 500\text{K}$ , showing the best fit of our data.

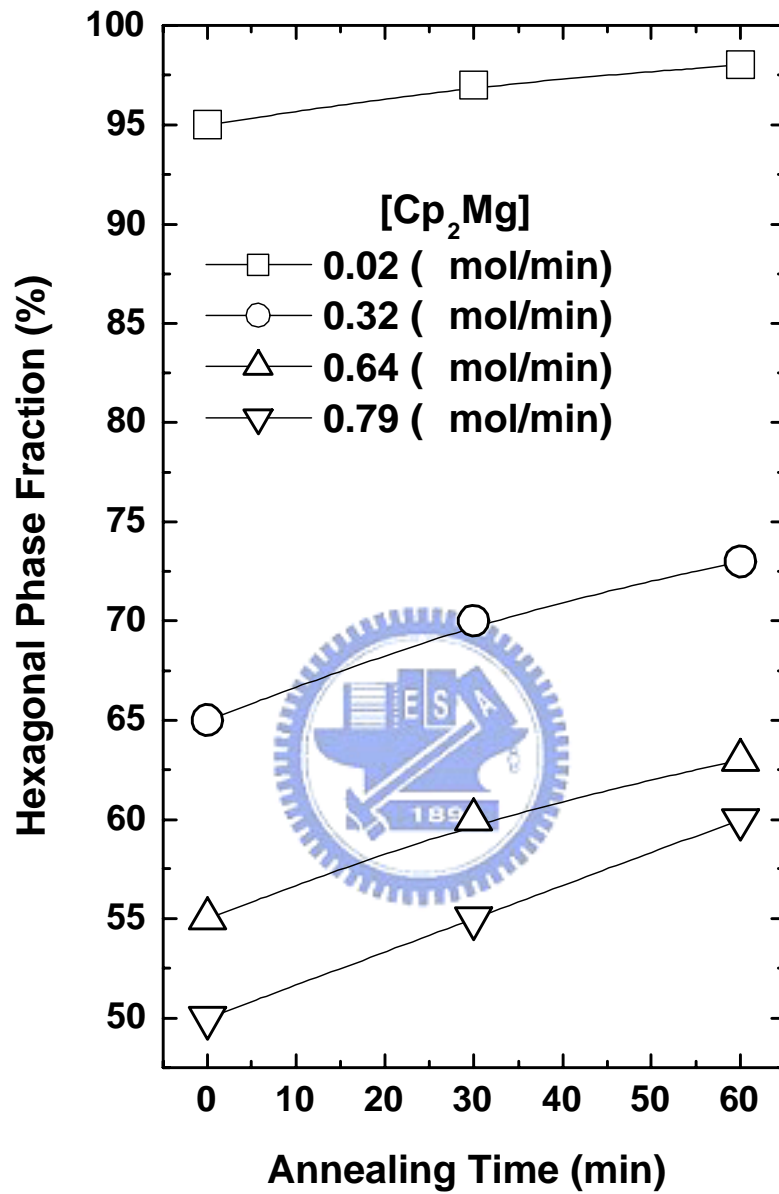


Figure 6.5: Hexagonal phase fractions for as-grown, 30 min, and 60 min annealed GaN:Mg films.

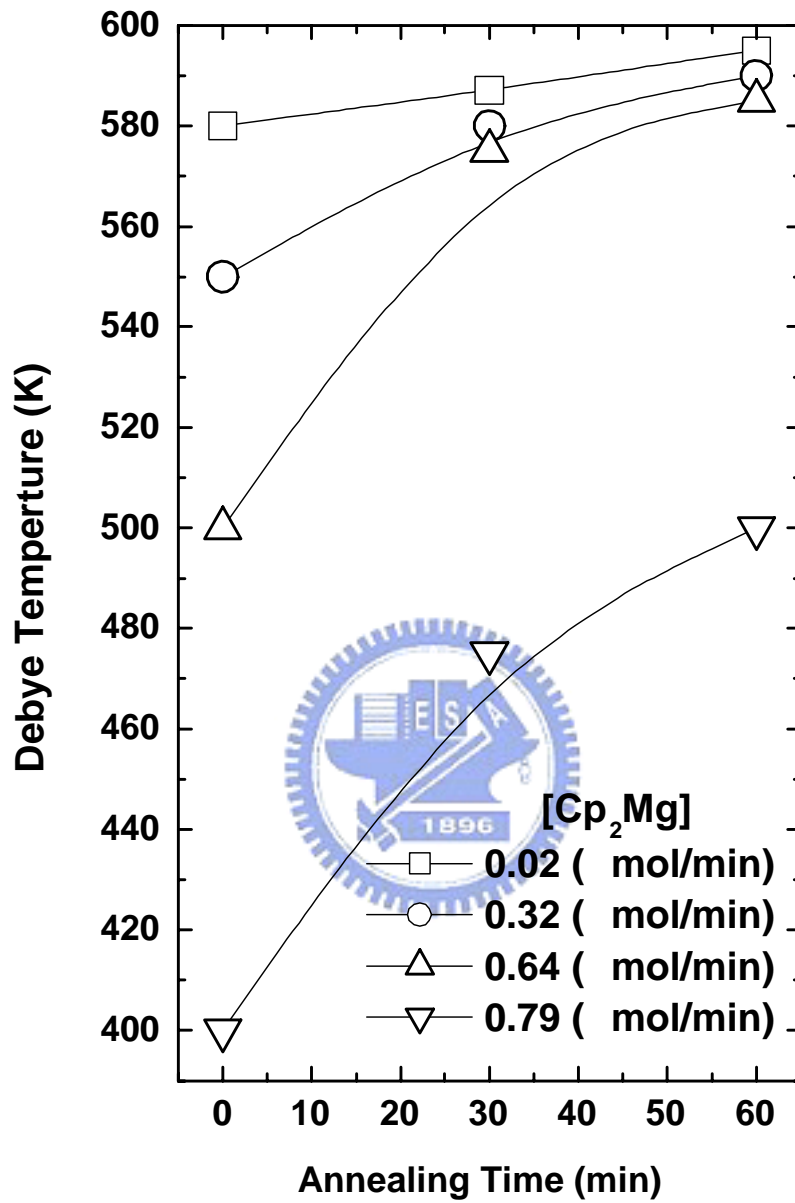


Figure 6.6: Debye Temperatures for as-grown, 30 min, and 60 min annealed GaN:Mg films.

time. The reduction of the cubic phase and enhancement of the hexagonal phase show the latter structure is more stable form that gained more percentage during the course of annealing. The trend of hexagonal enhancement was also displayed in the XANES spectra of Fig. 6.2 (since *u*-GaN is hexagonal[63]) and reflected in the lengthening of inter-atomic bond lengths in the direction normal to the epifilms' surface (because of the larger lattice constant of hexagonal GaN than that of cubic GaN), diminishing of Debye-Waller factor as well as the shifting of coordinates numbers towards a more stable configuration.

The Debye temperatures for as-grown, 30 min, and 60 min annealed GaN:Mg samples are depicted in Fig. 6.6. At each annealing time, the Debye temperature ( $T_D$ ) keeps decreasing with the Mg supply. This is caused by the disorderliness introduced by Mg incorporation.[63] It is noted in Fig. 6.6, that  $T_D$  increases with the annealing time for each  $\text{Cp}_2\text{Mg}$  flow rate. From the Debye approximation for the Debye-Waller factor of EXAFS, Sevillano[66] suggested that increasing of Debye temperature would appear with the reduction of Debye-Waller factor. This is in accordance with our EXAFS analysis that  $\sigma_{\text{Ga}-\text{N}}$  and  $\sigma_{\text{Ga}-\text{Ga}}$  were both reduced after thermal annealing. The increasing of  $T_D$  through thermal annealing can be viewed as the combined effects of structure disorder reduction and density of states increasing with the evolution of mix-phase structures towards hexagonal phase through thermal annealing.

## 6.4 Summary

Thermal annealing effects on GaN:Mg films grown by MOVPE were investigated with *x*-ray absorption spectra. From the near edge spectral data, mixed polytype structural shifting was seen to favor the hexagonal wurzite structure through annealing. From EXAFS analysis and data simulation, on the other hand, stronger effects on the structural parameters pertinent to the *x*-ray addressed elements were found to occur on the hexagonal *c*-axis direction and an overall Debye temperature increasing for the films was also inferred. Based on these findings we concluded that a more stable and orderly atomic configuration was achieved in the longer annealing samples and crystalline property characterization using *x*-ray absorption measurements is effective and feasible for studying compound semiconductors of this breed.



## CHAPTER 7

# LONG-TERM PHOTOCAPACITANCE DECAY BEHAVIOR IN UNDOPED GAN FILMS

### 7.1 Introduction

Because of its superior material properties including a wide direct band gap, high breakdown electric field, and high thermal conductivity as well as high thermal stability, gallium nitride (GaN) has recently drawn much attention from the view point of use in a variety of device applications. These include high-temperature transistors[67], blue and green light-emitting diodes and violet laser diodes[68]. However, as compared to GaAs and InP, GaN usually possesses relatively poor film quality in terms of dislocations. With such a high density of threading edge dislocations[69] ( $10^8 \text{ cm}^{-2}$ ), it was difficult to believe that high-performance optoelectronic devices can be realized without difficulty by the use of this type of material. In the early stages of GaN device fabrication, researchers even believed that the dislocations were simply electrically inert to a light-emitting process. Nevertheless, Rosner *et al.*[70] have shown in their cathodoluminescence study that dislocations influence carrier recombination and, most likely, act as nonradiative recombination centers in GaN. It was also demonstrated that nega-



tive charges exist near the edge dislocations, displaying acceptorlike behavior[71]. All of these arguments were recently supported by the models developed by Look and Sizelove[72], Wright and Grossner[73], and Elsner *et al.*[74] Their works showed that the threading edge dislocations in GaN are indeed electrically active, affecting not only the minority carrier transport parameters but also the luminescence efficiency. In this chapter, we provide a different means of examining the physical properties of GaN film by observing for the first time the long-term photocapacitance decay behavior in undoped GaN. Our results show that the steady state value of the transient photocapacitance decays logarithmically in time defined by the time interval between light off and the commencement of measurement at room temperature. This dynamic response is inferred to be correlated closely to the electron-hole recombination at dislocations.



## 7.2 Experiments

The sample employed in this study is undoped GaN grown on a (0001) sapphire substrate using the low-pressure metalorganic vapor phase epitaxy (MOVPE) growth technique. The corresponding Hall concentration and mobility are  $4.7 \times 10^{16} \text{ cm}^{-3}$  and  $77 \text{ cm}^2/\text{V}\cdot\text{s}$ , respectively. During the experiment, metal Ni dots of 1 mm diameter were first deposited on the film as Schottky contacts through a metal mask by electron-gun evaporation. The ohmic contact was subsequently formed on the epilayer surface by depositing strips of Al, which exhibited good linear I-V

characteristic and was suitable for our phot capacitance measurements.

### 7.3 Design of Photocapacitance Measurements

For the measurements of photocapacitance, the Schottky diode was illuminated by a nominal 60 W tungsten lamp for 5 min at zero bias voltage. The sample was then used for the measurement of transient behavior at room temperature using a HP4194 impedance analyzer at different dark waiting times from 5 min to 12 h. For each measurement, a reverse bias of -1 V square voltage with duration of  $\sim 1.5$  s was applied for the purpose of emptying the carrier in the depletion region. Pulses with a test frequency of 10 kHz and 100 mV oscillation level were employed to record the small signal diode capacitance. The trigger duration used was sufficiently long to attain the respective steady state capacitance value,  $C_S(t)$ , so that long-term photocapacitance behavior could be obtained. Attention was paid to ensure that the time interval between the consecutive measurements was at least 4 min. Under these circumstances, any possible intervention between the measurements can be minimized to a negligible extent. The schematic procedures of the experiment was shown in Fig. 7.1.

### 7.4 Results and Discussion

Figures 7.2(a) and 7.2(b) show the transient capacitance of the undoped GaN measured at room temperature probed at different waiting times,  $t$ , after the il-

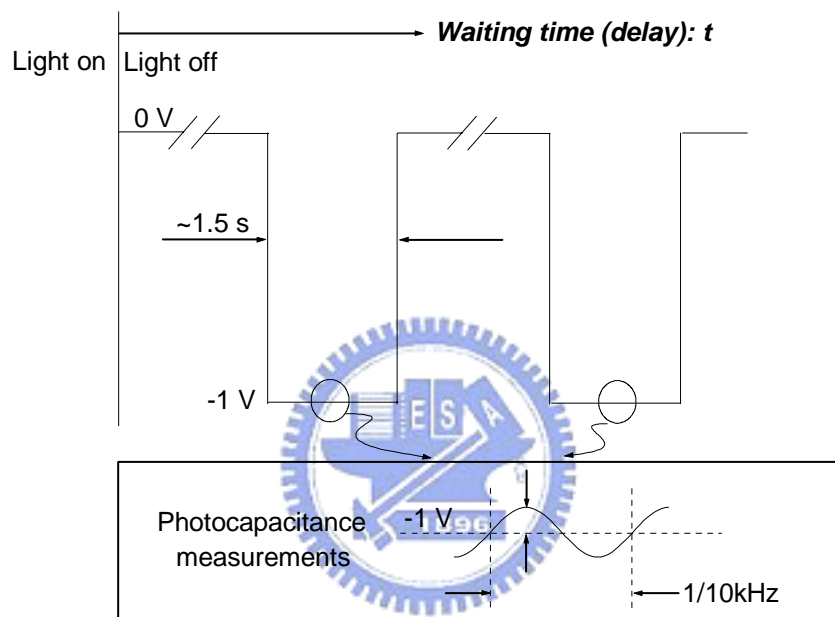


Figure 7.1: Schematic procedures of photocapacitance measurements.

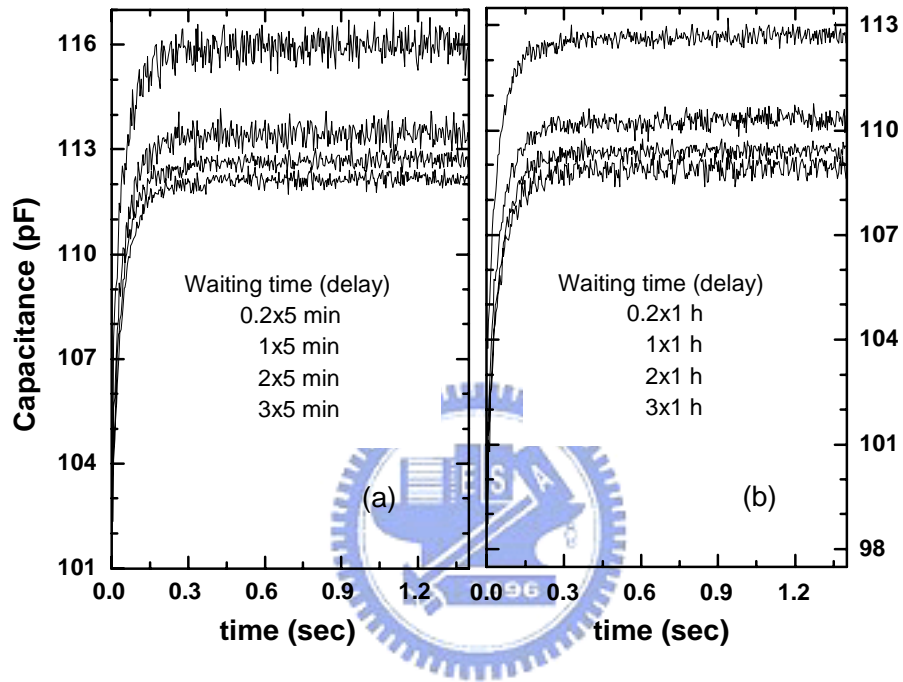


Figure 7.2: The transient capacitance response of the undoped GaN during the applications of square voltage recorded at different waiting time,  $t$ , at room temperature.

lumination was switched off. As can be seen in Figs. 7.2(a) and 7.2(b), for each measurement when a square triggering voltage is applied, the capacitance signal increases exponentially at the beginning and saturates to a steady-state value within a duration of  $\sim 0.2$  s. The uprising portion has been attributed primarily to the point defects associated with the 0.60 eV level below the conduction band as they exhibit the characteristics of the same time constant and defect concentration, as revealed by deep level transient spectroscopy measurements[75]. This particular trap, due to its fast dynamic response in nature, cannot be considered responsible for the long-term photocapacitance behavior. It is worth noting that the steady-state capacitances  $C_S(t)$  in Figs. 7.2(a) and 7.2(b) were recorded respectively in 5 min and 1 h units and also plotted in shifted ordinates. The heights of  $C_S(t)$  on both sides of the figures, due to their logarithmic nature, are virtually the same for all different time scales used. That is, the heights of  $C_S(t)$  are the same for  $t = 0.2 \times 5$  min,  $t = 0.2 \times 1$  h, and so forth.

Figure 7.3 depicts the plot of steady-state values of the photocapacitance,  $C_S(t)$ , versus  $t$ .  $C_S(t)$  is found to decrease logarithmically as a function of  $t$  with its value dropping from 113 pF at  $t = 5$  min to 107 pF at  $t = 12$  h. The change in  $C_S(t)$  can be expressed approximately as:

$$\Delta C_S(t) \propto -\log(t). \quad (7.1)$$

Similar phenomenon in photoconductivity behavior was observed in the plasti-

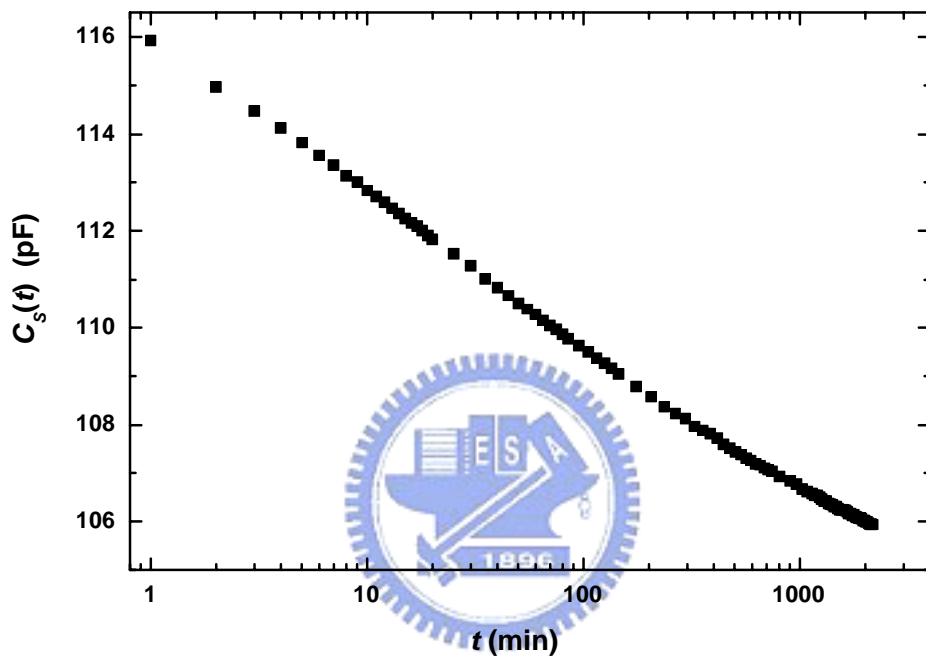


Figure 7.3: The steady state value of transient capacitance,  $C_S(t)$  versus waiting time  $t$  at room temperature for undoped GaN.

cally deformed n-type GaAs reported by Nakata and Ninomiya[76]. They ascribe this unique feature to the carrier recombination involved with the dislocations presented in the epilayer. We believe this is also the very case which occurred in our heteroepitaxial GaN film.

It is known that due to the lack of a lattice-matched substrate, the GaN epitaxial film usually contains large quantities ( $> 10^8 \text{ cm}^{-2}$ ) of threading edge dislocations[69]. By using scanning capacitance microscopy, Hansen *et al.*[71] found that in the vicinity of dislocations, the electronic structure appears to be negatively charged, which is very different from the rest of the region. They attributed this to the presence of deep acceptor-like trap states near the valence band associated with threading dislocations. This view was soon supported by Wright and Grossner[73] and Elsner *et al.*[74] using density-functional theory to study the effects of doping and growth stoichiometry on the core structure of threading dislocations for GaN. Their calculations showed that the edge dislocations indeed play an essential role as electron traps, *i.e.*, acceptor-like defects, in an n-type GaN material. The foregoing arguments certainly provided us with valuable hints towards the explanation of our observed data.

In this experiment, the GaN sample was subjected to light illumination at the beginning, generating a substantial number of excess holes in the valence band as shown in Fig. 7.4(a). Owing to the characteristic of the short minority carrier lifetime ( $\sim 6.5 \text{ ns}$ ) in n-GaN[77], the excited holes soon migrate to the dislocations.

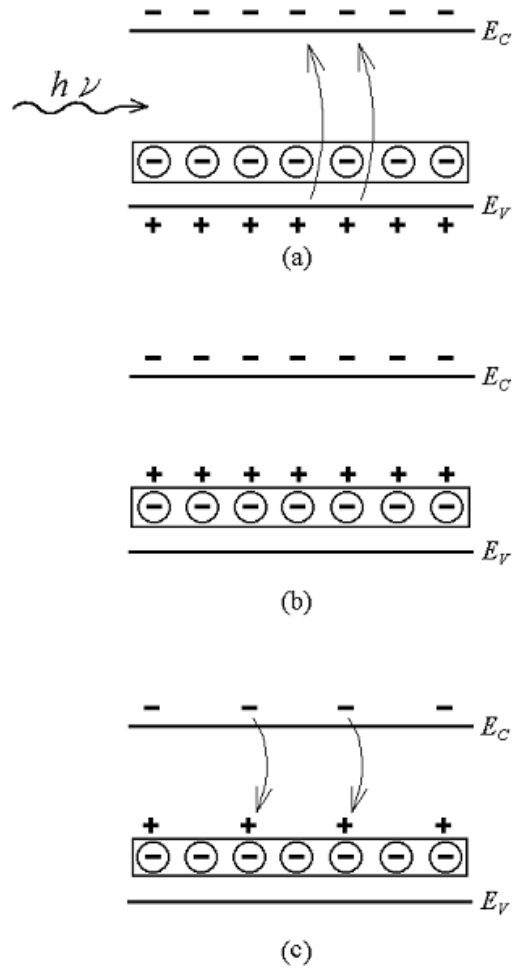


Figure 7.4: The status of excess carriers in GaN (a) during the photopumping (b) at the time soon after the photopumping, and (c) at prolonged time after the switch-off of the light. The open rectangles enclosing negative charged ions symbolizes the groups of linear arranged dislocation traps.



At the end of photopumping, most traps along the dislocation lines are conceivably filled with holes and become neutrally charged (Fig. 7.4(b)). When the light is switched off, the trapped holes remain at the dislocations until recombination with electrons from the conduction band (Fig. 7.4(c)). It is worth mentioning that the capture of electrons by dislocations discussed here proceeds relatively slowly compared to the capture of holes in the valence band. This is because these dislocation traps in principle act as repulsive Coulomb scattering centers for nearby electrons. Unlike the filling of holes, a cylindrical potential barrier[72] is presented between the free electrons and dislocation lines due to the nature of the negative charge property of the core dislocation.

The description of the electron captured by dislocations using the barrier-limited recombination model was given by Figielski[78]. In this model, the electron capture rate for linearly arranged traps, such as dislocation lines, is assumed to be limited by the barrier height of the corresponding cylindrical potential, set up by the electrons already caught by the dislocations. The electrostatic potential at time  $t$  established in the depletion region due to the uniform trap concentration can be written as:

$$\phi(t) = \frac{\phi_0 n_T(t)}{n_{T0}}, \quad (7.2)$$

where  $n_T(t)$  is the concentration of traps actually occupied with electrons and the subscript "0" denotes their final steady state values under the experimental con-

dition. The height of the barrier increases gradually with the increasing number of trapped electrons, making the subsequent capture of electrons in the conduction band more difficult. Consequently, a prolonged charge transfer phenomenon resulted in the diode.

Since only those free electrons having sufficient energy to surmount the potential barrier can reach the trap site and recombine with holes, the rate equation for this electron capture process, therefore, can be written as:

$$\frac{dn_T}{dt} = \sigma_T \nu_n (N_T - n_T) n \exp \frac{-q\phi(t)}{kT}, \quad (7.3)$$

where  $\nu_n$  is the thermal velocity of the electrons,  $\sigma_T$  and  $N_T$  are respectively the electron capture cross section and the total concentration of the dislocation traps,  $n$  represents the free electron concentration outside the barrier, and

$$n \exp \left[ \frac{-q\phi(t)}{kT} \right] \quad (7.4)$$

is the amount of free electrons that can leap over the barrier. For simplicity, the concentration of the dislocation traps  $N_T$  is assumed to distribute uniformly throughout the semiconductor. With the initial condition  $n_T(0) = 0$  and the assumption of a slow electron filling process associated with the dislocation traps, *i.e.*,  $n_T(t) \ll N_T$ , one can arrive at an approximate solution to eq.(7.3) in the form of:

$$n_T(t) = \frac{kT}{q} \frac{n_{T0}}{\phi_0} \ln \frac{t + t_0}{t_0}, \quad (7.5)$$

where

$$t_0 = \frac{kT}{q} \frac{n_{T0}}{\sigma_T \nu_n n \phi_0 N_T}. \quad (7.6)$$

For  $t \gg t_0$  and after substituting eq.(7.6), eq.(7.5) can be expressed as a linear equation in a linear form of:

$$n_T(t) = a + b \ln t, \quad (7.7)$$

where

$$a = -\sigma_T \nu_n n N_T t_0 \ln t_0 \quad (7.8)$$

and

$$b = \sigma_T \nu_n n N_T t_0. \quad (7.9)$$

We propose the photocapacitance  $C_S(t)$  is related to the charge state affiliated with the dislocation traps and can be expressed as[79]:

$$C_S(t) = C_S(0) \sqrt{1 - \frac{n_T(t)}{N_D}} \approx C_S(0) \left[ 1 - \frac{n_T(t)}{2N_D} \right] \quad (7.10)$$

for  $n_T(t) \ll N_D$ , where  $N_D$  is the donor density in the space charge region. Hence from eq.(7.10) and the  $C_S(t)$  versus  $t$  curve in Fig. 7.3, we then obtained  $n_T(t)$  of each  $t$  and plotted it in Fig. 7.5. From the ratio of the retrieved slope and intercept of  $n_T(t) = a + b \ln t$ , we obtained the time constant  $t_0$  of  $\sim 34.5$  s. Since we know that  $N_T/N_D$  has a lower limit of  $\sim 20\%$  from Fig. 7.5, together with the obtained time constant  $t_0$ , slope  $b$ , and  $n = 4.7 \times 10^{16} \text{ cm}^{-3}$ , we obtained an upper limit of capture cross section of  $\sigma_T \approx 2.89 \times 10^{-27} \text{ cm}^2$ . For comparison,

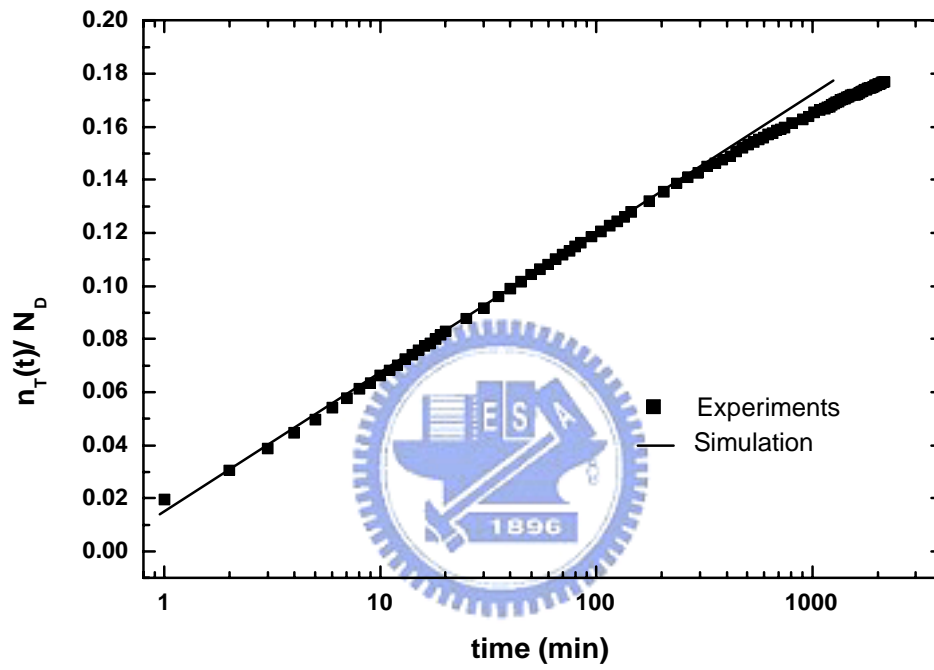


Figure 7.5: The ratio of  $n_T(t)$  and  $N_D$  versus waiting time  $t$  at room temperature.

a straight line using the same time constant and the same upper limit value of the capture cross section is also plotted in Fig. 7.5 to simulate the conditions of  $t \gg t_0$ .

From Fig. 7.3 and Fig. 7.5, it is evident that our measured photocapacitance and trap concentration essentially follow the theoretical prediction when the waiting time  $t$  (delay) is longer than 3 min, satisfying the condition of  $t \gg t_0$ . The capture cross section  $\sigma_T$  obtained is much smaller than the physical size of a hydrogen atom ( $\sim 10^{-15}$  cm<sup>2</sup>). This is consistent with our earlier repulsive Coulomb potential assumption. Nonetheless, departure of the experimental data from the simulated line is observed for  $t > 500$  min. After such a long waiting time  $t$ , the trapped electron concentration  $n_T(t)$  tends to approach its final saturation value  $n_{T0}$ . Under this circumstance, the linear dependence of cylindrical potential on the concentration of the trapped electron is no longer valid and the electron capture process slows down markedly and eventually ceases.

## 7.5 Summary

In summary, the dynamic photocapacitance decay behavior of an undoped, MOVPE-grown GaN film observed at various waiting times  $t$  after switching off illumination was measured. The steady-state value of the capacitance decays logarithmically with the waiting time  $t$ . We argue that this phenomenon is closely related to the electron capture process at the dislocation traps, which can be

explained satisfactorily with the barrier-limited recombination model. The characteristic time constant  $t_0$  and the capture cross section  $\sigma_T$  of the electron filling process were experimentally determined for the first time to be  $\sim 34.5$  s and  $< 2.89 \times 10^{-27}$  cm<sup>2</sup>, respectively.



## CHAPTER 8

# ISOELECTRONIC IN-DOPING EFFECTS ON THE LONG-TERM PHOTOCAPACITANCE DECAY BEHAVIOR IN GAN

### 8.1 Introduction

We have already previously discovered that isoelectronic In-doping can effectively suppress the formation of point defects such as E1 and E2 in the DLTS measurements [75], and we also found out the new phenomenon that there is a long-term phot capacitance behavior in undoped GaN [80]. We then were curious about the isoelectronic In isodoping effects on the new phenomenon. In order to understand whether or not the phenomenon still exists after the isoelectronic In-doping, and its influences on the logarithmic time constants, the capture cross sections, the estimated total trap concentrations (in the unit of background concentrations), and above all, the overall crystal quality, we performed the phot capacitance measurements for both the undoped and isoelectronic In-doped GaN films.

## 8.2 Experiments

The undoped and In-doped GaN films were grown on (0001) sapphire substrates at a temperature of 1100°C by a low-pressure horizontal metalorganic vapor phase epitaxy (MOVPE) reactor. For undoped GaN growth, ammonia (NH<sub>3</sub>) and trimethylgallium (TMGa) were used as the N and Ga precursors with flow rates of 3 standard liter per minute and 133 μmol/min, respectively. The growth condition for iso-doped sample was almost the same as undoped one, except that a flow rate of 25.5 μmol/min of TMIIn was introduced into the reactor during the sample preparation. Since the indium atom appears very difficult to enter into the solid at high growth temperatures, the resulted In/Ga ratio in the solid is less than 0.2%, as determined by secondary ion mass spectrometry. Photoluminescence (PL) and Raman measurements further confirm isoelectronic doping properties of our GaN:In film because neither PL emission wavelength shift, nor phonon vibration mode broadening is observed. Hall measurement reveals that the electron carrier concentrations and mobilities are  $4.70 \times 10^{16} \text{ cm}^{-3}$ ,  $77 \text{ cm}^2/\text{V}\cdot\text{s}$  for undoped GaN and  $8.21 \times 10^{16} \text{ cm}^{-3}$  and  $88 \text{ cm}^2/\text{V}\cdot\text{s}$  for doped one. It seems that the Hall properties do not change significantly at this isoelectronic doping level.

Prior to the diode fabrication, the as-grown GaN sample was cleaned in successive rinses of acetone, isopropyl alcohol and D. I. water for 5 min each with ultrasonic agitation and etched by HCl: H<sub>2</sub>O= 1:1 for 10 min. Ni and Al met-



als were then deposited on the front of GaN films to form Schottky and ohmic contacts by electron-gun evaporation through metal masks.

For the measurements of photocapacitance, the Schottky diode was illuminated by a nominal 60 W tungsten lamp for 5 min at zero bias voltage. The sample was then used for the measurement of transient behavior at room temperature using a HP4194 impedance analyzer at different dark waiting times from 5 min to 12 h. For each measurement, a reverse bias of -1 V square voltage with duration of  $\sim 1.5$  s was applied for the purpose of emptying the carrier in the depletion region. Pulses with a test frequency of 10 kHz and 100 meV oscillation level were employed to record the small signal diode capacitance. The trigger duration used was sufficiently long to attain the respective steady state capacitance value,  $C_S(t)$ , so that long-term photocapacitance behavior could be obtained. Attention was paid to ensure that the time interval between the consecutive measurements was at least 4 min. Under these circumstances, any possible intervention between the measurements can be minimized to a negligible extent.

### 8.3 Results and Discussion

Figures 8.1(a) to 8.1(d) shows the transient capacitance of Ni Schottky diodes on both undoped and In-doped GaN epilayers measured at room temperature probed at different time,  $t$ , after the illumination was switched off. For each measurement in Fig. 8.1 when a square triggering voltage is applied, the capaci-

tance signal increases exponentially and saturates to a steady-state value within a duration of  $\sim 0.2$  s. The uprising portion has been attributed primarily to the point defects associated with the deep level of  $\sim 0.6$  eV below the conduction, as previously revealed by deep level transient spectroscopy measurements.[75] This particular trap cannot be due to its fast dynamic response in nature, cannot be considered responsible for the long-term photocapacitance behavior. It is worth noting that the steady-state capacitances  $C_S(t)$  were recorded respectively in 5 min and 1 h units and also plotted in shifted ordinates for both undoped and In-doped GaN Schottky diodes. The heights of  $C_S(t)$  on both sides of the figures are virtually the same for all different time scales used.

Figure 8.2 shows the plot of the time dependence of the steady-state values of the photocapacitance,  $C_S(t)$ , of Ni Schottky diodes on both undoped and In-doped GaN epilayers. We observed that  $C_S(t)$  decreases logarithmically as a function of  $t$  with its value dropping from 116 pF at  $t = 1$  min to 106 pF at  $t = 36$  h for undoped GaN, and from 200 pF at  $t = 1$  min to 188 pF at  $t = 66$  h for In-doped GaN. The vertical offset in between was due to the slight difference of concentrations of net ionized impurity in the space charge region. As can be seen in Fig. 8.2,  $C_S(t)$  is found to maintain its logarithmic decay behavior as a function of  $t$  when small quantities of In are doped into the epilayer.

From eq. (7.10) and the  $C_S(t)$  versus  $t$  curve in Fig. 8.2, we then obtained  $n_T(t)$  of each  $t$  and plotted in Fig. 8.3 and Fig. 8.4. Figure 8.3 shows the ratio

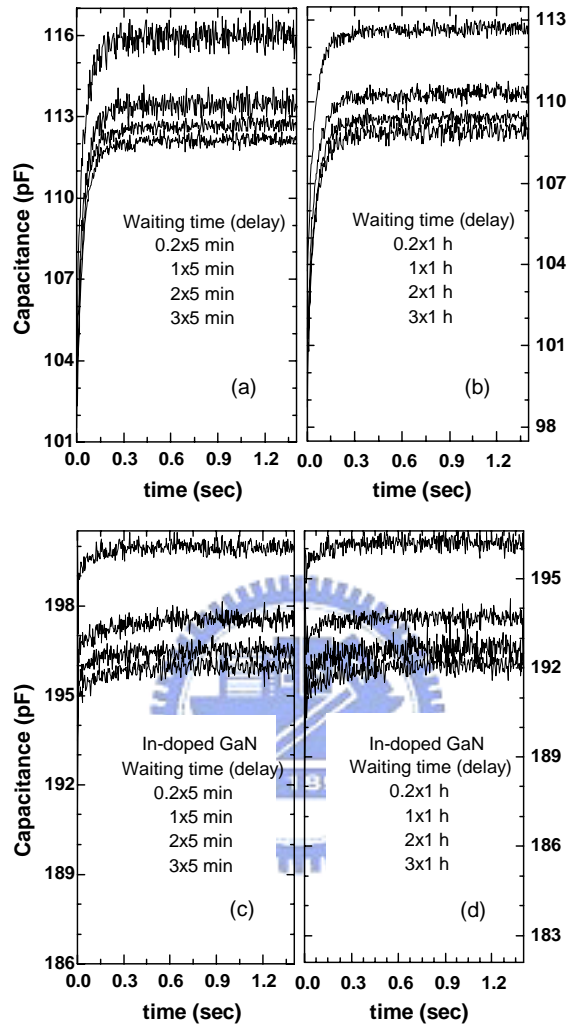


Figure 8.1: The transient capacitance response of the undoped and In-doped GaN during the applications of square voltage recorded at different waiting time,  $t$ , at room temperature.

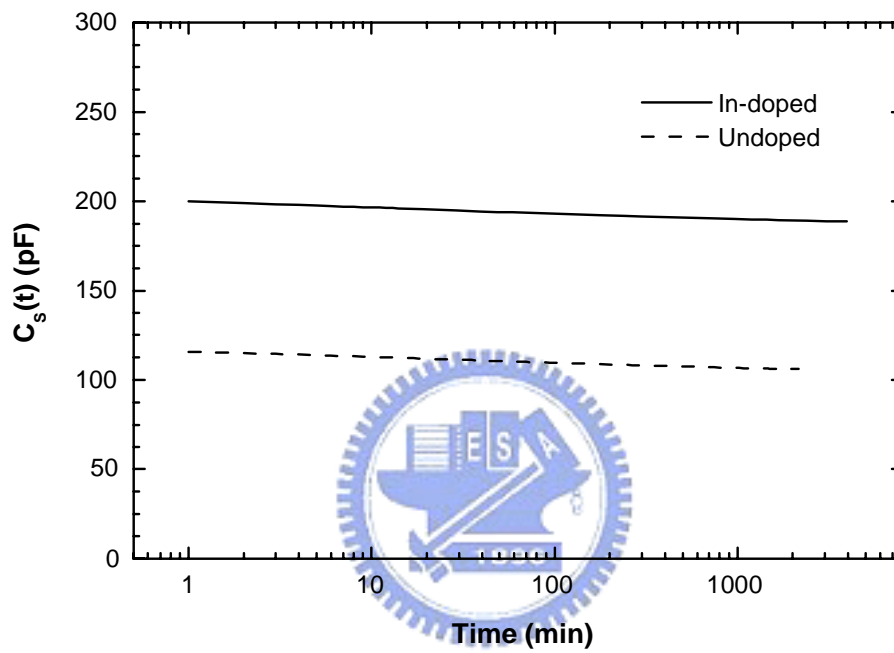


Figure 8.2: The steady state value of transient capacitance,  $C_S(t)$  versus waiting time  $t$  at room temperature for undoped and In-doped GaN.

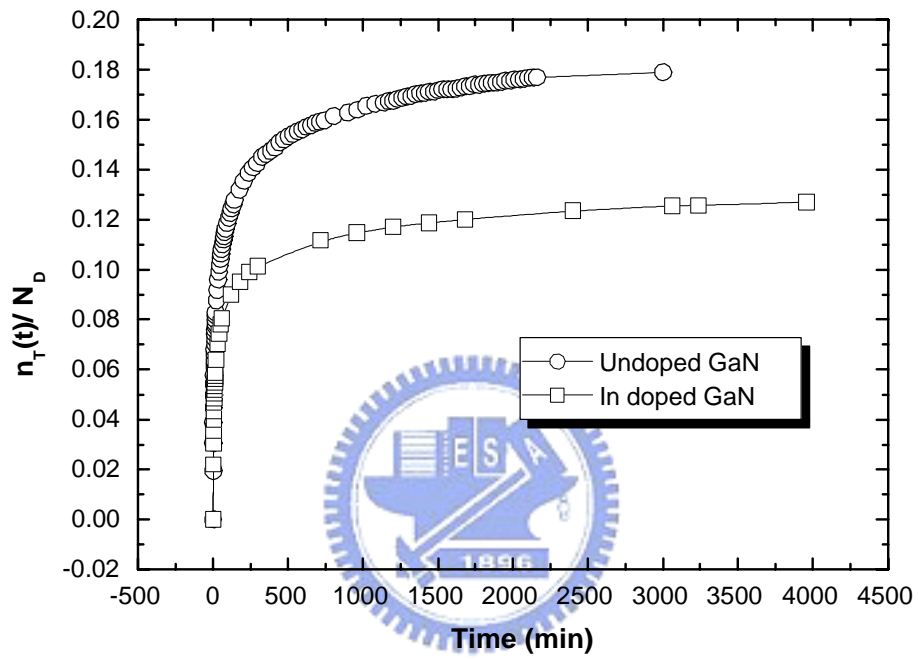


Figure 8.3: The ratio of  $n_T(t)$  and  $N_D$  versus waiting time  $t$  at room temperature for undoped and In-doped GaN films in linear scale.

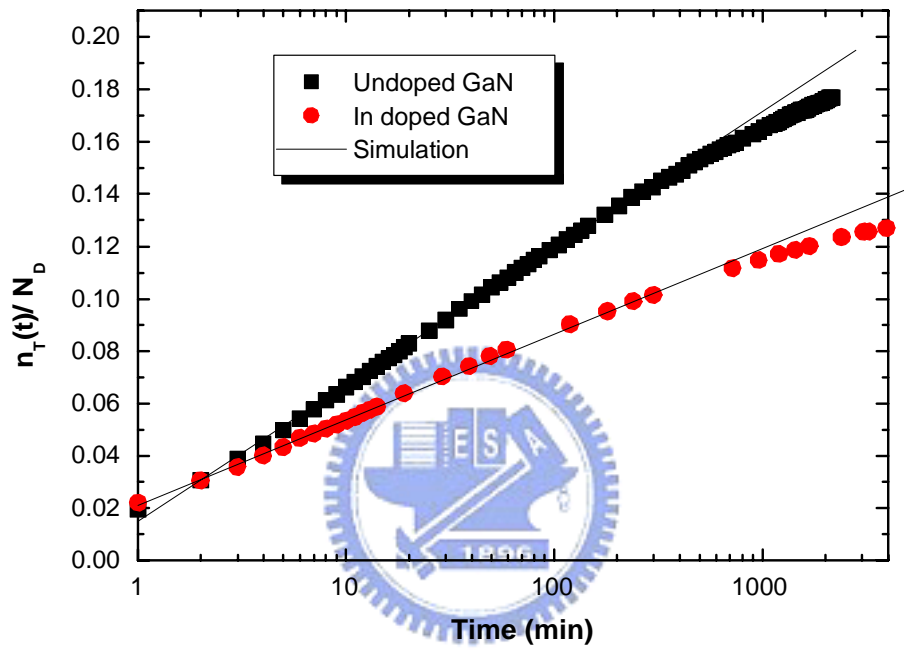


Figure 8.4: The ratio of  $n_T(t)$  and  $N_D$  versus waiting time  $t$  at room temperature for undoped and In-doped GaN films in log scale.

of  $n_T(t)$  and  $N_D$  versus waiting time  $t$  at room temperature for undoped and In-doped GaN films in linear scale. As can be seen in the figure, the  $N_T/N_D$  (obtained by the maximum value of  $n_T/N_D$  as  $t$  goes to the infinity, that is, the time larger than 2500 min) were improved from 18% to 13%. The isoelectronic In doping indeed improved the crystal quality through the suppression on the formation of dislocation-related trap.

Figure 8.4 shows the ratio of  $n_T(t)$  and  $N_D$  versus waiting time  $t$  at room temperature for undoped and In-doped GaN films in log scale. According to the simulation method we previously revealed,[80] from ratio of the retrieved slope and intercept of  $n_T(t) = a + b \ln t$ , using eq. (7.8) and eq. (7.9), we obtained that the time constants and electron capture cross sections are 34.5 s and  $2.89 \times 10^{-27}$  cm<sup>2</sup> for undoped GaN and 13.7 s and  $3.92 \times 10^{-27}$  cm<sup>2</sup> for In-doped ones.

The enlarged electron capture cross section and the shortened logarithmic time constant after the incorporation of In atoms are consistent with the reduction of the concentration of dislocation-related traps, since the suppression of dislocation-related traps would introduce a smaller repulsive Coulomb potential, which would make the traps capture the electrons more easily and form the cylindrical potential around the dislocations more easily, and then introduce the larger electron capture cross section and smaller logarithmic time constant after the isoelectronic In doping.

## 8.4 Summary

In summary, we have measured the dynamic response of photocapacitance of Schottky diodes made of both undoped and isoelectronically In-doped GaN samples at various waiting time  $t$  after illumination was switched off. Experimental results reveal that when small quantities of In atoms are added into the epilayer, the logarithmic time constant was improved from 34.5 to 13.7 s, and the formation of the concentration of the affiliated dislocation traps can be effectively suppressed. This study confirms that isoelectronic doping technique is a simple, yet useful method in reducing the concentration of electron-hole recombination centers at dislocations. Application of this technique may bring an improvement in GaN device performance, particularly for those films grown with large defect concentration.





## CHAPTER 9

# SURFACE TREATMENT EFFECTS ON *P*-GAN SCHOTTKY DIODES

### 9.1 Introduction

The wide-bandgap gallium nitride is a promising material for high-temperature, high-power GaN-based field-effect devices owing to its peculiar properties, such as high electron velocity, good thermal conductivity, high breakdown field, high sheet charge density, large conduction band discontinuity and piezoelectric effect.[81, 82] Because of the use of field effect nature in these devices, the Schottky performance is without question one of the most important issues in implementation of these devices. Up to date, most of relevant works reported has focused on the Schottky properties of *n*-type GaN film, very few literatures have been addressed on that of *p*-type GaN film. For the case of *p*-GaN Schottky diode, T. Mori *et al.* have carried out the study as early as 1996 and reported a barrier height of  $\sim 0.65$  eV.[83] This result is considered to be much lower than the expected value calculated from Schottky approximation, indicating that non-ideal current mechanisms are predominant in device carrier transport. Since the rectifying characteristics rely greatly on the surface properties of the semiconductor, several surface pretreat-

ment methods including the use of HF, HCl solvents, or complex combination of HCl, HF and  $(\text{NH}_4)_2\text{S}$  chemical cleaning steps, have been employed to remove the native oxide and modify the surface electrical properties.[83, 84, 85] Nevertheless, only limited successes have been achieved. Most of  $p$ -GaN Schottky diodes still exhibits very leaky characteristics unless it is made on a low Mg-doped GaN epilayer, which is in turn taken at the expense of high device series resistance and low operation current. In this study, we have made  $p$ -type Schottky diodes on GaN film using different surface cleaning process. Our experiment shows that when the substrate is subjected to ammonia sulfide surface pretreatment process good  $p$ -GaN Schottky contacts can be obtained on a nominal  $p$ -GaN epitaxial layer having a hole concentration of  $2.5 \times 10^{17} \text{ cm}^{-3}$ . Calculation also indicates that the sulfide-treated  $p$ -GaN sample is nearly free from any surface contaminations. The resulted surface state density is as low as  $2.004 \times 10^{12} \text{ cm}^{-2} \text{ eV}^{-1}$ .

## 9.2 Experiments

The epitaxial Mg-doped GaN film used in this experiment was  $1\text{-}\mu\text{m}$  thick, grown by low-pressure horizontal metalorganic vapor phase epitaxy (MOVPE). The corresponding Hall concentration and mobility were measured to be  $2.5 \times 10^{17} \text{ cm}^{-3}$  and  $8 \text{ cm}^2/\text{V}\cdot\text{s}$ , respectively, after the thermal annealing at  $750 \text{ }^\circ\text{C}$  for 40 min. Mirror-like surface morphology is observed for this film and the associated root-mean-square roughness is about  $8 \text{ \AA}$  as revealed by atomic force microscopy

measurement. Prior to the diode fabrication, the wafer was cut into several pieces of samples of approximate area of  $1 \text{ cm}^2$ . All of the samples were degreased in successive rinses of acetone, isopropyl alcohol and de-ionized water for 5 min each with ultrasonic agitation, and dried with nitrogen gas. Several different surface treatments were then employed for these samples. They were immersed either in an HCl solution at room temperature for 4 min or in a boiled  $(\text{NH}_4)_2\text{S}$  solution for 10 min. These samples were subsequently rinsed in de-ionized water, blown dry by nitrogen gas again, and quickly loaded into an electron beam evaporator. Ni metal was then evaporated onto the sample surface through the metal mask to form the Schottky contacts with a diameter of  $\sim 100 \mu\text{m}$ , and to form the stripe ohmic contacts at the same time due to the use of large surface area in this study. To verify the surface treatment effects, we also made Schottky diodes from an Mg-doped GaN film without any inorganic surface cleaning process here for comparison.

### 9.3 Results and Discussion

The  $I$ - $V$  characteristics of these samples were measured with a HP4145B semiconductor analyzer and the  $C$ - $V$  profiles were measured by a HP4194A impedance analyzer at a frequency of 300Hz. The effective barrier height  $\phi_B$  and ideality factor  $n$  of the Schottky diode can be obtained from the  $I$ - $V$  characteristics, assuming carrier transport is dominated by thermionic emission. The  $I$ - $V$  characteristics in

the forward bias is given by[86]

$$J = J_s \exp\left(\frac{q(V - IR_s)}{nkT} - 1\right), \quad (9.1)$$

and

$$J_s = A^{**}T^2 \exp\left(-\frac{q\phi_B}{kT}\right) \quad (9.2)$$

where  $J$  is the current density,  $J_s$  the saturation current density, the Richardson constant ( $96 \text{ Acm}^{-2}\text{K}^{-2}$  for  $p$ -GaN),[85]  $T$  the diode temperature,  $R_s$  series resistance,  $q$  the electron charge,  $n$  ideality factor and  $k$  the Boltzmann's constant.

In Figs. 9.1(a) and 9.1(b), we show the typical room-temperature current density-voltage characteristics of the above Ni Schottky diodes in both linear and log scales. As can be seen in Fig. 9.1(a), almost no rectifying  $I$ - $V$  characteristics can be observed for the untreated  $p$ -GaN Schottky diode. Although HCl surface treatment gives better results in Schottky properties, considerably high leakage current is still observed at reverse bias, very similar to case of the  $p$ -GaN Schottky study reported by K. N. Lee *et al.*[87] For these two samples, the slopes of reverse leakage current vs. bias voltage in log-scale are found to equal approximately 2, showing that the leakage currents are proportional to the device surface area. Such a fact implies that the reverse carrier transport in these two types of samples is influenced significantly by the surface states[86] between the metal and semiconductor interface, which conceivably is one of the major causes responsible for the degradation of such types of  $p$ -GaN Schottky diodes.

On the other hand, well-behaved rectifying characteristics were obtained in

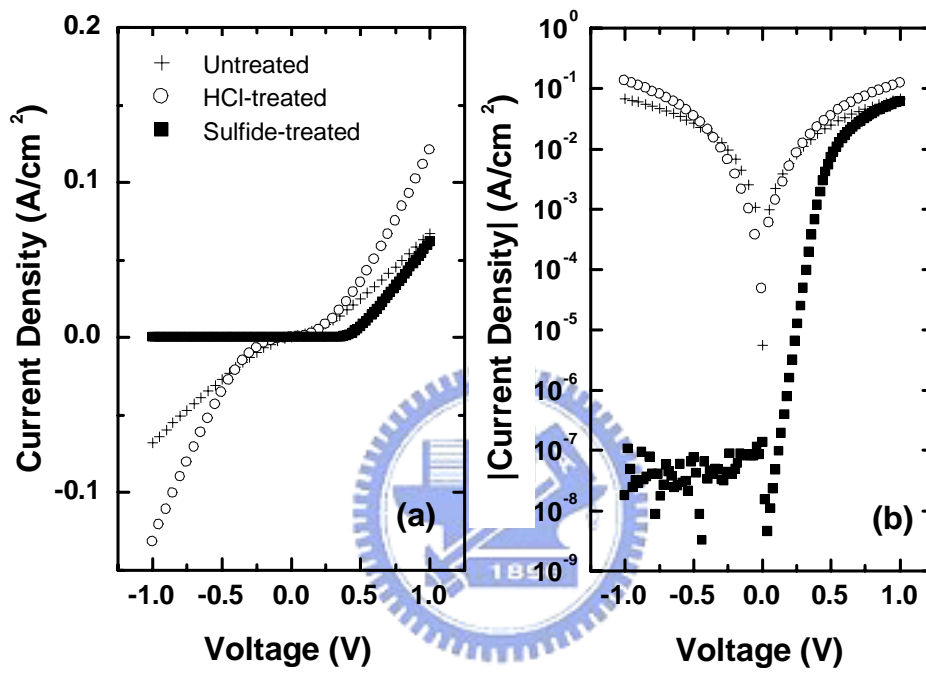


Figure 9.1: Room temperature current density-voltage characteristics of Ni-GaN Schottky diodes with various surface treatments in both linear and log scales.

(NH<sub>4</sub>)<sub>2</sub>S-treated *p*-GaN Schottky diode. As compared to the previous diodes, we can find there are dramatic effects on the diode properties as sulfide treatment is used in preparing *p*-GaN Schottky diode. The calculated ideality factor  $n$ , saturation current  $J_S$  and barrier height  $\phi_b$  are 1.14,  $1.53 \times 10^{-9}$  A/cm<sup>2</sup> and 0.94 eV, respectively, much better than those prepared by the previous methods. Moreover, the resulted reverse leakage current is rather low, down to a value of  $\sim 5 \times 10^{-8}$  A/cm<sup>2</sup>, which represents one of the best values ever reported for *p*-type GaN Schottky diode. Different from the results by X. A. Cao *et al.*[85], our experiment demonstrates that the sulfide surface cleaning process is a viable method for preparing good quality *p*-type Schottky diode.

From the above discussions, particularly the facts of proportionality between the leakage current and diode surface area, together with very leaky current behavior in untreated and HCl-treated diodes, we can infer that the surface of *p*-GaN semiconductor is by nature unstable itself. That is without proper surface treatment, the interface of metal-semiconductor could usually be covered by a large concentration of surface defects due to the dangling bonds on the *p*-GaN surface. In order to investigate the surface states more qualitatively, we thus conducted a *C-V* measurement for these samples. Figure 9.2 shows the *C-V* characteristics of Ni Schottky diodes with different surface treatments measured at room temperature. As can be seen in the figure, the linearity of  $1/C^2$  as a function of reverse bias voltage is held for the sulfide-treated and the HCl-treated samples

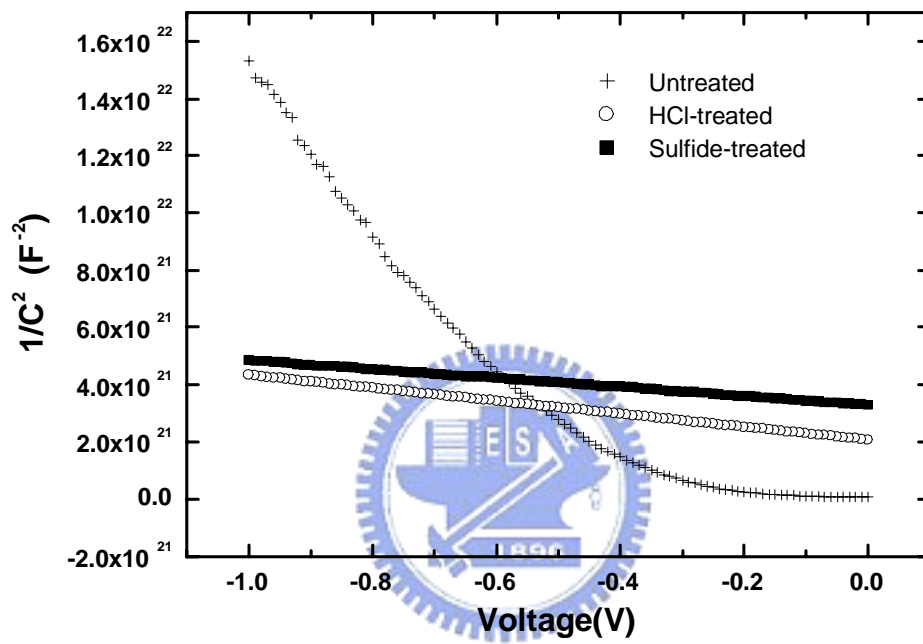


Figure 9.2: Room temperature capacitance-voltage characteristics of Ni-GaN Schottky diodes with various surface treatments.

only, but is invalid for untreated one. The capacitance against applied voltage for the Schottky diode can be expressed as

$$\frac{1}{C^2} = \frac{2(V_{bi} + V_R - kT/q)}{\epsilon_s q N_a A^2}, \quad (9.3)$$

where  $V_{bi}$  is the built-in potential,  $V_R$  the reverse bias voltage,  $\epsilon_s = 9.5 \epsilon_0$  for GaN,  $N_a$  the acceptor concentration,  $A$  is the area of Schottky diode. From the intercept on the voltage axis, the barrier heights can be also determined:

$$\phi_{Bp} = V_{bi} + (E_f - E_v)/q - \Delta\phi_m = \chi + E_g/q - \phi_m - \Delta\phi_{Bp} \quad (9.4)$$

Here  $E_f$  and  $E_v$  are the Fermi level and valence band, and are the electron affinity (4.1 eV) and bandgap (3.4 eV) for GaN,  $\phi_m$  is the Ni metal work function (5.2 eV) and  $\Delta\phi_{Bp}$  represents the barrier lowering due to the image force, which is given by

$$\Delta\phi_{Bp} = \left[ \frac{q^3 N_a}{8\pi^2 \epsilon_s^3} (V_{bi} + V_R) \right]^{1/4}. \quad (9.5)$$

Using these equations, we can have the acceptor concentrations and barrier heights of  $1.08 \times 10^{18}$ ,  $1.56 \times 10^{18} \text{ cm}^{-3}$  and 0.970, 2.190 eV for HCl-treated and  $(\text{NH}_4)_2\text{S}$ -treated samples, respectively. One can note that as the  $C$ - $V$  barrier height of sulfide-treated sample is twice the value of that of HCl-treated one, confirming the significance of sulfide treatment in preparing  $p$ -GaN Schottky diode. After adding up the measured Schottky barrier height  $\phi_{Bp}$  with  $\Delta\phi_{Bp}$  (0.093 eV at reverse bias of one volt), we have a value of 2.283 eV, very close to that of ideal barrier height 2.3 eV derived from Schottky approximation.



The highly coincidence between the experimental and theoretical values strongly suggests that the surface of sulfide treated *p*-GaN is nearly free from any contaminations. Indeed, we have found the density of surface states is approximately of  $2.004 \times 10^{12} \text{ cm}^{-2} \cdot \text{eV}^{-1}$  in accord with the following formula we developed following the model by Cowley and Sze[86]

$$\phi_{Bp} + \Delta\phi_{Bp} = b_2 [E_g/q - (\phi_m - \chi)] + (1 - b_2)(E_g/q - \phi_0), \quad (9.6)$$

and

$$D_s = \frac{(b_2 - 1)\epsilon_i}{b_2\delta q^2}, \quad (9.7)$$

, by assuming that the sulfide cleaned *p*-GaN surface has a thin interfacial layer with  $\delta = 5 \text{ \AA}$ ,  $\epsilon_i = 3.8 \epsilon_0$ , and  $\phi_0 = 2.334 \text{ eV}$ . [86, 88, 89, 90] Here,  $\delta$  is the thickness of the interfacial layer and  $\epsilon_i$  is its permittivity, and  $\phi_0$  represents the neutral energy level for the surface states. Such a value is considerably lower than those of most III-V semiconductor compounds, such as Si, GaP and GaAs, which lying in the range from  $2.7 \times 10^{13}$  to  $12.5 \times 10^{13} \text{ cm}^{-2} \cdot \text{eV}^{-1}$ . On the contrary, the resulted surface state density for HCl-treated sample is quite large. The corresponding value is as high as  $1.020 \times 10^{15} \text{ cm}^{-2} \cdot \text{eV}^{-1}$  ( $\delta = 10 \text{ \AA}$  and  $\epsilon_i = 10.2 \epsilon_0$ , and  $\phi_0 = 2.334 \text{ eV}$ ), [85, 86, 91] comparable to the maximum dangling bond density  $3.404 \times 10^{15} \text{ cm}^{-2} \text{ eV}^{-1}$  that can be allowed for GaN surface.

We believe such a distinct surface density reduction in sulfide-treated *p*-GaN diode is contributed primarily to the surface passivation effects imposed by sulfur atoms. It has been reported that when the  $(\text{NH}_4)_2\text{S}$  solution is introduced during

the cleaning process for GaN, it will not only produce a low coverage of oxygen on the surface, but the sulfur atoms can also fill in the nitrogen vacancies and react with the gallium atoms to form stable Ga-S bonds to prevent from further oxidation in the air.[89] Consequently, a virtually contamination-free surface can be obtained for the *p*-type GaN film after the sulfide pretreatment surface process. Although, the HCl process can also effectively remove the native oxide, it seems not necessary to warrant a low concentration of surface defects on *p*-type GaN sample. S. W. King *et al.*[92] have pointed out that the exposure of GaN surface to HCl solution could inevitably leave significant amounts of residual Cl contaminants and C-H bonded carbons on the surface. That may explain partially for the extraordinary high density of surface states observed in our HCl-treated *p*-GaN Schottky diode.



#### 9.4 Summary

In summary, we have investigated the surface treatment effects on the *I-V* and *C-V* characteristics of *p*-GaN Schottky diodes using different cleaning steps. Poor rectifying characteristics were observed on both untreated and HCl-treated samples. When the sample was undergone  $(\text{NH}_4)_2\text{S}$  treatment process, significantly improved Schottky behaviors could be obtained. The resulted ideality factor, reverse leakage current, *I-V* barrier height and *C-V* barrier height are 1.14,  $1.53 \times 10^{-9} \text{A/cm}^2$ , 0.94 eV and 2.19 eV, respectively, indicating the good quality of

our *p*-type GaN Schottky contact. Furthermore, we have also found that  $(\text{NH}_4)_2\text{S}$  surface pretreatment has a profound effect in the reduction of surface state density for GaN. The corresponding surface state density can be reduced to a value as low as  $2.004 \times 10^{12} \text{ cm}^{-2} \text{ eV}^{-1}$ , which is about a three-order of magnitude improved than that of contact deposited on HCl-treated *p*-GaN surface.



## CHAPTER 10

### CONCLUSION

#### 10.1 On the Isoelectronic In-doping Effects in GaN

Indium isoelectronic doping was found to have profound effects on electrical properties of GaN films grown by metalorganic chemical vapor deposition. When a small amount of In atoms was introduced into the epilayer, the ideality factor of n-GaN Schottky diode was improved from 1.20 to 1.06, and its calculated saturation current could be reduced by two order of magnitude as compared to that of undoped sample. Moreover, it is interesting to note that In isodoping can effectively suppress the formation of deep levels at 0.149 and 0.601 eV below the conduction band, with the 0.149 eV trap concentration even reduced to an undetected level. Our result indicates that the isoelectronic In doping technique is viable way to improve the GaN film quality.

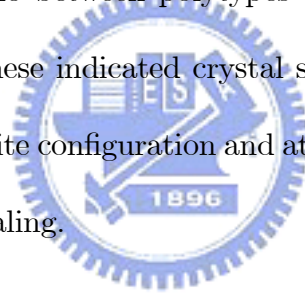
#### 10.2 On the Isoelectronic As-implanted Effects in GaN

Hall, current-voltage and deep level transient spectroscopy measurements were used to characterize the electric properties of *n*-type GaN films implanted with As atoms. After 800°C thermal annealing for 60 min, one additional deep level

located at  $E_C - 0.766$  eV was found in the films. We presume this induced trap is arsenic-related point defect, most likely antisite in nature.

### 10.3 On the Microstructural Study of Thermal Annealing Effects on Mg doped GaN Films

Ga *K*-edge *x*-ray absorption measurements were employed to investigate thermal annealing effects on Mg-doped GaN films. The effects are anisotropic with respect to the crystal axes and have the greatest crystal microstructural change along the perpendicular of the epilayer surface. The effects also involved shifting of the structural mixing ratio between polytypes and increasing of Debye temperature of the films. All these indicated crystal structure relaxation towards a more stable hexagonal wurtzite configuration and atomic rearrangement to a more orderly condition after annealing.



### 10.4 On the Long-Term Photocapacitance Decay Behavior in Undoped GaN Films

We have measured the dynamic response of the photocapacitance of a Schottky diode made of an undoped GaN epilayer grown by metalorganic vapor phase epitaxy. The measurements were performed after the suspension of a white light for a specified “waiting” time,  $t$ . The results indicate that the capacitance exhibits a logarithmic function of  $t$  from which a time constant of approximately 34.5 s and

a cross-sectional area of less than  $2.89 \times 10^{-27} \text{ cm}^2$  were retrieved. These are interpreted as the characteristic time and the cross-sectional area of electron capture by the traps associated with dislocations formed in the epilayer, respectively.

## 10.5 On the Isoelectronic In-doping Effects on the Long-Term Photocapacitance Decay Behavior in GaN

Indium isoelectronic doping was found to have profound effects on the dynamic response of the photocapacitance of Schottky diodes made of GaN epilayers grown by metalorganic vapor phase epitaxy. When a small amount of In atoms was introduced into the epilayer, the steady state value of photocapacitance retains its logarithmic decay behavior, and the logarithmic time constant was improved from 34.5 to 13.7 s. Moreover, it is interesting to note that In isodoping can slightly enlarge the electron capture cross section and effectively suppress the formation of the concentration of the affiliated dislocation traps. Our results indicate that In-doping technique is a viable way to improve the GaN film quality.

## 10.6 On the Surface Treatment Effects on GaN Schottky Diodes

The current-voltage ( $I$ - $V$ ) and capacitance-voltage ( $C$ - $V$ ) measurements were employed to characterize the electrical properties and surface state density for Ni/ $p$ -GaN Schottky diodes prepared by different surface cleaning methods. Experimental results indicate that the associated Schottky behaviors were very sen-

sitive to the surface treatment process prior to the metal deposition. Rather poor rectifying characteristics were resulted for both untreated and HCl-treated samples. However, we do observe a well-behaved Schottky profiles for  $p$ -GaN Schottky diode surface-treated by  $(\text{NH}_4)_2\text{S}$  solution. The corresponding ideality factor, saturation current density,  $I$ - $V$  barrier height and  $C$ - $V$  barrier height are 1.14,  $1.53 \times 10^{-9}$  A/cm<sup>2</sup>, 0.94 eV and 2.19 eV, respectively, suggesting the good quality of our Schottky diode. More interestingly, theoretical calculation also indicates that the surface state density for  $(\text{NH}_4)_2\text{S}$ -treated  $p$ -type GaN film is quite low, down to a value of  $\sim 2 \times 10^{12}$  cm<sup>-2</sup>eV<sup>-1</sup>, which is comparatively lower than that obtained by using HCl-cleaning method.



## BIBLIOGRAPHY

- [1] J. Stöhr, *NEXAFS spectroscopy* (Springer, Berlin, 1992).
- [2] M. Katsikin, E. C. Paloura, T. D. Moustakas, *J. Appl. Phys.* **83**, 1437 (1998).
- [3] K. Lawniczak-Jablonska, T. Suski, Z. Liliental-Weber, E. M. Gullikson, J. H. Underwood, R. C. C. Perera, and T. J. Drummond, *Appl. Phys. Lett.* **70**, 2711 (1997).
- [4] Kronig, R. del. Z., *Phys.* **70**, 317 (1931).
- [5] Kronig, R. del. Z. *Phys.* **75**, 468 (1932); *ibid.*, **76**, 468 (1975).
- [6] F. W. Lytle, D. E. Sayers, and E. B. Moore, *Appl. Phys. Lett.*, **24**, 45 (1974).
- [7] F. W. Lytle, D. E. Sayers, and E. B. Moore. *Phys. Rev. B* **11**, 4825 (1975); **11**, 4836 (1975).
- [8] P. M. Eisenberger and B. M. Kincaid, *Chem. Phys. Lett.* **36**, 134 (1975).
- [9] B. M. Kincaid, Ph.d. Thesis, Stanford University, 1975.
- [10] B. M. Kincaid, P. Eisenberger, *Phys. Rev. Lett.* **34**, 1361 (1975).



- [11] B. M. Kincaid, P. Eisenberger, K. O. Hodgson, S. Doniach, Proc. Natl. Acad. Sci. U. S. A. **72**, 2340 (1975).
- [12] Boon K. Teo, *EXAFS: Basic Principles and Data Analysis*, Springer-Verlag (1986).
- [13] J. Bardeen, Phys. Rev. **71**, 717 (1947).
- [14] R. H. Kingstom, *Semiconductor Surface Physics* (University of Pennsylvania Press, Philadelphia, 1957).
- [15] R. J. Archer and M. M. Atalla, Am. Acad. Sci. N. Y. **101**, 697 (1963).
- [16] H. K. Henisch, *Rectifying Semiconductor Contacts* (Oxford University Press, New York, 1957), Chap. VII.
- [17] C. A. Mead and W. G. Spitzer, Phys. Rev. **134**, A713 (1964).
- [18] C. R. Crowell, S. M. Sze, and W. G. Spitzer, Appl. Phys. Lett. **4**, 91 (1964).
- [19] A. M. Cowley and S. M. Sze, J. Appl. Phys. **36**, 3212 (1965).
- [20] S. M. Sze, C. R. Crowell, and D. Kahng, J. Appl. Phys. **35**, 2534 (1964).
- [21] S. Yoshida, J. Suzuki, J. Appl. Phys. **84**, 2940 (1998).
- [22] S. Nakamura, M. Senoh, S-I Nagahama, T. Matsushita, K. Kiyoku, Y. Sugimoto, T. Kozaki, H. Umemoto, M. Sano, and T. Mukai, Jpn. J. Appl. Phys., Part 2 **38**, L1966 (1999).
- [23] S. Binari, H. B. Dietrich, W. Kruppa, G. Kelner, N. S. Saks, A. Edwards,

J. M. Redwing, A. E. Wickenden, and D. D. Koleske, in Proceedings of the Second International Conference on Nitride Semiconductors ICNS'97, Tokushima, Japan, 1997, Japan Society of Applied Physics, p. 476.

[24] D. G. Thomas, J. J. Hopfield, and C. J. Frosch, Phys. Rev. Lett. **15**, 857 (1965).

[25] P. K. Bhattacharya, S. Dhar, P. Berger, and f. Y. Juang, Appl. Phys. Lett. **49**, 470 (1986)

[26] S. M. Sze, *Physics of Semiconductor Devices*, (Wiley Eastern Limited, New Delhi, India, 1969).

[27] P. Hacke, A. Maekawa, N. Koide, K. Hiramatsu, Jpn. J. Appl. Phys. **31**, 6443 (1994).

[28] P. Hacke, T. Detchprohm, K. Hiramatsu, and N. Sawaki, J. Appl. Phys. **76**, 304 (1994).

[29] W. Gotz, N. M. Johnson, H. Amano, and I. Akasaki, Appl. Phys. Lett. **65**, 463 (1994).

[30] Z.-Q. Fang, J. W. Hemsley, and D. C. Look, Appl. Phys. Lett. **72**, 448 (1998).

[31] W. I. Lee, T. C. Huang, J. D. Guo, and M. S. N. M. Johnson, H. Amano, and I. Akasaki, Appl. Phys. Lett. **65**, 463 (1994).

[32] C. D. Wang, L. S. Yu, S. S. Lau, and E. T. Yu, Appl. Phys. Lett. **72**, 1211 (1998).

[33] D. Hasse, M. Schmid, W. Kumer, A. Domen, V. Harle, F. Scholz, M. Burkard, and H. Schweizer, Appl. Phys. Lett. **69**, 2525 (1996).

- [34] D. W. Jenkins and J. D. Dow, Phys. Rev. B **39**, 3317 (1989).
- [35] C. K. Shu, J. Ou, H. C. Lin, W. K. Chen, and M. C. Lee, Appl. Phys. Lett. **73**, 641 (1998).
- [36] D. I. Barrett, S. McGuigan, H. M. Hobgood, G. W. Eldridge and R. N. Thomas, J. Cryst. Growth, **70**, 179 (1984).
- [37] S. Yoshida, J. Suzuki, J. Appl Phys. **84**, 2940 (1998).
- [38] S. Nakamura, M. Senoh, S-I Nagahama, T. Matsushita, K. Kiyoku, Y. Sugimoto, T. Kozaki, H. Umemoto, M. Sano, and T. Mukai, Jpn J. Appl. Phys., Part 2 **38**, L1966 (1999).
- [39] Y. Kuga, T. Shirai, M. Haruyama, H. Kawanishi, and Y. Suematsu, Jpn J. Appl. Phys. **34**, 4085 (1995).
- [40] H. M. Chung, W. C. Chung, Y. C. Pan, C. C. Tsai, M. C. Lee, W. H. Chen, W. K. Chen, C. I. Chiang, C. H. Lin, and H. Chang, Appl. Phys. Lett. **76**, 897 (2000).
- [41] T. Mattila, and A. Zunger, Phys. Rev. B **58**, 1367 (1998).
- [42] C. G. Van de Waale, and J. Neugebauer, Appl. Phys. Lett. **76**, 1009 (2000).
- [43] W. M. Jadwisieniczak and H. J. Lozykowski, MRS Proc. **482**, 1033 (1998).
- [44] L. J. Guido, P. Mitev, M. Gherasimova, and B. Gaffey, Appl. Phys. Lett. **72**, 2005 (1998).
- [45] X. Li, S. Kim, E. E. Reuter, S. G. Bishop, and J. J. Coleman, Appl. Phys. Lett. **72**, 1990 (1998).

- [46] B. Gil, A. Morel, T. Taliercio, P. Iefebvre, C. T. Foxon, I. Harrison, A. J. Winsor, and S. V. Novikov, *Appl. Phys. Lett.* **79**, 69 (2001).
- [47] S. R. Jin, M. Ramsteiner, H. T. Grahn, K. H. Ploog, Z. Q. Zhu, D. X. Shen, A. Z. Li, P. Metev, and L. J. Guido, *J. Cryst. Growth* **212**, 56 (2000).
- [48] Our unpublished data.
- [49] F. D. Auret, S. A. Goodman, F. K. Koschnick, J-M. Spaeth, B. Beaumont, P. Gibart, *Appl. Phys. Lett.* **73**, 3745 (1998).
- [50] D. Haase, M. Schmid, W. Kumer, A. Dornen, V. Harle, F. Scholz, M. Butkard, and H. Schweizer, *Appl. Phys. Lett.* **69**, 2525 (1996).
- [51] Z. Q. Fang, D. C. Look, J. Jasinski, M. Benamara, Z. L. Weber, and R. J. Molner, *Appl. Phys. Lett.* **78**, 332 (2001).
- [52] C. D. Wang, L. S. Yu, S. S. Lau, and E. T. Yu, *Appl. Phys. Lett.* **72**, 1211 (1998).
- [53] R. Passler, *J. Appl. Phys.* **90**, 3956 (2001).
- [54] E. Monroy, T. Palacios, O. Hainaut, F. Omnes, F. Calle, and J. F. Hochedez, *Appl. Phys. Lett.* **80**, 3198 (2002).
- [55] D. Ciplis, R. Rimeika, M. S. Shur, S. Rumyantsev, R. Gaska, A. Sereika, J. Yang, and M. A. Khan, *Appl. Phys. Lett.* **80**, 2020 (2002).
- [56] K. Kumakura, T. Makimoto, and N. Kobayashi, *Appl. Phys. Lett.* **80**, 1225 (2002).

- [57] M. G. Cheong, K. S. Kim, C. S. Kim, R. J. Choi, H. S. Yoon, N. W. Namgung, E. K. Suh, and H. J. Lee, *Appl. Phys. Lett.* **80**, 1001 (2002).
- [58] K. T. Tsen, C. Koch, Y. Chen, H. Morkoc, J. Li, J. Y. Lin, and H. X. Jiang, *Appl. Phys. Lett.* **76**, 2889 (2000).
- [59] F. Shahedipour and B. W. Wessels, *Appl. Phys. Lett.* **76**, 3011 (2000).
- [60] S. Nakamura, N. Iwasa, M. Senoh, and T. Mukai, *Jpn. J. Appl. Phys., Part 1*, **31**, 1258 (1992).
- [61] K. Lawniczak-Jablonska, T. Suski, Z. Liliental-Weber, E. M. Gullikson, J. H. Underwood, R. C. C. Perera, and T. J. Drummond, *Appl. Phys. Lett.* **70**, 2711 (1997).
- [62] *X-ray Absorption*, edited by D. C. Koningsberger and R. Prins, (Wiley, New York, 1988).
- [63] Y. C. Pan, S. F. Wang, W. H. Lee, M. C. Lee, W. K. Chen, W. H. Chen, L. Y. Jang, J. F. Lee, C. I. Chiang, H. Chang, K. T. Wu, and D. S. Lin, *Appl. Phys. Lett.* **78**, 31 (2001).
- [64] C. Y. Yeh, Z. W. Lu, S. Froyen, and A. Zunger, *Phys. Rev. B*, **46**, 10087 (1992).
- [65] Our unpublished data.
- [66] E. Sevillano, H. Meuth, and J. J. Rehr, *Phys. Rev. B*, **20**, 4908 (1979).
- [67] S. Yoshida and J. Suzuki, *J. Appl. Phys.* **84**, 2940 (1998).
- [68] S. Nakamura, M. Senoh, S. I. Nagahama, T. Matsushita, K. Kiyoku, Y.

- Sugimoto, T. Kozaki, H. Umemoto, M. Sano and T. Mukai, *Jpn. J. Appl. Phys.* **38**, L1966 (1999).
- [69] F. A. Ponce, D. Cherns, W. T. Young and J. W. Steeds, *Appl. Phys. Lett.* **69**, 770 (1996).
- [70] S. J. Rosner, E. C. Carr, M. J. Ludowise, G. Girolami and H. I. Erikson, *Appl. Phys. Lett.* **70**, 420 (1997).
- [71] P. J. Hansen, Y. E. Strausser, A. N. Erickson, E. J. Tarsa, P. Kozodoy, E. G. Brazel, J. P. Ibbetson, U. Mishra, V. Narayanamurti, S. P. DenBaars and J. S. Speck, *Appl. Phys. Lett.* **72**, 2247 (1998).
- [72] D. C. Look and J. R. Sizelove, *Phys. Rev. Lett.* **82**, 1237 (1999).
- [73] A. F. Wright and U. Grossner, *Appl. Phys. Lett.* **73**, 2751 (1998).
- [74] J. Elsner, R. Jones, M. I. Heggie, P. K. Stich, M. Haugk, Th. Frauenheim, S. Oberg and P. R. Briddon, *Phys. Rev. B* **58**, 12571 (1998).
- [75] H. M. Chung, W. C. Chuang, Y. C. Pan, C. C. Tsai, M. C. Lee, W. H. Chen, W. K. Chen, C. I. Chiang, C. H. Lin and H. Chang, *Appl. Phys. Lett.* **76**, 897 (2000).
- [76] H. Nakata and T. Ninomiya, *J. Phys. Soc. Jpn.* **47**, 1912 (1979).
- [77] Z. Z. Bandic, P. M. Bridger, E. C. Piquette and T. C. McGill, *Appl. Phys. Lett.* **72**, 3166 (1998).
- [78] T. Figielski, *Solid State Electron.* **21**, 1403 (1978).

- [79] D. K. Schroder, *Semiconductor Material and Device characterization* (Wiley, New York, 1998) p. 276.
- [80] H. M. Chung, Y. C. Pan, W. C. Chuang, N. C. Chen, C. C. Tsai, M. C. Lee, W. H. Chen, and W. K. Chen, *Jpn. J. Appl. Phys., Part 1* **40**, 5871 (2001).
- [81] S. Nakamura, M. Senoh, N. Iwasa, and S. Nagahama, *Jpn. J. Appl. Phys., Part 2* **34**, L797 (1995).
- [82] L. Lee, W. C. Lee, H. M. Chung, M. C. Lee, W. H. Chen, W. K. Chen, and H. Y. Lee, *Appl. Phys. Lett.* **81**, 1812 (2002).
- [83] T. Mori, T. Kozawa, T. Ohwaki, Y. Taga, S. Nagai, S. Yamasaki, S. Asami, N. Shibata, and M. Koike, *Appl. Phys. Lett.* **69**, 3537 (1996).
- [84] Z. Z. Bandic, P. M. Bridger, E. C. Piquette, and T. C. McGill, *Appl. Phys. Lett.* **73**, 3726 (1998).
- [85] X. A. Cao, S. J. Pearton, G. Dang, A. P. Zhang, F. Ren, and J. M. Van Hove, *Appl. Phys. Lett.* **75**, 4130 (1999).
- [86] S. M. Sze, *Physics of Semiconductor Devices*, (John Wiley & Sons, New York, USA, 1981).
- [87] K. N. Lee, X. A. Cao, C. R. Abernathy, S. J. Pearton, A. P. Zhang, F. Ren, R. Hickman, and J. M. Van Hove, *Solid-State Electron.* **44**, 1203 (2000).
- [88] R. S. Besser, and C. R. Helms, *J. Appl. Phys.* **65**, 4306 (1989).
- [89] Y. J. Lin, C. D. Tsai, Y. T. Lyu and C. T. Lee, *Appl. Phys. Lett.* **77**, 687 (2000).

- [90] X. Y. Chen, X. Y. Hou, X. A. Cao, X. M. Ding, L. Y. Chen, G. Q. Zhao, and X. Wang, *J. Cryst. Growth* **173**, 51 (1997).
- [91] D. J. Fu, Y. H. Kwon, T. W. Kang, C. J. Park, K. H. Baek, H. Y. Cho, D. H. Shin, C. H. Lee, and K. S. Chung, *Appl. Phys. Lett.* **80**, 446 (2002).
- [92] S. W. King, J. P. Barnak, M. D. Bremser, K. M. Tracy, C. Ronning, R. F. Davis, and R. J. Nemanich, *J. Appl. Phys.* **84**, 5428 (1998).

